DEVELOPMENT OF A HIGH-PRESSURE, GAS-FILLED ION SOURCE FOR A RADIOACTIVE BEAM FACILITY

By

Patrick Andrew Lofy

A DISSERTATION

Submitted to
Michigan State University
in partial fulfillment of the requirements
for the degree of

DOCTOR OF PHILOSOPHY

Department of Chemistry

2003

ABSTRACT

DEVELOPMENT OF A HIGH-PRESSURE, GAS-FILLED ION SOURCE FOR A RADIOACTIVE BEAM FACILITY

By

Patrick Andrew Lofy

The National Superconducting Cyclotron Laboratory (NSCL) produces radioactive nuclear beams (RNBs) by in-flight fragmentation of fast ion beams. This method produces nuclei more exotic (having a more extreme neutron-proton ratio) than methods at other RNB facilities. However, the resulting beams, by comparison, have other characteristics, such as very high velocities, which can be less desirable for certain nuclear science experiments. It was the goal of the research in this work to construct an ion source which would capture the fast exotic beams produced at the NSCL, and re-emit them near thermal velocities for use in precision experiments, thus expanding the capabilities of a fragmentation facility.

We have developed a new high efficiency, high pressure, gas filled ion source for radioactive ions. The source utilizes a high pressure ($\sim$1 bar) helium gas cell which stops fast ($\sim$100 MeV/nucleon) radioactive ions. These exotic nuclei are thermalized in the helium and extracted with a combination of electrodes and gas flow through a nozzle. The ions will then be captured in a radiofrequency quadrupole rod structure in a differentially pumped expansion chamber and then transported downstream for use in precision nuclear science experiments.

Presented in this volume are the preparations, results and interpretation of the stopping and extraction efforts. The features and operation of the major components will be addressed. For radioactive beams spanning a large range of masses (A$\sim$40 to 120), the source has shown the ability to stop (typically) 30-70% of the ions introduced into the gas cell. The combined stopping and extraction efficiency has been shown

to be approximately 0.5%. These results demonstrate that this source will be useful in providing a low-energy, high-quality ion beam to precision experiments for many new nuclides produced in the NSCL Coupled Cyclotron Facility despite their short half-life (down to ∼100 ms) and low production rate (as low as ∼100/s). In addition, this method of stopping fast beams shows promise for use in future radioactive beam facilities such as RIA (the Rare Isotope Accelerator). Finally, future work and planned improvements are presented.

to those who have come before me, who have undergone the fatigue of building the roads and bridges I now traverse

ACKNOWLEDGMENTS

My thanks starts with the organization known as the NSCL, an exceptional lab with a dedicated staff. I firmly believe that I was provided more than the standard graduate education in chemistry. My degree was completed with the contribution of more than 100 employees of the lab, everyone from professors to welders to beam tuners and machinists. The experience of interacting with all these people afforded me an experience like few other students receive.

The faculty of the NSCL is a group to be admired. The contributions of my committee to my education will always be remembered. First the greatest thanks go to my advisor, Professor David J. Morrissey. His value to my education and to the lab have not gone unnoticed. His mantra on dealing with his group "Everyone's different" certainly applied to me, as I sometimes took less-traveled paths in completing my degree. Professor Paul Mantica was my second reader and sometimes second advisor. I thank him for making the phone calls which brought me to MSU and for being the voice 'whispering in the wind' when I needed additional guidance. To Professor Thomas Glasmacher I owe a debt for making me an adjunct member of his group while I was temporarily in need of a project. I recall him often asking (with a mild German accent) "How would they do that in the Army?" which made me feel more important....if even for a moment. Finally, my thanks go to Professor Brad Sherrill, who I can only describe as a man of 'quiet efficiency.' He is the finest example of an intelligent soul who pauses slightly before giving the most thoughtful answers and advice.

The next bunch deserving of my thanks are fellow students and group members. To those students of NSCL Past who made my start at the lab more tolerable: the wise guys (Jac Caggiano, Jon Kruse, Chris Powell, Erik Tryggestad) who continually reminded me that there was life outside the laboratory walls, and to my academic family (brother Don Anthony, step-cousins Joann Prisciandaro and Dan Groh) who

helped me along time after time. Don and Joann, to you I owe more than I can repay. To all of the students of NSCL Present I thank you for your friendship and tolerance, especially Katie Miller, Jennifer Church, Mark Wallace, Michelle Ouellette, Heather Olliver, and James Russell Terry. To the LEBIT group members, who have been instrumental in the continuing success of my project: Professor Georg Bollen, Stefan Schwarz, Ryan Ringle, Peter Schury and Sun Tao. Finally, I give special thanks to my group members Leo Weissman and Debbie Davies. Without their many great efforts, I would still be months away from writing these acknowledgments.

As a last thanks to the lab, I recognize the contributions of the many staff members who ensured that my work succeeded. Specific praise is for the welders, the machinists, the plumbers, the coil-winders, the electricians, the administrators, the cryogenicists, the designers, the cyclotron operators, and the beam tuners who make science at the lab possible. Special recognition goes to Mr. Jack Ottarson in design for withstanding my excessive visits to his office. Although an older and wiser gentlemen, he somehow was empathetic in feeling my pain. I thank him for not having the meter running while I usurped his time.

The last body I wish to thank is in the form of the many influences on the life of Patrick A. Lofy. To the greatest influence in my life, my family, for my fortunate upbringing. My parents, Francis and Dona (with one 'n') have always provided for me. To the church which taught me to respect others and to the Boy Scouts which helped a young boy grow up. To my high school chemistry teacher, Mr. Brian Molle (and his strong family) for the inspiration which sent me down the path of chemistry. To two undergraduate professors who taught me both chemistry and important lessons of life: Corporal Roy Shaver for the guidance and mentoring of a wise old owl and Lieutenant (j.g.) Harold Fenrick for his wit and wisdom and enthusiasm for teaching. Finally, I give thanks to the United States Army for its positive influences on me and to the military men and women who serve and have served to grant me the privileges which I enjoy now.

Contents

List of Figures

IMAGES IN THIS DISSERTATION ARE PRESENTED IN COLOR.

List of Tables

Chapter 1

Introduction

1.1 Motivation for Nuclear Physics Studies

The span of pure research in the field of nuclear science can largely be summarized as the further understanding of our universe in two areas: nuclear structure and (astrophysical) nucleosynthesis. It is our natural curiosity which drives us to comprehend the details of some of the smallest objects as well as the processes which occur in the some of the largest objects in the universe that created these tiny objects billions of years ago. Our learning more about both fields leads to a firmer grasp of both the composition and genesis of our world.

The study of radioactive nuclear species, nuclei not common in our everyday life, provides insight into the constitution of and the processes which make up matter and energy in our universe. Radioactive nuclear beam (RNB) research is the focus of the experimental program at the National Superconducting Cyclotron Laboratory (NSCL). It is the first step in the manipulation of these RNBs, gas stopping, which is the focus of the present work.

1.1.1 Nuclear Structure Motivation

The landscape of nuclear structure is conveniently represented by the chart of nuclides, or Segré chart (Figure 1.1). The horizontal axis is the neutron number, while the vertical axis is the proton number. The dark squares along the central diagonal axis denote the positions of the less than 300 stable nuclei. Moving away from this line of stability, the next set of nuclides (in yellow) are those which have been measured in some form. The remaining nuclei, out to the left (proton drip line) and right (neutron drip line) extremes are yet unknown, but are predicted by various theories to be particle stable; that is, each of the nuclei in the green areas should survive long enough to be studied.

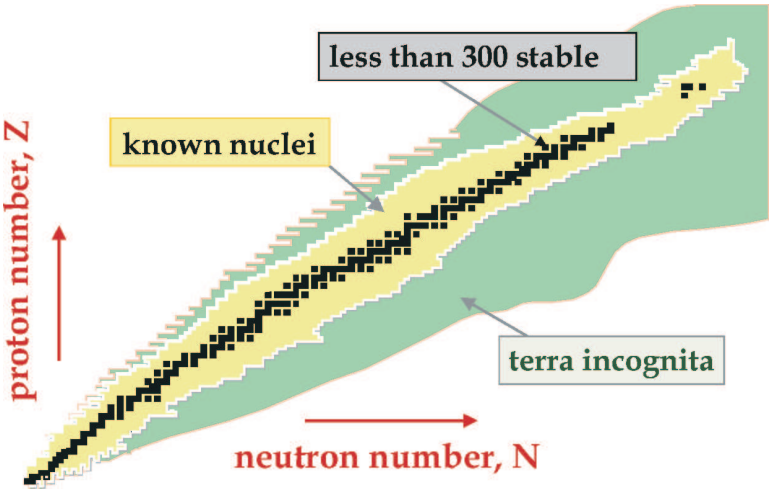

Figure 1.1: Simplified chart of the nuclides.

It follows then, that one of the first questions posed by nuclear science might be the limits of nuclear existence (including the search for the heaviest at the upper right of the chart). Once boundaries, or the so-called limits of stability are experimentally determined (even in part), then the quest for understanding properties of all nuclei inside these boundaries suggests follows.

From an experimental standpoint, an entire hierarchy of the observable properties of an unknown nucleus is open to study. These properties range from the mass, half-life and decay modes, through the nuclear spin and moments, and on to detailed

spectroscopy of its energy levels. At present, the body of information available for a given nucleus depends largely on the difficulty of producing it in a nuclear reaction. Fusion/evaporation reactions and fission have provided the majority of nuclei during the last half-century of studies. In the last approximately 20 years, a third method, projectile fragmentation, has developed to the point that it is widely used to create new nuclei. The NSCL and a few other accelerator facilities were designed specifically to be nuclide factories based on the projectile fragmentation technique. These RNB facilities, distributed worldwide, are capable of delivering radioactive nuclei which can be studied to provide experimental observables such as nuclear masses (binding energies), half-lives, excitation energies and production cross sections.

1.1.2 Astrophysical Motivation

The task to completely characterize the nuclei within the limits of stability takes on greater significance if these nuclei are involved in astrophysical processes, making their properties important to understanding stellar evolution. In particular, since it is well accepted that the stars are the factories which build up nuclear mass (i.e., responsible for the creation of all nuclei in the universe beyond lithium), knowledge of the properties of nuclei are critical to understanding nucleosynthesis and the distribution of the elements in the universe.

More specifically, some of the processes in stellar nucleosynthesis are thought to involve nuclei far from stability. The r-process [1,2] and the rp-process [3] (see Figure 1.2) are the most prominent examples. In addition, energy evolution is a by-product of the nuclide building processes in stars and the reaction cycles that produce this energy often encompass radioactive nuclei. The participation of unstable nuclei (some far from stability as in the r-process) makes the study of RNBs vital to understanding the composition of our universe.

Nuclear astrophysicists attempt to understand the many processes taking place in stellar and explosive environments by using reaction rates to predict the distribution

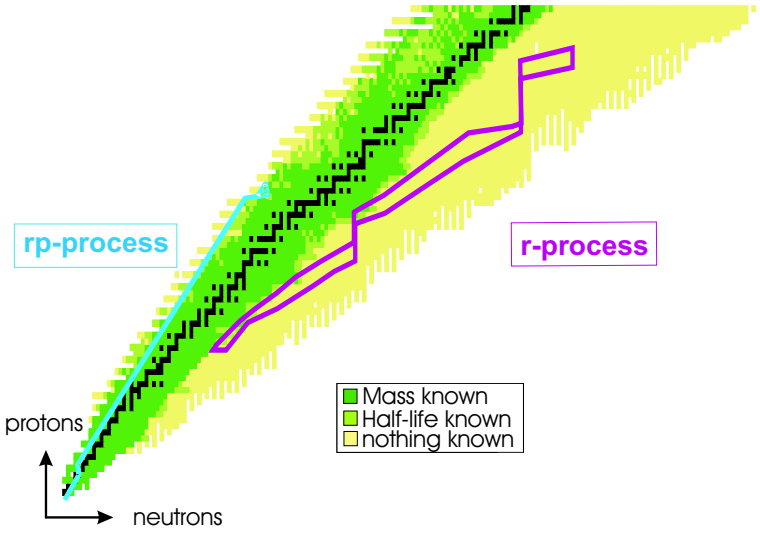

Figure 1.2: Chart of the nuclides with the approximate paths of the rp- and r- stellar nucleosynthesis processes.

of all elements in the universe. By using measured reaction conditions (temperatures, pressures, particle abundances) and measured reaction parameters (cross sections, decay rates, binding energies) in their network calculations, nuclear astrophysicists form models of the mass building processes and stellar evolution. Therefore, a primary contribution of nuclear physics to astrophysics is the measurement of specific properties of nuclei far from stability, especially those nuclei involved in one of the nucleosynthesis processes. The contribution of RNBs to astrophysics centers around the information on masses, half-lives, and cross sections and the reaction energetics and time scales which they represent. These data enter into calculations which attempt to model the formation and distribution of elements in the universe.

The need to gather data with high accuracy, achievable in "precision experiments," is crucial to providing greater constraints to both nuclear structure and nucleosynthesis models. The role of a gas stopping cell at a projectile fragmentation facility will be made clear in subsequent sections.

1.2 Precision Experiments

The kinetic energy per particle of the radioactive beam fragments produced at the NSCL is typically of the order of 100 MeV/nucleon (∼0.4c). The energies of these nuclei are suited to nuclear structure experimental techniques such as intermediate energy Coulomb excitation [4] and decay studies where the ions are implanted in a solid [5]. However, other precision studies [6, 7] require intensive manipulation of the radioactive ions and/or low beam energies. These requirements demand further treatment of the fast beams produced at a fragmentation facility before their use in such studies. Penning Trap mass measurements and selective ionization by lasers are two examples of such handling of ions for precision experiments.

Nuclear masses are a well-known example of the importance of precision experiments. Perhaps the most fundamental and essential property of a nucleus that can be measured is its mass [8]. It is, therefore, the measurement of this property which is first among efforts to study a particular nucleus. Ground state masses reflect the total of all interactions in the nucleus. Nucleon binding or separation energies are determined directly by mass differences. The separation energies point out the location of the boundaries of stability. In addition, mass differences give information on residual interactions (pairing) and deformations of the nucleus. Since mass differences are, essentially, the source of energy in stars, knowledge of binding energies constrains nucleosynthesis calculations.

Continuing with our example of nuclear masses, the need for precision mass measurements can be illuminated with the following illustration (Figure 1.3). The case for the rubidium (Z=37) isotones is presented [7], where the mass differences from 6 different models are plotted as a function of neutron number. In the region where the masses have been measured, model predictions show excellent agreement. However, above N=64, where masses have not been measured, the models diverge wildly. Clearly, accurate and precise mass measurements of nuclei far from stability would

provide a significant test for these models.

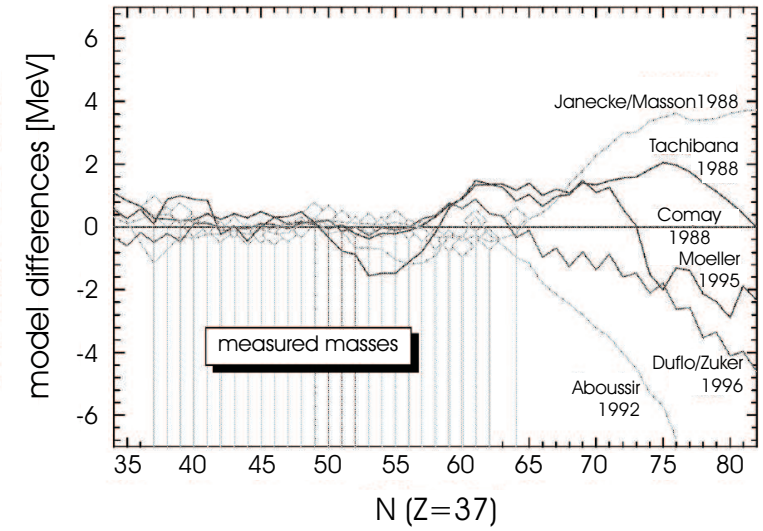

Figure 1.3: Comparison of mass model calculations for Z=37 isotones [7].

1.2.1 Penning Traps

To date, the most precise mass measurements are being performed with Penning Traps. Although trap measurements have the capability to contribute in other areas, their ability to directly determine nuclear masses with extreme precision on just a few ions has made them the choice for these studies.

By using a static electric quadrupole field, provided by a ring electrode and hyperbolic caps (Figure 1.4) combined with a strong, static homogeneous magnetic field, the measurement of even a single stable or long-lived ion can yield an accurate mass.

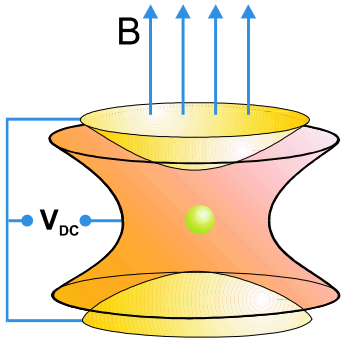

Figure 1.4: Simplified Penning Trap diagram.

In principle, Penning Traps act as high precision mass spectrometers by measuring the cyclotron frequency, ν_c, of stored ions.

$$\nu_c = (q/m) \cdot (B/2\pi) \tag{1.1}$$

where q is the charge of the ion, m is the sought after mass and B is the magnetic field of the trap.

The difficulty with these measurements is they require injection of ions into the trap at an extremely low and accurately controlled velocity; that is, a kinetic energy on the order of eV is necessary.

1.2.2 Mass Measurements

The measurement of nuclear masses fall largely into two categories: indirect (such as reactions and decay measurements) and direct (mass spectrometers, ion traps and time-of-flight) methods. While the indirect methods have produced mass precisions below the 100 keV level [9], they are usually not suited to measure masses far away from stability, as such nuclides' masses would be dependent on a chain of measurements with diminishing statistics as one studies nuclei further from stability. And, though a direct time-of-flight (TOF) method [10, 11] is suitable for exotic (far from stability) nuclei, its precision is typically limited to ~100 times worse than Penning Trap measurements.

Penning Traps have been used to measure the mass of ions with half-lives as low as 65 ms [12] or with as few as one stable ion. The resolving power and statistical accuracy depend on experimental conditions. The resolving power, R, is given as

$$R = \nu_c / \Delta\nu_{c(\mathrm{FWHM})}, \tag{1.2}$$

which depends on an observation time limited by the decay of the exotic nucleus

under study,

$$\Delta\nu_{c(\mathrm{FWHM})} \approx 1/\mathrm{T_{obs}}. \tag{1.3}$$

The accuracy of the mass determination is written

$$\delta \mathrm{m/m} \approx 1/(\mathrm{R} \cdot \mathrm{N}^{1/2}), \tag{1.4}$$

where N is the number of detected ions. Thus, the efficient collection and delivery of very short-lived ions to the trap is key.

Typical Penning Trap results have an accuracy of 10^{-7}, which translates to a mass uncertainty of $10-20$ keV. Increasing the number of ions detected and improving the emittance of the ion beams could improve this accuracy by a factor of 100. So, while the current knowledge of masses of nuclei away from stability are often known only to a few hundred keV (and the masses of nuclei far from stability are mostly unknown), Penning Trap data could improve on the statistical precision of many of these same nuclei by factors of 10 to 100.

1.3 The NSCL Gas Stopping Cell

The importance of precision experiments in the realm of nuclear science has been clearly established. In this section, the case for the construction and operation of a gas stopping cell at a fragmentation facility will be presented.

1.3.1 Production and Use of Radioactive Beams

The production of radioactive beams is dominated by two methods: Isotope Separation on Line (ISOL) and Fragmentation (or in-flight separation). As will be shown, these methods are complementary rather than competing techniques–each has its own niche in the scheme of nuclear physics experimental work. The variety of beams, beam energies and beam qualities that each offers is valuable to nuclear physics.

Isotope Separation On Line (ISOL)

The ISOL facilities generally have peak production for neutron-deficient nuclei near the valley of stability with large chemical selectivity. The typical ISOL facility makes use of a production accelerator which accelerates a light beam, often protons, at a thick production target (see Figure 1.5). The neutral reaction products diffuse from the target matrix and out through a transfer tube to an ion source where they can be selectively ionized. The ions leaving the ion source are accelerated to low energies before they are electromagnetically separated. Post-acceleration is possible, but not necessary for mass measurements.

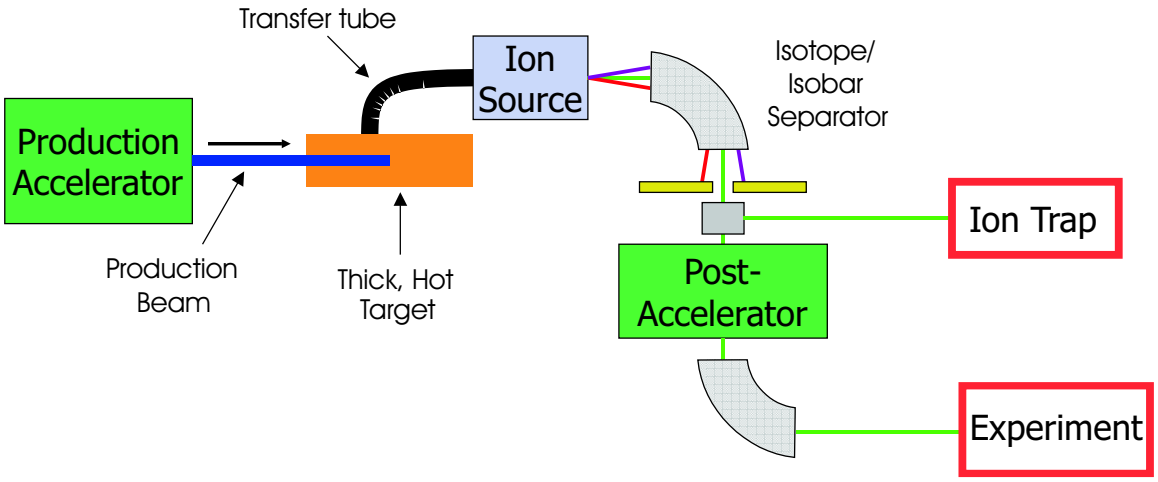

Figure 1.5: The ISOL (Isotope Separation on Line) method for production of radioactive beams.

While this method suffers from the dependence on the chemistry of the reaction products as they diffuse from the target, its more severe limitation, when compared to fragmentation methods, is the effect of the diffusion time on yield through the half-lives. Usual transfer times are on the order of one second. Although short-lived nuclides ($\sim$100 ms) have been measured with this method in special cases. Neglecting the types of beams produced, however, ISOLs superior feature is the excellent beam quality (low emittance and precise energy) which is well suited for precision studies.

Projectile Fragmentation (In-flight Separation)

The forte of fragmentation facilities is the rapid delivery of nuclei far from stability. A fragmentation facility relies on, most often, the acceleration of a heavy beam of ions (up to ~0.5c) directed at a thin production target (see Figure 1.6). Heavy projectiles which encounter target nuclei can be abraded, giving a variety of forward-focused fragments, which are separated, *in flight*, by a fragment separator utilizing strong magnetic fields in the so-called Bρ - ΔE - Bρ technique [13–16].

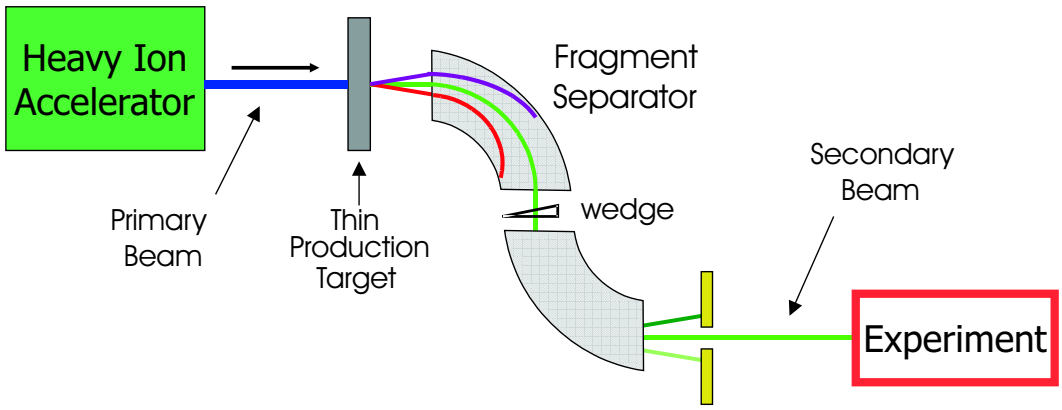

Figure 1.6: The fragmentation method for production of radioactive beams.

Comparison of ISOL and Projectile Fragmentation Methods

The nuclear reactions at the heart of the two techniques are very similar. Generally, a high kinetic energy beam interacts with a target creating a broad range of nuclei and fission products. The major difference is that projectile fragments retain their high velocity while ISOL target fragments are created essentially at rest (in the laboratory frame). Collecting and separating out high velocity residues is clearly a different task from sorting out a thermalized mixture of target residues. The projectile fragmentation process with in-flight separation has been extremely successful in providing fast beams of the most exotic nuclei.

Compared to the ISOL method, fragmentation provides more exotic beams, but the beam velocity remains high and the optical properties of the beam are poor due

to the effects of the target and wedge specifically, the fragments retain most of the velocity of the accelerated heavy ion beam. They can have a large emittance and non-negligible momentum spread which is proportional to the acceptance of the separator and the yield. Finally, depending on the desired nuclide, beam purities can vary over a wide range (1-99%), although the capability to perform beam tracking can aid the experimenter in dealing with background.

In the case of certain beams, especially those very far from stability with short half-lives, it would be beneficial to unite the best features of the two production methods, thereby allowing precision measurement of nuclides previously unavailable. It will be shown that adding the capabilities of a gas stopping station to a fragmentation facility (NSCL) is essential to making precision measurements on the most exotic nuclei.

1.3.2 The NSCL

The National Superconducting Laboratory (NSCL) at Michigan State University is an example of a third generation fragmentation facility [17]. The first dedicated device was the LISE separator at GANIL [18]. Second generation and improved separators included the A1200 at the NSCL [19], the FRS at GSI [20], and RIPS at RIKEN [21]. With the recent upgrade completed of the Coupled Cyclotron Facility (CCF), the NSCL has expanded the explorable regions of the chart of nuclides up to the mid-mass region (A$\sim$120), extending nuclear science experimental possibilities closer to (or out to) the limits of stability (Figure 1.7).

The A1900 Fragment Separator at the NSCL has the largest acceptance of any such device and can provide beam with magnetic rigidities up to 6 T·m and with a momentum spread of $\pm$2.5% [22]. The A1900 uses a system of superconducting dipole and quadrupole magnets (see Figure 1.8) to separate the beam fragments by mass/charge ratio, making a Bρ selection in the first half, matched energy loss in the middle and a second Bρ selection in the second half.

The beams resulting from the fragmentation and subsequent separation can then

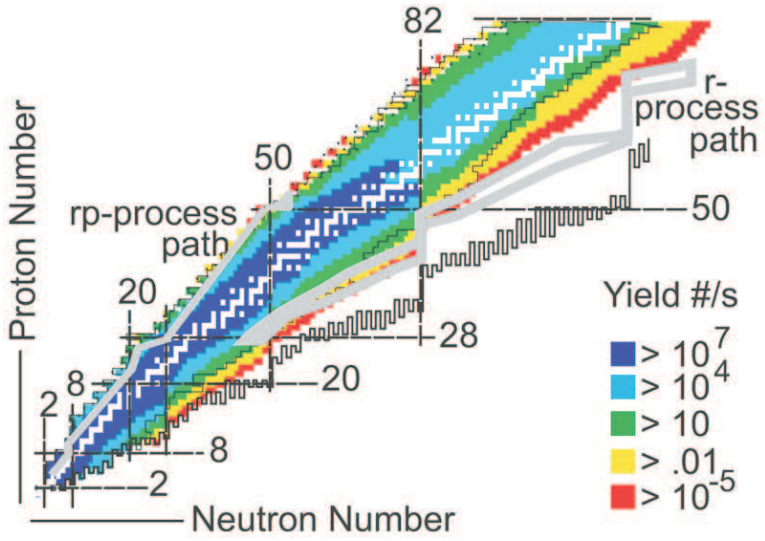

Figure 1.7: Beam production rates for the Coupled Cyclotron Facility (CCF).

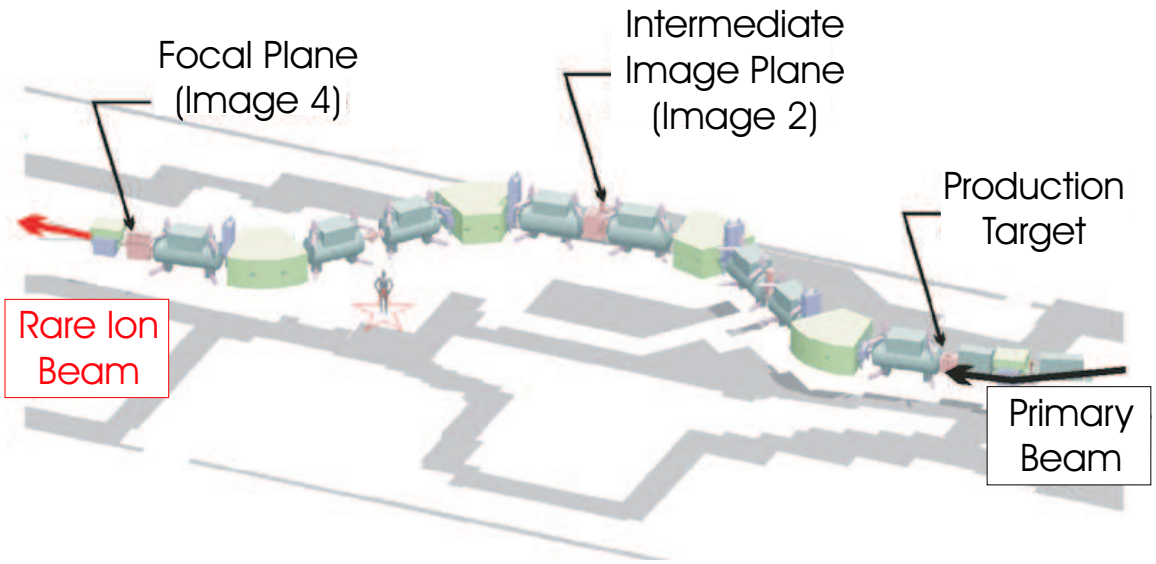

Figure 1.8: The A1900 Fragment Separator.

be delivered to experimental endstations. The properties of these beams are highly disjoint with the requirements for precision experiments (Table 1.1).

Again, many of these required beam qualities are characteristic of beams created at an ISOL facility. However, the desire to produce radioactive beams far from stability (fragmentation facility) *and* to produce them with these excellent beam qualities necessary for precision measurements is the greatest motivation for our gas stopping efforts.

Table 1.1: Properties of Fragmentation Production beams compared to Requirements for Precision Experiments

Fragmentation production provides:	Precision Experiments require:
High energy beams (∼100 MeV/nucleon)	Extremely low energy (∼1eV/nucleon)
Large energy spread	Low energy spread
Large emittance	Low emittance
DC beam	Pulsed beam
Possible contaminants	Pure beams

1.3.3 LEBIT Methods and Objectives

To have the best of both worlds (very rare beams and good beam quality), we are developing a gas stopping device. The requirements are stopping the fast radioactive beams and re-emitting them at lower energies with low angular energy spread. Creating such an ion source is the leading objective for the collaboration at the NSCL known as LEBIT (Low Energy Beam and Ion Trap). LEBIT [23] intends to stop ions in a buffer gas, strip the gas off and transport the ions to endstations for precision experiments. The first experiment will be mass measurements in a Penning Trap (already under construction).

The LEBIT method to stop fast radioactive beams is similar to that described by Geissel *et al.* [24]. The incoming ion beam will be met in the beamline vacuum by degraders which will attenuate most of the beam energy (see Figure 1.9). With their remaining energy, the ions will pass through a thin window acting as the pressure barrier between vacuum and the ∼1 bar helium in the gas cell. The degraders must be variable as to allow the experimenter to take away the proper amount of energy from the ions such that the ions will come to rest in the helium gas, with the greatest stopping efficiency. Through a combination of electric potentials and gas flow, the ions (and the helium) will be extracted through a nozzle. The ions will be captured in an ion guide while the helium will be skimmed away in a differentially pumped system. The ion guide will direct the ions downstream to the experimental endstations for precision studies.

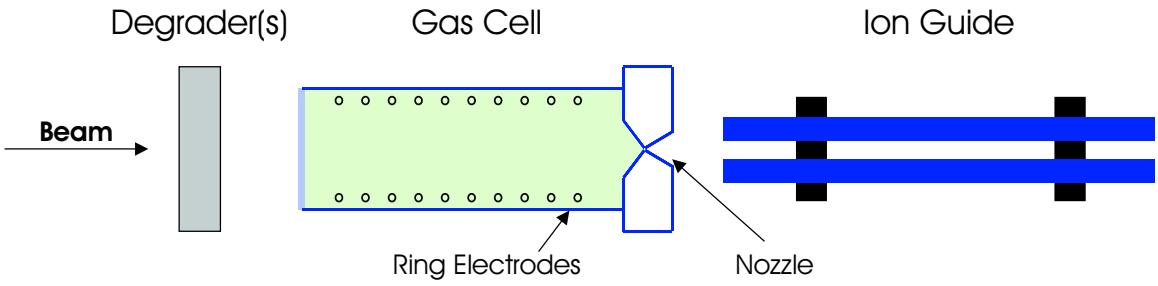

Figure 1.9: Diagram of simplified gas stopping concept.

1.3.4 Similar Efforts

The NSCL is not alone in its attempt to construct and operate a gas catcher. The expanded opportunities that a gas stopping cell can offer are being introduced at several high energy facilities: Argonne (Illinois), SHIP and FRS (GSI, Germany), and RIKEN (Tokyo, Japan).

The ion stopping and collection in a helium buffer gas follows on the IGISOL (Ion-Guide-ISOL) system [25, 26] developed originally at Jyväskylä, Finland, and implemented in several labs around the world [27,28]. The name implies the IGISOL technique is a version of ISOL that relies on thermalization of the products, close to or even containing the target, in a buffer gas. This technique is now applied to thermalize fast reaction products that already have been separated.

As shown in Table 1.2, a variety of cell sizes and pressures are under development. The RIKEN gas cell extracts ions at right angles to the beam direction from a long (two meter) gas cell. Although helium appears to be the stopping gas of choice, argon has been tested.

While it seems clear that the gas cell should have the highest pressure gas with the highest atomic number in order to have the greatest stopping power for fast ions, several other factors must be considered. High atomic number gases such as krypton and xenon are efficient stopping media but they are relatively polarizable and form adduct compounds with the ions that slow their migration and need to be broken before the ions are usable.

Table 1.2: Comparison of gas stopping efforts [29].

Lab, Location	Gas	Cell Length	Gas Pressure	Incoming Beam Energy [MeV/A]
ANL, Argonne [30, 31]	He	20 cm	150 mbar	∼5
GSI, Darmstadt (SHIP) [32]	He, Ar	18 cm	100 mbar	∼5
RIKEN, Japan [29, 33]	He	200 cm	130 mbar	∼50
NSCL Gas Cell	He	50 cm	1 bar	∼100
GSI, Darmstadt (FRS) [31]	He	125 cm	0.5 - 1 bar	100 - 1000

The most prominent aspect of the NSCL's initiative is the incoming beam energy which the gas cell will meet, highlighted in the last column of Table 1.2. The beam energies of the NSCL's Coupled Cyclotrons are typically above 100 MeV/nucleon–greater than the energies of beams being introduced into the other gas cells (the gas cell listed last in Table 1.2 is only beginning to come online). This fact makes the attempt to efficiently stop and quickly extract rare, short-lived radioactive beams even more challenging due to the growth of the residual energy distribution as the ions slow down. We have chosen to use a high pressure gas cell with static electric drift fields. A novel feature of the cell is that a bias will be applied across the extraction nozzle itself.

Similarly, the beam energies encountered at the NSCL's gas cell also figure prominently into the possibility of stopping beams at the next (planned) radioactive beam facility, RIA (The Rare Isotope Accelerator). Currently, the ∼100 MeV/A energies of the NSCL are nearest the planned beam energies of ∼400 MeV/A at RIA. The prospects of gas stopping at RIA will be greatly influenced by the NSCL experiments.

1.4 Overview of LEBIT / Gas Stopping Station

Radioactive beams from the A1900 Fragment Separator will be delivered to the N4 Vault at the NSCL. The fast beam will be degraded and brought to rest in the high-pressure helium in the gas cell of the Gas Stopping Station (see Figure 1.10).

A combination of electric potentials and gas flow will extract the helium and ions through a nozzle. The ions will be captured in a radiofrequency quadrupole (RFQ) ion guide while the helium will be skimmed off in a differentially pumped system. The now low energy beam will leave the shielded N4 Vault and the Gas Stopping Station and travel via the LEBIT beam optics into the accumulator/buncher. From here the pure, low-energy, low-emittance ion beam will be delivered in pulses to an endstation for a precision measurement. Currently, a 9.4 Tesla Penning Trap is under construction to perform precision mass measurements.

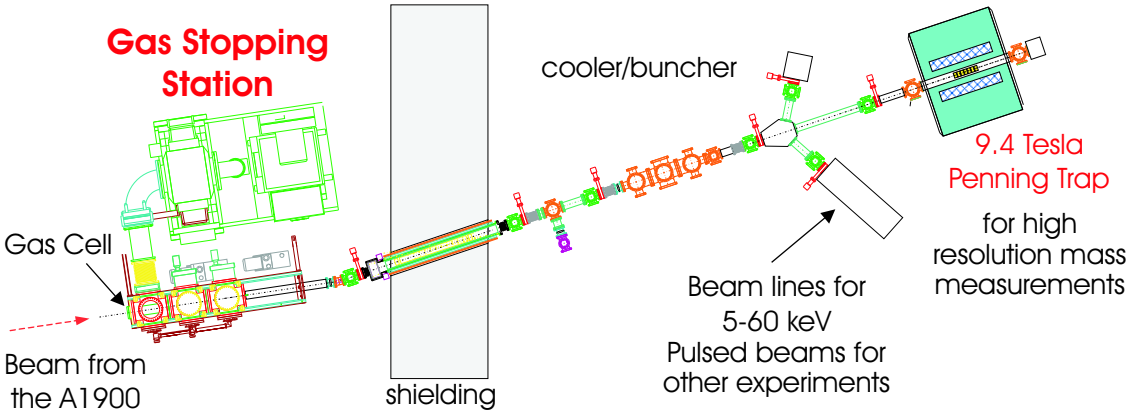

Figure 1.10: Overhead view of LEBIT (Low Energy Beam and Ion Trap).

Closer examination of the Gas Stopping Station (the focus of this work) in Figure 1.11 illustrates the main features of the gas-stopping scheme. The beam energy will be attenuated by a pair of variable glass degraders and a mono-energetic wedge, both of which are discussed in Chapter 2. Ions pass through the thin beryllium window and are stopped (with maximum efficiency) in the high-pressure helium of the gas cell, a re-entrant chamber in Cross A of the system.

Extraction will be performed by electric potentials (inside the gas cell) and gas flow through a supersonic nozzle. The ions will then be captured in the RFQ ion guide while the helium is skimmed off and removed from Crosses A, B and C by the high-capacity differential pumping system . The ions are then transmitted by the LEBIT beam optics downstream to the accumulator/buncher for preparation for use

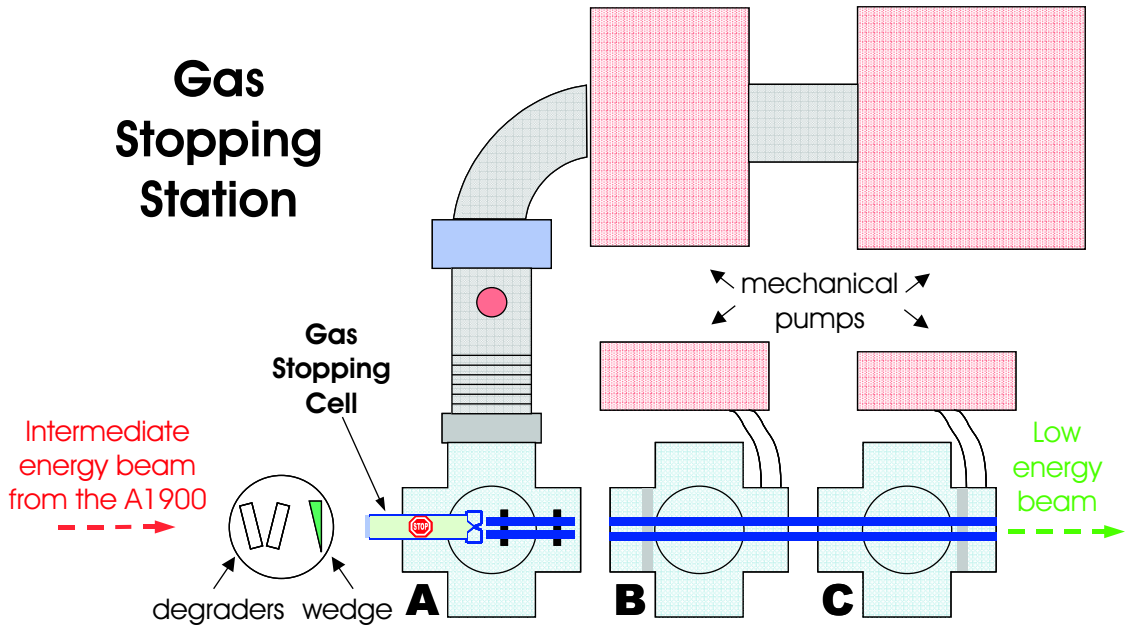

Figure 1.11: Overhead view of the Gas Stopping Station.

in precision studies.

1.5 Thesis Organization

This thesis will be organized into chapters which detail the trials of the two significant challenges of constructing the new ion source: stopping and extraction.

A series of experiments to measure the energy distributions of primary (mono-energetic) and secondary (up to $\pm 1\%$ in momentum) beams in the helium gas are described in Chapter 2.

The details of gas flow through the nozzle and an orifice were measured prior to assembly of the extraction system and are given in Chapter 3.

The results of ion extraction studies with radioactive ions under operating conditions are given in Chapter 4.

A summary and considerations for further work is given in Chapter 5.

Chapter 2

Gas Stopping

2.1 Energy Loss of Ions in Matter

2.1.1 Background

Heavy ions ($A \gtrsim 4$) passing through matter interact largely through the coulomb force with orbital electrons of the absorber atoms. Although elastic and inelastic interactions of the ions with absorber nuclei are possible, such interactions are rare and contribute little to the energy loss of the ions. The velocity of the ions are decreased as a result of their interactions, ionization or excitation, with absorber electrons.

For ions in a given absorber, the *linear stopping power*, S, is given as the differential energy loss for the ion in the absorber divided by the corresponding differential path length [34]:

$$S = -\frac{dE}{dx} \tag{2.1}$$

The *range*, or path length, R, can then be defined as:

$$R(E_0) = \int_0^{E_0} \frac{dE}{S} \tag{2.2}$$

The range of an ion in an absorber is most often determined experimentally, and so

we limit our discussion to stopping power.

The magnitude of -dE/dx along the path length is also named the *specific energy loss* and is given by the Bethe formula:

$$-\frac{\mathrm{dE}}{\mathrm{dx}} = \frac{4\pi \mathrm{e}^4 \mathrm{q}^2}{\mathrm{m}_0 \mathrm{v}^2} \mathrm{NZB} \tag{2.3}$$

where

$$\mathrm{B} \equiv \left[\ln \frac{2\mathrm{m}_0 \mathrm{v}^2}{\mathrm{I}} - \ln \left(1 - \frac{\mathrm{v}^2}{\mathrm{c}^2} \right) - \frac{\mathrm{v}^2}{\mathrm{c}^2} \right] \tag{2.4}$$

In both Equations (2.3) and (2.4): v and qe are the velocity and charge on the projectile, m_0 is the electron rest mass, e is the electronic charge, I is the average excitation and ionization potential of the degrader and N and Z are the number density and atomic number of the degrader [34].

2.1.2 Energy Loss Models

The Bethe formulation has been known some 70 years. Improvements, in the form of corrections to this formula, have been added continually since this time, but have accelerated greatly in the last 20 or so years. Probably the most widely used models which are pertinent to the energy range of our experiments are the Hubert, Ziegler and ATIMA codes.

The Hubert model [35] is actually a series of range and stopping-power tables for 2.5 - 500 MeV/A heavy ions stopping in solids. The model centers around a semi-empirical formula for a heavy ion effective charge parameterization that was derived from a set of nearly 600 data points. The data covered projectile mass from ^{16}O to ^{238}U in the 3 - 90 MeV/A range interacting with targets from beryllium to uranium. This model is focussed on ions stopping in solids, however, so such an empirically parameter dependent calculation may not be expected to model gas stopping precisely.

Probably the most frequently used predictor for slowing down heavy ions is SRIM (The Stopping and Range of Ions in Matter) [36] based on the model of Ziegler *et*

al. [37]. The theoretical base of the Ziegler model is grounded in the Bethe-Bloch concept; however, this tabular collection of stopping powers also includes a number of free parameters that are continually updated (normalized) to the growing volume of experimental data.

The ATIMA (ATomic Interaction with MAtter) code [38] is a direct calculator which incorporates the classical Bethe-Bloch theory. Additional terms are included which take into account such effects as the dielectric polarization of the stopping medium (density effect), shell corrections for the binding energy of target electrons and displacement of the electrons during collisions (Barkas term). Finally, ATIMA can also incorporate theory by Lindhard and Sørensen (LS) which makes corrections for high and relativistic energy ions [39].

The software LISE [40, 41] has great utility as both a stopping power calculator and as an estimator of rates of production of secondary beams. For stopping power predictions, LISE allows the selection of one of three energy-loss models: Hubert, Ziegler and ATIMA. The code allows the user to include all of the materials in the path of the beam and the effects of simple ion optics.

2.2 Introduction to Gas Stopping

The goal of our gas stopping initiative was efficient stopping to study rare beams in a gas which would allow for quick extraction of short-lived ions and further manipulation of the ion beam. This chapter is devoted to ion stopping experiments performed on both stable, mono-energetic (primary) beams and on radioactive (secondary) beams. The primary beam trials helped us to initially characterize and test our gas stopping system while the secondary beam stopping runs were the final objective of the gas stopping tests.

2.2.1 Design Considerations

In order to construct a working gas stopping cell which would be efficient for a wide range of nuclide atomic numbers and energies, many parameters were first carefully considered and studied. The challenges of bringing ions traveling at nearly half the speed of light to rest in a gas were many. A gaseous collector is a relatively thin stopping medium. In addition, energy-loss straggling and angular straggling will add to the spread of the spatial distribution of ions stopping in the gas.

Ion Stopping in Gases

As mentioned in the motivation, in order to intensely manipulate the ion beams for making precision measurements, we had to stop the ions not in a solid, but in a gas. For our purposes, we knew that we had to attenuate most of the fast radioactive beam's energy ($\sim$100 MeV/A) with degraders such that a gas cell of reasonable length could remove the remainder of the energy and finally stop the ions.

Immediately the disparity between the densities of solids and gases (typically a factor of 1000) is obvious. The stopping of heavy ions in a solid is well studied. However, of stopping of ions in a gas, there is less known. One might consider making a very long (on the order of several meters) gas stopping cell, but this is not a practical use of laboratory space and, as discussed in the next chapter, would require too much time to evacuate the interesting short-lived ions. The more promising approach would degrade the beam's energy upstream from the gas cell and then have the gas remove the remainder of the beam's energy while bringing the ions to rest. The task is to remove a very high percentage of the beam's energy with degraders and construct a relatively short accompanying gas cell. However, an important factor (and challenge) must be considered–the spread in the longitudinal distribution over which the ions stop, better known as energy straggling.

Energy Straggling Calculations

Energy loss is a statistical or stochastic process, governed by the random interactions of the projectiles with, primarily, the electrons in the absorber. A spread in the resultant energies (and therefore ranges) occurs even for a beam of mono-energetic particles passing through any material. The width of the energy distribution is a measure of *energy straggling* [34]. While the amount of straggling encountered when stopping ions in a solid is small, gas stopping presents a very different situation. A simple SRIM [36, 37] calculation was performed to model a mono-energetic ^{40}Ar primary beam at typical NSCL energies impinging on a 7 mm thick foil of beryllium (Figure 2.1). Shown in the figure is the characteristic narrow width of ions stopping

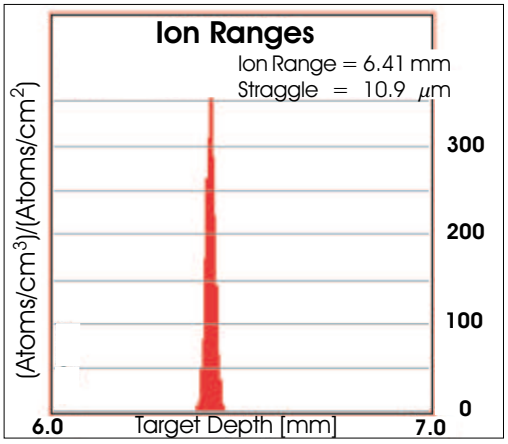

Figure 2.1: SRIM calculation resulting showing narrow stopping distribution of 100 MeV/A ^{40}Ar ions in beryllium metal.

in the solid material. In this case the range is 6.410 mm with a straggling of 0.011 mm, a relative range/straggling value of only 0.0017. The straggling in the SRIM calculation is precisely defined as the square root of the variance of the distribution.

If we were to pass the same beam through 20 μm less (that is, 6.390 mm) beryllium and allow the energy attenuated ions to come to rest in 1 bar of helium gas in a cell sufficiently long to stop them, we would have the results shown in Figure 2.2. Now 194 mm of helium gas at one bar is required to remove the residual energy and the increased straggling of ions in the gas is very visible. Here the straggling (width) is

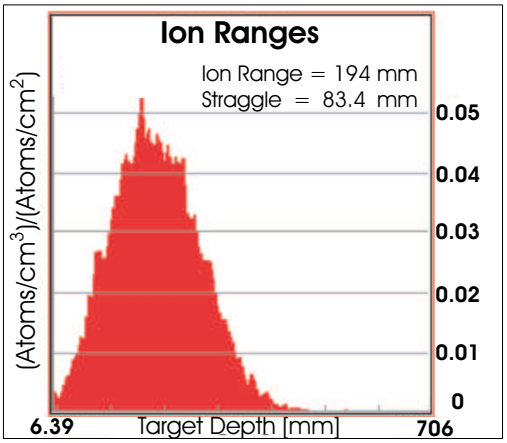

Figure 2.2: SRIM calculation showing an expanded stopping distribution of 100 MeV/A ^{40}Ar ions coming to rest in helium gas after being degraded in beryllium metal. Note that in this case, the x-axis represents nearly 700 mm of gas.

83.4 mm, and the relative range/straggling becomes 0.43 for the same mono-energetic beam. For completeness SRIM calculations were performed for the stopping of the same argon beam in helium gas alone. Not surprisingly, 53.4 m of helium gas would be required to stop the 100 MeV/A beam, but the straggling of approximately 100 mm is comparable to the straggling in the beryllium/helium shown earlier.

The usual way that target materials are compared is in terms of mass thickness (or aerial density). Mass thickness has units of mass/area, and is simply the density of a material multiplied by its actual thickness. This unit relies on the fact that nuclei are extremely small and that thin pieces of ordinary, randomly ordered materials will appear to a high energy beam as if all the atoms were in a single layer. In this way, materials are placed on a basis that factors out their densities. Comparing the mass thicknesses of materials leaves only their atomic numbers, Z, as the factor which contributes to their differing stopping powers. Now, returning to the SRIM calculation in Figure 2.2, we see that the 6.39 mm of beryllium that removes the bulk of the energy has an equivalent mass thickness of 1180 mg/cm^2, while the final volume of helium at 1 bar, 22 degrees Celsius and 50 cm in length would have a mass thickness of only 9.8 mg/cm^2. This illustrates the difficulty of attempting to remove most of the beam's energy in a relatively thick degrading material before stopping

the ions in a 'thin' amount of gas.

The first gas stopping tests at the NSCL were performed by Baumann *et al.* [42]. These tests used an ^{36}Ar at 100 MeV/A with an aluminum degrader to stop ions in a volume containing various pressures of helium gas. They determined that the homogeneity of the energy degrader and the energy spread of the beam were significant parameters in determining the range distribution of ions stopped in the gas.

This result implies the largest challenge for our gas cell–the problem of the extended final distribution of the high energy ions in the gas. Clearly no design or equipment can reduce this statistical broadening of the stopping range. So, at best, we could hope to avoid *adding* to the width of the stopping, thereby keeping the fraction of ions stopped within the length of our gas cell at a maximum. Keeping in mind that the SRIM calculations above were performed for exceptional conditions (a mono-energetic primary beam passing through ideal degrader materials), we took every pain to minimize the amount of range straggling added by our system in anticipation of performing gas stopping under non-ideal conditions (secondary beams having a momentum spread passing through imperfect degrader materials).

2.2.2 Equipment

In its fully functional mode, the Gas Stopping Station is designed to stop ions in the gas cell, extract the ions and then deliver them to the LEBIT cooler/buncher before their use in precision experiments (previously diagrammed in Figure 1.10). A more detailed description of the important gas stopping equipment is shown in Figure 2.3.

Before arriving at the Gas Stopping Station, the beam passes through a thin plastic detector at the Intermediate Image of the A1900 Fragment Separator. This detector provides a particle count, helping us normalize the number of ions stopped in the many runs, while still allowing us to measure the magnetic rigidity of the resulting ions in the second half of the A1900. Further downstream, the ions encounter the first degrader materials, a pair of glass plates. These remotely controlled variable glass degraders

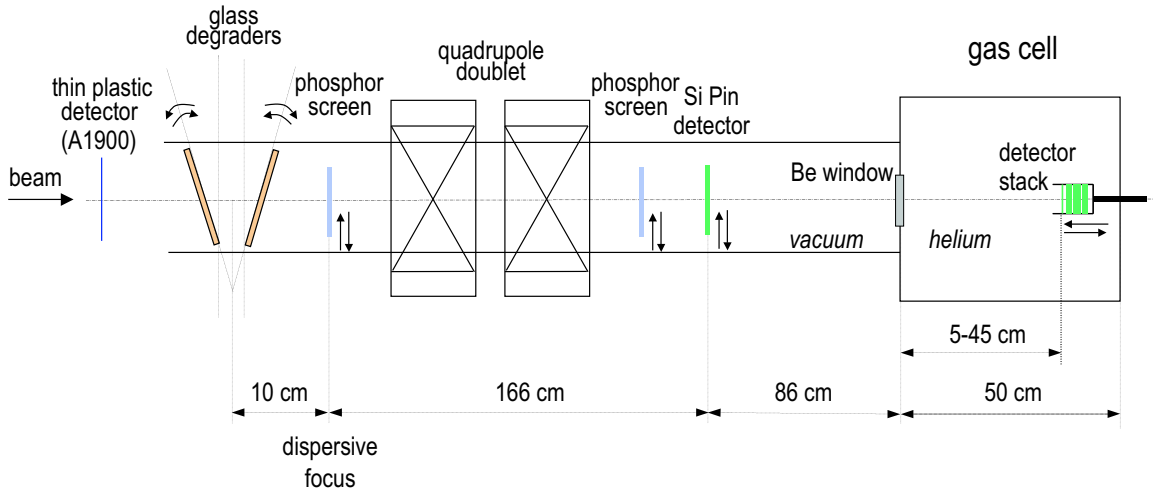

Figure 2.3: Schematic of gas stopping beamline and equipment.

are our only mechanism for precisely controlling the amount of energy removed from the beam, thus allowing the ions to stop in the gas cell with the greatest efficiency. At the dispersive focus (indicated in Figure 2.3), the (secondary) beam passes through a mono-kinetic wedge, where its energy distribution is compressed (more on this in subsection 2.4.1). The ions then are brought to a more parallel beam by the last superconducting quadrupole doublet magnet in the beam line. After the magnet, a large-area ($50 \times 50 \times 0.5$ mm) Si PIN detector can be moved in and out of the path of the beam to perform diagnostics and calibration. The beam leaves the vacuum of the beam line as it passes through the gas cell's window (beryllium) and enters the high pressure helium of the gas cell where it comes to rest. For the stopping trials reported in this chapter, the beam's path ends in the gas cell. The extraction and transport of ions in the gas stopping system will be discussed in later chapters. Finally, a set of silicon surface barrier detectors were placed in the gas cell to monitor the energies of the ions in the gas.

Recalling comparisons by mass thickness, a summary of the degrader materials follows in Table 2.1.

One of our imperatives was to minimize the amount of straggling contributed to the radioactive beam by our degrader materials. Therefore, exceptional care was

Table 2.1: Summary of degrader materials.

Degrader	Mass thickness [mg/cm^2] per cm material	Typical experimental actual thickness [cm]	Mass thickness [mg/cm^2]
Glass	2500	0.2	500
Beryllium window	1850	0.1	185
Helium (1 bar, 295K)	0.196	50	9.8

afforded to the quality of the materials selected in each of the energy loss media. More detail on the glass degraders and beryllium window follow.

Variable Glass Degraders

The majority of the beam's energy loss will occur in the variable degraders. In addition, the greatest flexibility in controlling energy loss will be due to our ability to precisely control the amount of material presented to the beam by these principle degraders. (Consider that the beryllium window is of a fixed thickness and that the helium gas has comparatively little stopping power.) For these reasons, it is critical that these degraders can be accurately adjusted and that they are of superior material which contributes minimally to the straggling of the beam's energy.

Optical quality glass was chosen as the material for the variable degrader. OPTIMAX Systems Incorporated was chosen as the manufacturer due to the specifications they were able to meet. BK7 Schott glass was used to construct plates of a rectangular prism shape. The area of the plates normal to the beam is 30 mm vertical $\times$ 90 mm horizontal. A variety of thicknesses were requisitioned in order to degrade a broad spectrum of ions and energies.

Four each of glass plates were manufactured and delivered of nominal thicknesses 1.2, 1.5, 2.0, 2.7, 3.6, 5.0 and 7.0 mm. The manufacturer was unable to consistently fabricate glass plates of a thinner dimension, thus only one plate each of 0.5 and 0.7 mm nominal thickness was delivered. Upon receipt of the glass plates, extensive measurements were recorded on their dimensions and mass (Table 2.2).

Table 2.2: Summary of measurements of glass degrader plates (averages are for that particular nominal thickness only)

Nominal thickness [mm]	Average measured thickness [mm]	Average Density [g/cm^3]	Density error [g/cm^3]
0.5	0.472	2.51	0.02
0.7	0.672	2.51	0.02
1.2	1.21	2.50	0.02
1.5	1.49	2.51	0.02
2.0	2.02	2.50	0.02
2.7	2.699	2.503	0.021
3.6	3.641	2.517	0.022
5.0	5.031	2.505	0.023
7.0	7.014	2.505	0.024
Errors	0.008		
Overall Averages		2.506	0.022

The specifications called for a surface roughness on the order of 10 nm, a maximum thickness deviation of 1 μm and a total homogeneity of better than 10^{-4}. Our thickness measurements using a precision micrometer showed surface deviations of less than 3 μm.

The glass degraders were mounted in a system that could be remotely controlled and had the flexibility to degrade a wide degrade of nuclides and energies without having to interrupt the experiment. The mechanism had pairs of glass plates opposite each other on two ladders. The ladders would counter-rotate against each other by the same angle (up to 45 degrees) perpendicular to the beam in the vertical plane in order to change the thickness of glass presented to the beam.

Counter-rotation and a pair of plates were incorporated into the design to cancel the effect of the small angular divergence of the beam, which would be the case for secondary beams. In this way, all beam particles would encounter the same degrading material. See Figure 2.4 and Table 2.3.

The ladder mechanism also allowed remote translation of the target ladder in the vertical dimension in order to select the glass plate pair of appropriate thickness. A schematic of the mechanism is shown in Figure 2.5.

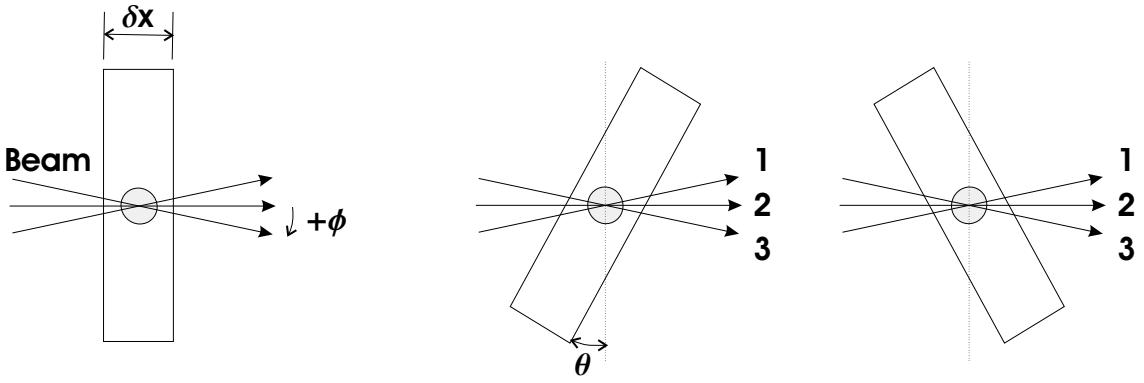

Figure 2.4: Counter-rotation of glass degraders. In the left portion, a single degrader plate is shown for clarity. The right portion shows the pair of plates counter-rotated about their centers.

Table 2.3: Cancelling effect of counter-rotated glass degraders. The approximation holds well for small beam angles, ϕ. For example, at a beam angle of 1 degree, the approximation is good to one part in 5000 for a glass degrader angle, θ, of 30 degrees.

Beam	Beam Angle	Plate A Contribution	Plate B Contribution	Total Thickness
1	$-\phi$	$\delta x/cos(\theta+\phi)$	$\delta x/cos(\theta-\phi)$	$\sim 2\delta x/cos\theta$
2	0	$\delta x/cos\theta$	$\delta x/cos\theta$	$2\delta x/cos\theta$
3	$+\phi$	$\delta x/cos(\theta-\phi)$	$\delta x/cos(\theta+\phi)$	$\sim 2\delta x/cos\theta$

Before each experimental run, the rotation control was calibrated such that the requested glass angle would match the angle actually produced by the target ladder mechanism. This was accomplished by first inserting a fitted rectangular form between the target ladders to ensure that they were parallel and at 0 degrees rotation. Next, after affixing a protractor which indicated the angle in degrees under a pointer attached to the target ladder drive, a series of angles were set by computer control and then measured. These data were plotted and show a good linearity as well as excellent agreement between the requested and measured angle. The error in the angle we assigned to be ± 0.25 degree. Since the degrader thickness increases with the cosine of the rotation angle, the combined thickness of the pair of degrader plates was chosen for each ion to minimize the angle on the glass, thereby minimizing the uncertainty in the thickness of the glass presented to the beam..

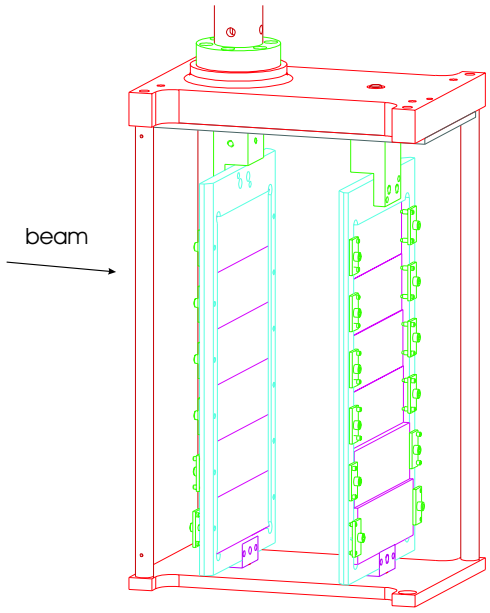

Figure 2.5: Mechanical drawing of glass degrader ladder. Each of the 6 plates of glass are 30 mm high $\times$ 90 mm wide and are of varying thicknesses. The drive mechanism above the ladders allows for remote manipulation of the angle of the glass.

Beryllium Window

The window's primary task is to act as a pressure barrier between the vacuum of the beamline and the high pressure (1 bar) of the gas cell. Ideally, the window should minimally impact the incoming ion beam. It should degrade the beam as little as possible, thereby allowing us more flexibility to attenuate beam energy using the upstream variable glass degraders. Also, like the glass degraders, the window should be of a homogeneity and flatness which would add as little as possible to the energy straggling of the beam.

To minimize the amount of energy loss caused by the window, the window should have two features. First, it should be as thin as possible while still able to function as a pressure barrier. Second, it should be made up of a material of low effective atomic number, Z, as the amount of energy loss scales with the Z of the absorber.

To minimize the contribution of energy straggling by the window, it should possess two further characteristics, like those of the glass degraders. First, it should be made of a very homogeneous material. Second, the surfaces of the window should be parallel,

smooth and flat. In addition, the window must not be too thin that it would deflect due to the difference in pressures on its two surfaces, as a window with a curvature would not present the same thickness of material to all incoming ions.

During preliminary trials on the stopping of primary beam, we used a disc-shaped stainless steel window, cut from metal sheet, of thickness 0.59 mm. The stainless steel window proved a thin but effective pressure barrier for these experiments. However, due to its possible inhomogeneity and poor surface characteristics, it was a potential significant contributor to the energy straggling.

Our next (and current) generation window was formed from beryllium. Initially, a pair of 1.5 mm thick, disc shaped windows (diameter 53.2 mm) was ordered from Brush Wellman Incorporated. We specified a flatness tolerance of 0.0005 inches (13 μm) with a surface finish of 8-16 micro-inch (0.2 - 0.4 μm). Our measurements of the windows showed an actual thickness of 1.499 mm and that the thickness range (flatness) was within 5 μm of this value. Assay of the windows performed by the manufacturer showed them to be 99.8% beryllium, the balance being trace amounts of other metals. We used gold o-rings (1 mm thickness, from Scientific Instrument Services, Incorporated) to form the vacuum seal which was successfully tested down to the 10^{-6} mbar range.

To give us greater versatility using the glass degraders for energy attenuation, we explored the possibility of using a thinner beryllium window. Before ordering the 1.5 mm thick windows, Jack Ottarson, of the NSCL, performed deflection calculations using a finite elements analysis for the static displacement. This result showed a deflection of 0.015 mm. A later calculation gave a deflection of only 0.050 mm for a beryllium window thickness of 1 mm. With this knowledge, a second pair of windows (1 mm thickness) was ordered from Brush Wellman using the same specifications. On receipt of the windows, our measurements found their thickness to be 1.022 mm, with a flatness within 10 μm of the thickness.

2.3 Primary Beam Measurements

The first attempts at gas stopping in the new system concentrated on stable, primary beams accelerated by the Coupled Cyclotrons and passed through the A1900. Such beams are as close to ideal as possible. They are nearly mono-energetic, have little momentum spread (determined by measuring the size of the beam spot in the dispersive image of the A1900, and typically on the order of $\Delta p/p \sim 0.07\%$) and are relatively easy to produce. By using the simplest possible beams, we could most easily observe the effects on stopping of small changes made in our gas stopping equipment.

2.3.1 Experimental Setup

The Coupled Cyclotrons accelerated and the A1900 delivered eight different primary beams of fully-stripped ions to the Gas Stopping Station in the N4 vault at the NSCL. After energy attenuation in the variable glass degraders and the beryllium window, the ions entered the gas cell. The helium (assumed to be at room temperature) pressure in the gas cell was read by a MKS Baratron 722A capacitance manometer (10,000 torr full range, controlled by an MKS 937A Multi-Gauge Controller).

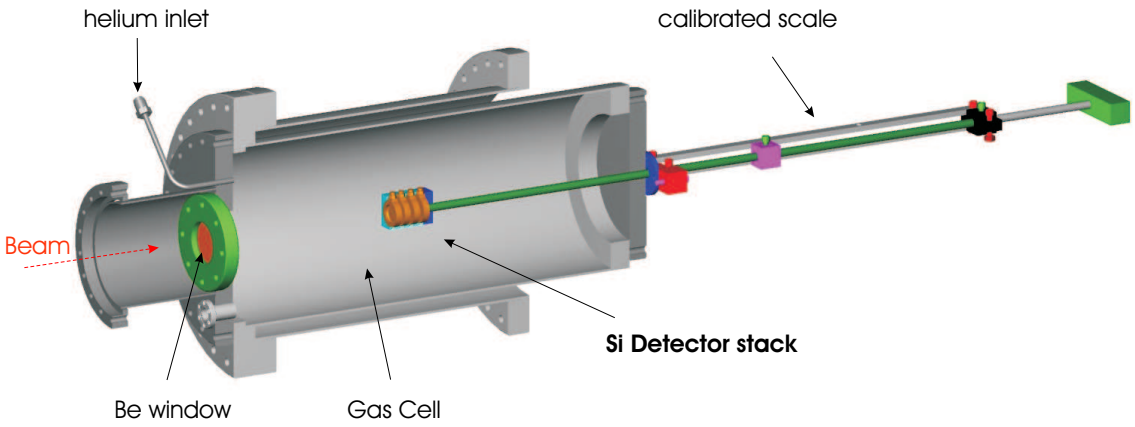

Figure 2.6: Moveable silicon detector stack on the beam axis inside the gas cell.

A stack of four silicon detectors (300 mm^2 active area and, in order, 0.1, 0.5, 1.5

and 0.5 mm thick) was mounted on a post, moveable along the beam axis, from the downstream side of the gas cell (Figure 2.6). These detectors were used for particle detection and identification and, ultimately, to determine the fraction of ions stopping in the gas cell. Detector pulses were immediately amplified by a Tennelec TC178 charge-sensitive preamplifier and the channels were checked with a complementary Tennelec TC 178P pulser. Data acquisition was triggered by constant fraction discriminators (CFDs).

Normalization of counts in the silicon detectors was aided by the introduction of a thin plastic scintillator ($\sim$28 mg/cm^2) at the dispersive plane of the A1900. Using the counts from this scintillator, variations in the delivered beam intensity could be factored out.

The primary beam was attenuated to give approximately 500 particles per second during each of the one to two minute data taking runs. This counting rate kept the data acquisition dead time low and was well within the operating limits of the silicon detectors.

Calibration of the silicon detectors was accomplished by removing the degrader glass and helium gas, thus causing the beam to pass through the entire stack. Comparing the resulting ΔE peaks with stopping power calculations provided the energy calibration. Several additional calibration points were measured by introducing thin (known thickness) detectors or degraders into the beam's path. Uncertainty in the energy calibration, which depends on calculations [37, 43], is approximately 3-5%.

Before examining data on primary beam, we should comment on the magnetic rigidity, or Bρ (give in units of Tesla·meter), of the magnetic elements in the A1900 separator and the beam line. As mentioned, the momentum distribution for our primary beam was estimated at 0.07(1)%. The central momentum of the beams was known to $\sim$0.1% from the values of Bρ of the A1900 magnets. The degraded beam will have a lower Bρ than the fully accelerated beam. Therefore, in all stopping trials, the value of Bρ in the last superconducting quadrupole doublet (see Figure 2.3), which

is positioned after the glass degraders, was set to the appropriate value given the energy of the degraded beam. This adjustment ensured the consistency of beam optics. Calculation of these values was performed with the energy module of the computer software LISE.

2.3.2 Primary Beam Stopping Data

Measurements were performed on primary, mono-energetic beams over a range of eight energies and nuclide masses. As a representative measurement, we offer the data from stopping tests of 150 MeV/A ^{36}Ar. Glass degraders of thicknesses 2.02 and 5.03 mm were paired and installed in the degrader ladder. The detector stack (silicon telescope) was positioned on axis in the gas cell, with the first silicon detector 45.0(2) cm distant from the beryllium window. The number of primary ions detected was deduced from integrating spectra. Measurements were made for varying degrader angles, gas pressures and detector distances.

Shown in Figure 2.7 are raw on-line data with several spectra depicting the response from the first silicon detector in a series of measurements for ^{36}Ar primary beam The only change from one spectrum to the next is the angle (and, therefore, the thickness) of the degrader glass. The response of the first detector shows a predictable trend as more energy is removed upstream by the degraders, leaving successively fewer ions, with a greater range distribution, to be detected.

Stopping Profile

The *transmitted fraction* can be defined as the normalized fraction of primary beam ions that were counted in the first silicon detector. Now the measurements made for a fixed detector distance and helium gas pressure could be summarized in a simple graph of degrader glass angle versus transmitted fraction.

In Figure 2.8, the number of ions observed in the first detector begins to descend steeply as the amount of energy attenuated by the glass degraders enters a range

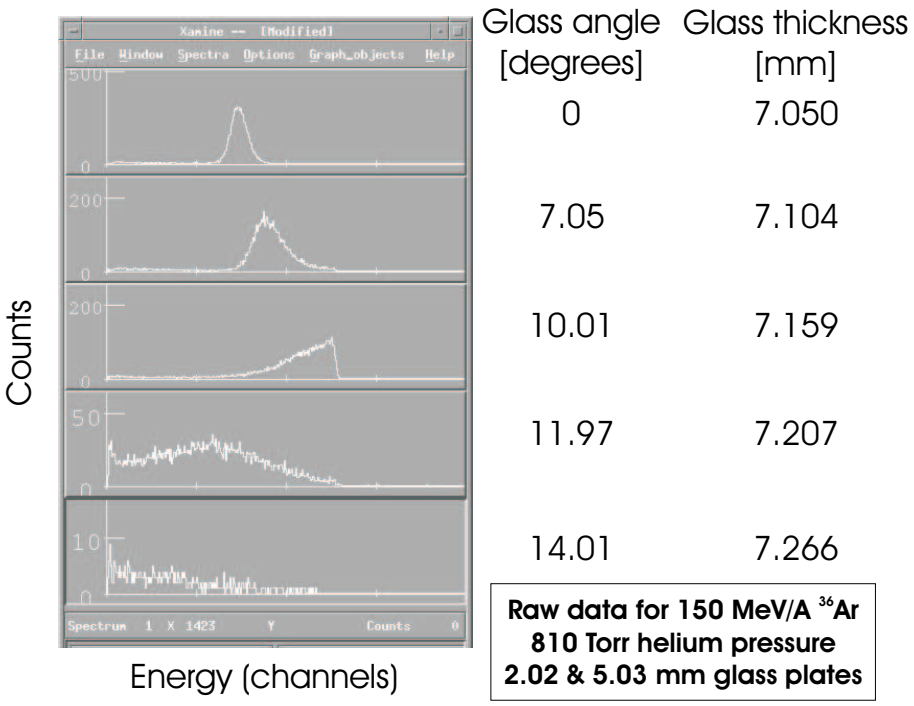

Figure 2.7: Raw data from first silicon detector (ΔE) over a range of glass degrader angles. Data is from the stopping of 150 MeV/A ^{36}Ar in 810 Torr (1.08 bar) helium with 2.02 and 5.03 mm glass plate degraders.

where ions can stop in the gas. At the largest angles, too much energy is removed by the glass degraders and the ions are stopped in the beryllium window.

Note that ions with total energy less than approximately 3 MeV were not counted as they fell below the threshold of the first silicon detector. SRIM calculations showed that, for example, the range of such ^{36}Ar ions would be less than 2 cm in the 1 bar helium. Therefore, in the case of the detectors at 45 cm distance in the 50 cm gas cell, the ions would have stopped in the gas cell. The number of ions under the threshold energy were calculated and corrected by using the calculated energy spectra (see Figure 2.9).

The correction is significant only at large degrader angles where the transmitted fraction is small. Therefore, the correction minimally affects the transmission curve.

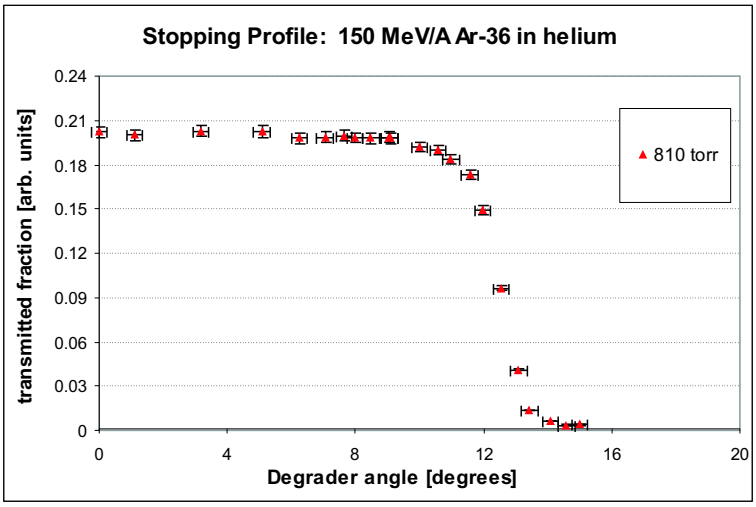

Figure 2.8: Stopping profile of 150 MeV/A ^{36}Ar ions in 810 Torr (1.08 bar) helium.

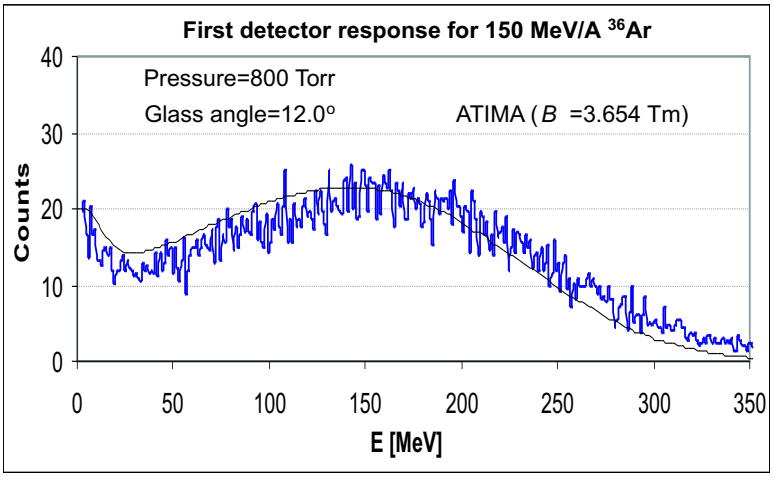

Figure 2.9: Energy spectrum with fitted ATIMA curve for 150 MeV/A ^{40}Ar ions in 800 Torr (1.07 bar) helium for a fixed degrader angle. The Bρ is the adjusted magnetic rigidity value used in the ATIMA calculation.

Pressure Variation and Primary Beam Calculations

Depicted in Figure 2.10 are stopping profiles with a fixed detector distance for the evacuated gas cell and for 800 Torr (1.07 bar) and 1200 Torr (1.60 bar) helium pressures. The data were fitted to a Fermi function of the form:

$$f(x) = \frac{1}{e^{(x-a)/b} + 1} \tag{2.5}$$

where x is the degrader thickness, a is the midpoint of the descending curve and b is indicative of the slope. The difference between the stopping profile for a given pressure and the stopping profile for the evacuated gas cell gives a direct measure of the fraction of the ions stopping in the gas as a function of degrader thickness [This simple change of x-axis units provides a linear representation of the degrader materials.]. This difference is represented by the two peaked curves of the figure. One can see that, at the optimal degrader thickness, approximately 60% of the ions stop in the 1.07 bar helium while 80% stop in the 1.60 bar pressure. Vertical error bars represent the combined statistical uncertainty in the A1900's plastic scintillator, the first silicon detector and the error on the low-threshold correction (using a conservative 50% for this particular correction). Horizontal error bars represent the combined uncertainties in determining the glass degrader angle and measuring the thickness of the glass.

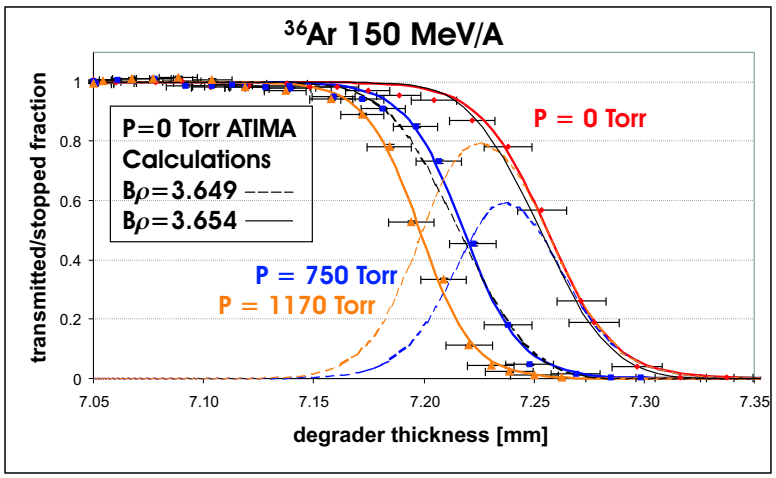

Figure 2.10: Transmitted (solid colored lines) and stopped fraction (dashed colored lines) of 150 MeV/A ^{36}Ar under three helium pressures fitted with Fermi functions. Also shown (in black) are the ATIMA calculations (for 0 Torr) with the experimental Bρ and the adjusted Bρ.

Also depicted in Figure 2.10 are curves determined by calculation. Data were compared with well-known stopping power calculations based on three different energy loss models (Hubert, Ziegler and ATIMA) [35, 37, 38] as incorporated into LISE. We found that the calculations using all of the nominal parameters did not agree well with the data (shown for an ATIMA calculation in Figure 2.10 above in dashed

lines). Very good agreement for the ATIMA calculation (solid lines in Figure 2.10) was obtained after a small adjustment in Bρ of 0.14%. The adjustments for the Hubert and Ziegler calculations were 0.20% and 0.24%, respectively, each producing similarly good agreement. Therefore, the ATIMA calculation was selected as the most closely matched model and was used for the remaining calculations. At this point, the A1900 had been calibrated by a time-of-flight method to provide a 5×10^{-4} level of uncertainty, and so the fields which figure into the magnetic rigidities are taken from Hall probes in the magnets [44]. Our adjustments (0.14%, for example) are slightly higher than the uncertainty.

Longitudinal Profiles

To this point, data has been presented which showed variations in degrader thickness and gas cell helium pressure. To make our understanding of stopping in the gas cell more complete, we examined the remaining untested dimension–the longitudinal stopping profile along the axis of the gas cell. Shown below in Figure 2.11, is a raw transmitted fraction versus the distance of the first silicon detector from the beryllium window. Comparing the data in the upper panel shows the expected trend on the transmitted fraction when the gas pressure is varied.

Note that possible undercounting may occur if the lateral spread of the beam was larger than the silicon detector (300 mm^2 area $\approx$ 19 mm diameter). In the case of the fixed detector distance, we were concerned that the divergence (or straggling) perpendicular to the beam's path through the gas might be larger than detector size. SRIM calculations before experiments showed the lateral straggling in the gas to be negligible, discounting that possibility. In the case of the detector being moved along the beam axis (the longitudinal profile), we had concerns with the optical divergence of the beam; that is, the beam's path after the last quadrupole doublet magnet might not be parallel in the gas cell. Measurements proved this divergence indeed had a real effect. With the gas cell evacuated of gas, the counting rate was not constant

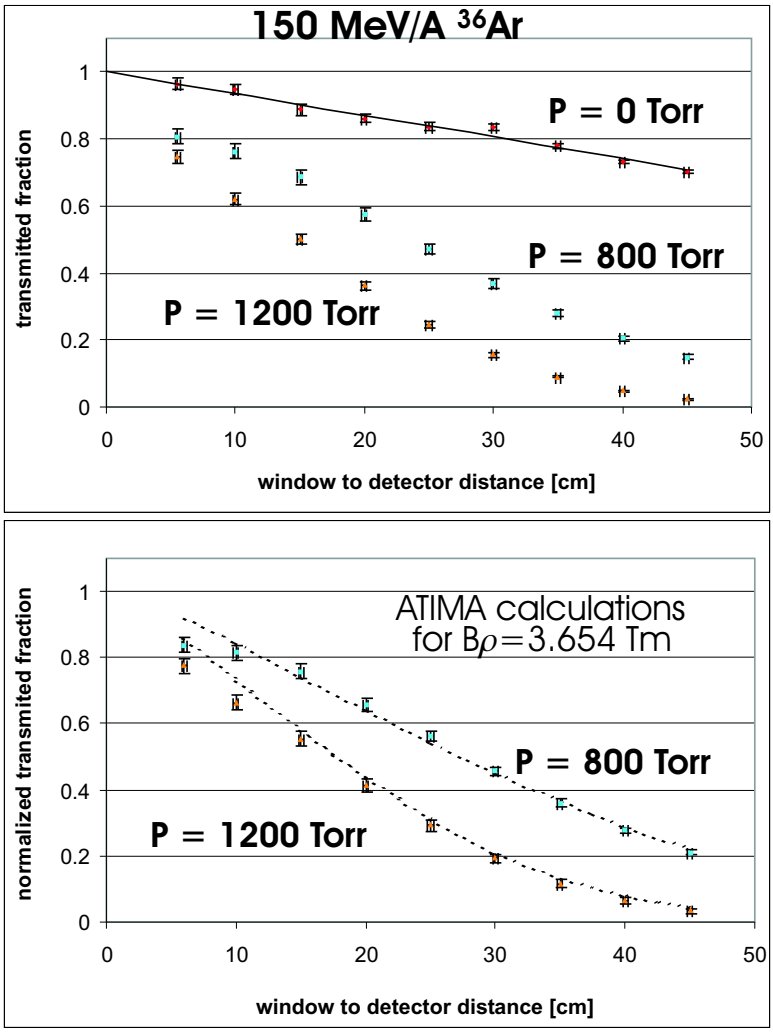

Figure 2.11: Longitudinal profiles for stopping of 150 MeV/A ^{36}Ar. The upper panel shows the raw transmitted fractions. The lower panel shows data normalized to the profile of the evacuated gas cell and ATIMA calculations for the adjusted Bρ.

when the detector distance was varied (see Figure 2.11). The data given in the lower half of that figure have been normalized to the profile of the evacuated cell. Now the calculations with an adjusted magnetic rigidity are able to reproduce the normalized data. With this information in hand, however, the beam divergence is not expected to be a detriment to the stopping and future extraction of ions where the divergence is much less than the extraction electrode's inner diameter (on the order of 5 cm).

Other Primary Beam Measurements

A summary of measurements made on other primary beams is given below. This summary includes discussion of the trends observed in measuring various nuclides of different energies.

Stopping profiles were measured for several beams. To maintain beam schedule flexibility, gas stopping trials were ad hoc in that measurements were made when a primary beam happened to be on the NSCL's running schedule. With this constraint

Table 2.4: Summary of primary beam experiments.

Beam	Nominal Energy [MeV/A]	Bρ [T·m]	Correction to Bρ [%]
^{36}Ar	150	3.649	0.14
^{36}Ar	150	3.673	0.11
^{36}Ar	125	3.311	0.24
^{40}Ar	100	3.284	0.06
^{48}Ca	110	3.714	0.25
^{76}Ge	130	3.960	1.09
^{86}Kr	140	3.342	-1.45
^{136}Xe	120	3.972	-2.27

on beams and energies (see Table 2.4), our intent was to cover the widest possible range of nuclide masses and beam energies in order to demonstrate the flexibility of the gas stopping system.

In addition to the beam's Bρ, Table 2.4 lists the Bρ correction required to have the ATIMA calculation agree with the experiment. The adjustments necessary for lighter beams (Z$\leq$20) were all much less than 1%, making for accurate stopping predictions. The heavier nuclides required a wider range ($\pm$2%) of corrections.

It can be observed in several of the stopping profiles that the flat, upper part of the profile can sometimes dip prematurely (Figure 2.12) or rise before the descending part of the curve. We believe this is controlled by the last quadrupole before the gas cell. After the beam passes through the glass degraders, the attenuated ions have a greatly reduced Bρ (Bρ_6, as it is the sixth and last section of the beamline before

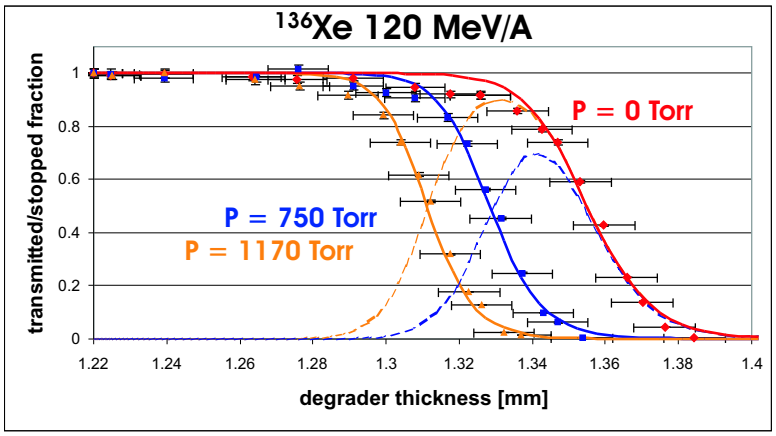

Figure 2.12: Transmitted (solid line) and stopped fraction (dashed line) of 120 MeV/A ^{136}Xe under three helium pressures.

entering the gas cell). In early experiments, this magnetic rigidity in the last beamline section was not carefully set, resulting in a non-ideal (straight, parallel) beam entering the gas cell.

Although the stopping power was underestimated by ATIMA in the case of the heavier beam, the general shape and appearance of the stopping curve is very similar to those of the lighter beams. The only true concern raised by this discrepancy is the need to have a versatile primary degrading system (covering a wide range of glass thicknesses) to account for the underestimated stopping power when using heavier beams.

2.3.3 Conclusions for Primary Beam Measurements

The results of our several measurements on primary beams indicate a functional gas stopping system operating with good stopping efficiency. In addition, predictions of energy loss calculations seem to largely agree with our findings.

The major items of equipment to perform gas stopping of primary beams are functioning as required. The variable degraders are performing as expected, although we have seen a need to have a greater variety of glass thicknesses. The beryllium window seems robust and appears to be acceptable. In order to prepare for ion extraction

tests, ring electrodes were introduced into the gas cell (more discussion of extraction will take place in Chapter 4). At this point, the detector stack was no longer compatible and a single silicon detector was installed between electrode rings. This lone detector could be moved in and out of the path of the beam; therefore, it was used for further stopping measurements, but would also serve well later while combination stopping/extraction experiments were performed.

The stopping efficiencies of primary beams was greater than 50% for most ions with a wide range of masses (A=36-126) and energies (100-150 MeV/A). This efficiency has been demonstrated in concert with the central apparatus in our system–the gas cell. That is, we believe we can perform efficient stopping of ions with our 50 cm gas cell at 1 bar helium pressure.

The comparison of our data with calculations and theory was rather good, with a minimum number of adjusted parameters. In our case, the thicknesses, densities and compositions of all degrader materials as well as the beam's momentum width were held constant (at their measured values) in the calculations. Only the magnetic rigidity was varied. For the lighter primary beams ($Z \leq 20$), the adjustment of $B\rho$ to find good agreement with calculations was quite small. Even in the heavier beams, the adjustment was within $\pm 2\%$.

The discrepancies between experiment and calculation listed for the 150 MeV/A ^{36}Ar which required adjustments to the magnetic rigidity for the three models (ATIMA: 0.14%, Hubert: 0.20% and Ziegler: 0.24%) are not completely unexpected. Model calculations have been shown to vary from experimental data by as much as 5% [37, 43]. However, the sign of the variation can vary over different energy regions; that is, the model uncertainties can have small overall corrections if the stopping power over a wide energy range is considered. For the ^{36}Ar data, the three corrections to $B\rho$ were all positive, indicating an overestimation of the energy losses.

With a stronger sense of the operation and performance of the gas stopping station on primary beams, we then turned our attention to the follow-on objective–a study

of the stopping of secondary beams.

2.4 Secondary (radioactive) Beam Measurements

Studying the stopping of secondary beams (that is, radioactive fragments) was one of the intermediate objectives of the gas cell project. Although the information gained while studying primary beams was useful, the final objective of the Gas Stopping Station (and LEBIT) is to stop and transport beams of rare, radioactive ions. Some of the same characteristics which make secondary beams ill-suited for precision experiments, also make them more difficult to efficiently stop. A significant energy spread, non-parallel beams and beam contamination are the forefront issues in dealing with secondary beams as compared to primary beams.

2.4.1 Range Compression

Our studies of primary beams typically saw the percentage of ions stopping in one bar of helium gas in the 50 - 70% range. As mentioned earlier, the primary beams typically had a momentum spread of $\Delta p/p \sim 0.07\%$. However the secondary beams produced at the NSCL have a much greater momentum spread (up to 5%). A quick calculation examining 100 MeV/A ^{40}Ar (Figure 2.13) reveals that the expected stopping fraction of ions having even a small momentum spread of 0.2% would be severely reduced. Notice that in the more ideal case of the primary beams (upper panel), even at the optimal degrader glass angle, the range distribution of ions stopping in the gas spans the entire length of the gas cell, including some beam that is lost; that is, even when we have the best stopping conditions, some of the beam hits the rear of the gas cell and some is stopped in the beryllium window. Now, as the momentum distribution is increased (lower panel), the situation is more severe. The stopping distribution is so wide that nearly 30% of the beam is lost to each the rear wall and the beryllium window, leaving just over 40% of the beam to stop in the gas. Also presented (in

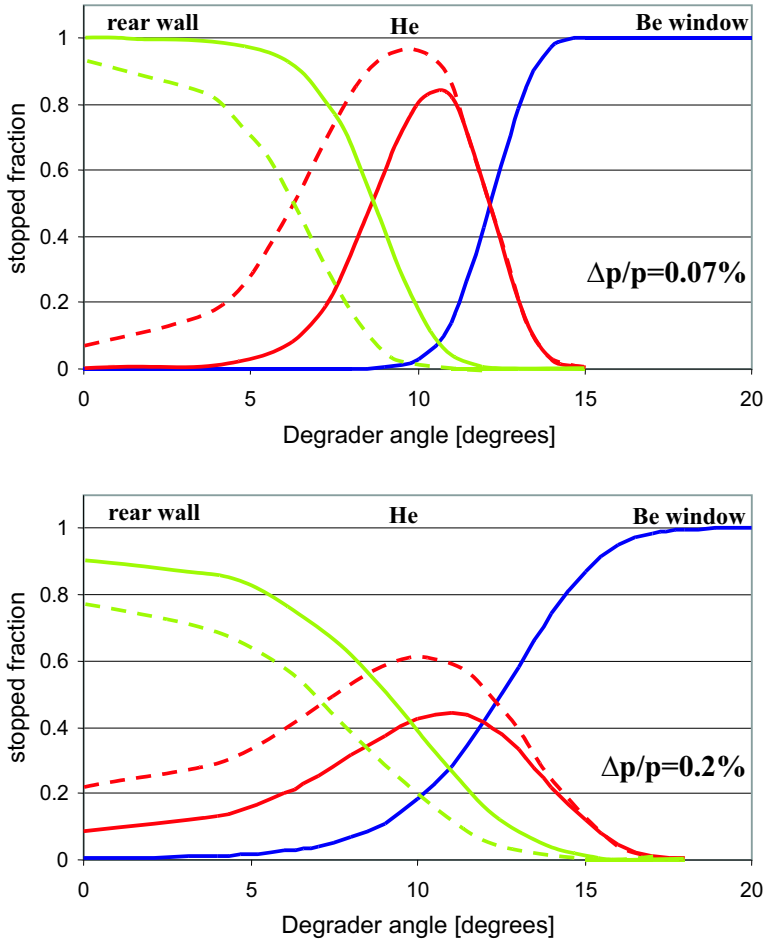

Figure 2.13: Comparison of calculated stopping fraction for two different beam momentum spreads (0.07% and 0.2%.) in stopping 100 MeV/A ^{40}Ar. The solid lines are calculated for 1 bar pressure while the dashed lines are for 1.5 bar.

dashed lines) is the predicted stopping one can expect by raising the helium gas pressure to 1.5 bar. In this situation, the fraction of ions one can stop in the gas has improved. However, as discussed further in chapter 3, the higher gas pressure has other drawbacks which may preclude its use.

This reduction of stopping capability would be unacceptable when dealing with most secondary ion beams, so a method to reduce the range of ion momenta was needed. The idea of **range compression** has been studied by Weick *et al.* at GSI [45,46]. They proposed that by placing a specially shaped mono-energetic degrader at the dispersive plane following a dispersive element, the momentum spread of reaction products could be reduced to the 0.2% level (Figure 2.14). Such a reduction would

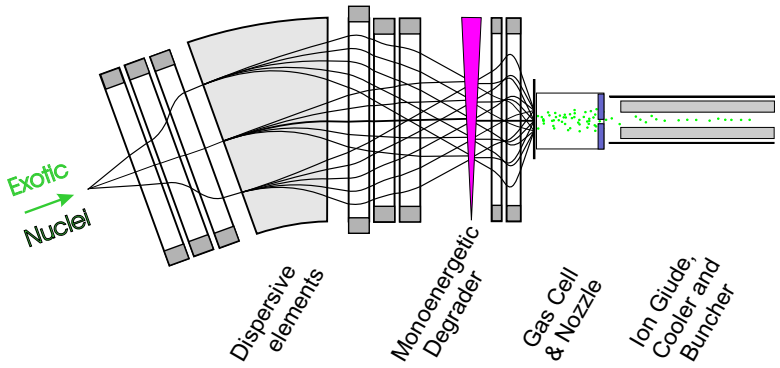

Figure 2.14: Range compression concept showing optical elements.

bring the momentum distribution into an acceptable range for collection in a gas cell of finite size.

Beam Impurities

Early in the discussion of secondary beam data we must assess the matter of beam contamination. As noted in the Introduction, one disadvantage of fragmentation beam production is beam impurities. Certainly impurities were produced and transmitted to the gas cell along with desired radioactive species. This fact begs an obvious question about data taking with these impure beams. Were the measured stopping profiles indeed representative of the specified ion or did some miscounting occur?

The use of the stack (telescope) of silicon detectors provided rates of reaction products, produced by interaction of the beam with degrader materials (glass and beryllium window). Reaction products, caused by fragmentation, were typically a few percent of the primary beam. The contribution of detector counts by reaction products was corrected in all data presented.

Beam purities were deduced from particle identification spectra taken at the focal plane of the A1900 and are summarized in Table 2.5.

The separation of counts contributed by beam impurities was easily taken into account by considering the different stopping powers of the ion impurities. This process is most clearly illuminated in the following diagram (Figure 2.15).

Table 2.5: Secondary beam impurities.

Primary beam	Secondary beam	Impurities
^{36}Ar	^{32}P 96.2%	^{33}S 3.4%, ^{31}Si 0.3%
^{86}Kr	^{80}As 79.7%	^{81}Se 21.3%, ^{79}Ge ~0.1%
^{40}Ca	^{38}Ca 56.8%	^{37}K 34.1%, ^{36}Ar 9.1%

While a clear separation of the impurities is not evident in the typical ΔE - E spectra (Figure 2.15a), a plot of ΔE - TOF (Figure 2.15b) provides a clear separation of the different nuclides. Examining any one of the curves in Figure 2.15b, one can follow (from right to left) the ions as they first leave only a fraction of their energy in the silicon detector (ΔE) rise as their energy is attenuated more by the glass degraders. Then as the amount of energy degrading reaches a critical value, the amount of energy deposited in the first detector drops as the ions are giving up their remaining energy (total energy) to the silicon.

2.4.2 Equipment for Secondary Beam Measurements

One device was employed to reduce the momentum spread of secondary beams. Momentum slits in the dispersive plane of the A1900 Fragment Separator can be adjusted to physically block the outlying beam thereby reducing the *momentum acceptance* of the separator. While the full momentum acceptance of the A1900 is 5%, the experimenter can close the slits to reduce the momentum spread of the beam to 0.1%.

In order to test the proposal of Weick *et al.* (Figure 2.14), the beam line connecting the A1900 to the gas cell in the N4 vault was tuned to provide a dispersive focus in the horizontal plane at a position just downstream of the glass degraders [47]. This tune allowed us to insert a mono-energetic wedge in the path of the secondary beam in addition to the glass degraders (Figure 2.16). The wedge was installed on a drive which could be remotely controlled.

The dispersion was measured with a ^{40}Ar primary beam by inserting thin degrader foils at the A1900 target position. The energy loss and resulting Bρ were calculated

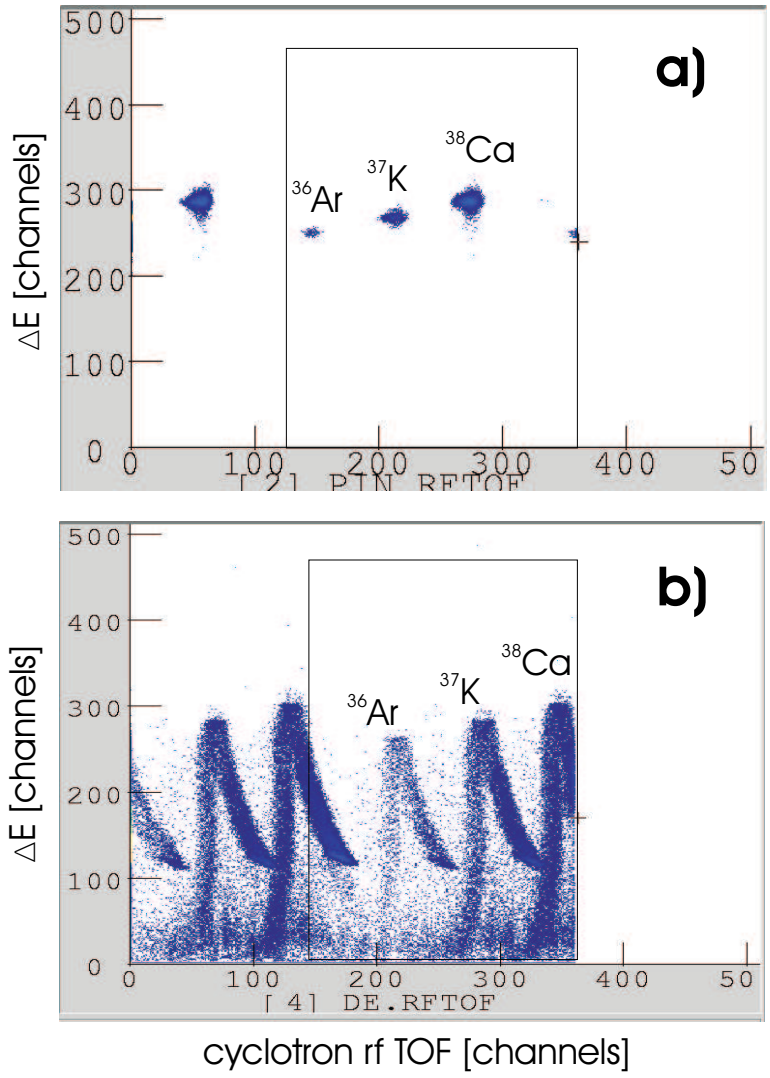

Figure 2.15: Particle identification in secondary beams. Data is aggregate of several experimental runs (for different glass degrader angles) for the fragments of 140 MeV/A ^{40}Ca primary beam. Shown in Panel a) is PIN ΔE vs. TOF. Shown in Panel b) is the first Si detector ΔE vs. TOF.

with LISE. The position of the beam at the mono-energetic wedge position was observed with a scintillator using a video camera. The results are shown in Table 2.6 and Figure 2.17.

The dispersion was determined to be 0.92 cm/%, in very good agreement with the expected value of 1 cm/%

With the onset of measuring secondary beams, we had several thin, aluminum (type 2024) wedge-shaped degraders machined by an EDM (electric discharge ma-

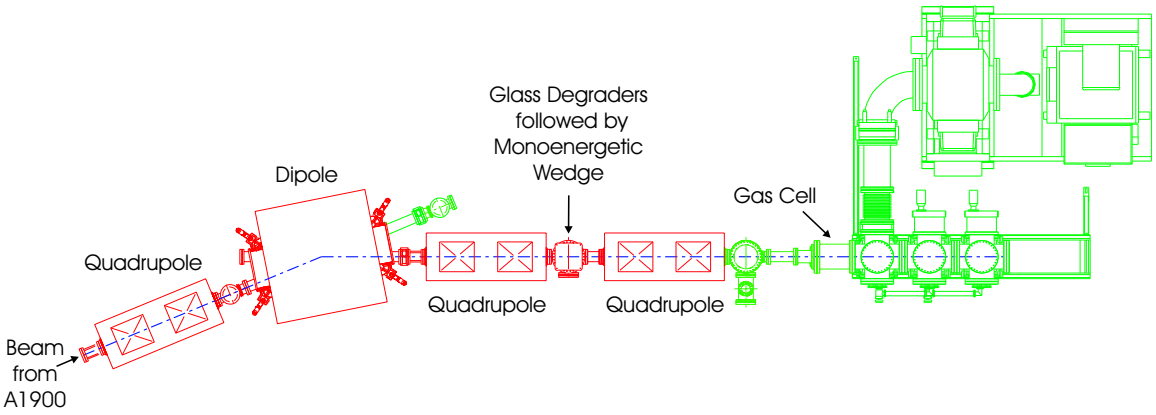

Figure 2.16: Beamline upstream of the Gas Stopping Station showing optical elements performing range compression.

Table 2.6: Dispersion measurement data using aluminum foils with nominal 130 MeV/A ^{36}Ar beam (Bρ=3.382).

Foil thickness [mg/cm^2]	ΔE [MeV/A]	ΔBρ [%]	Beam position [mm]	Dispersion [mm/%]
78	2.58	1.39	13.3	9.57
65	2.15	1.16	10.4	9.04
52	1.71	0.92	8.5	9.23
39	1.28	0.69	6.7	9.71
26	0.85	0.46	4.4	9.57
13	0.42	0.23	2.2	9.57

chining) technique. These approximately 2.5 $\times$ 5 cm degraders were wedged in the horizontal direction (normal to the beam axis). The average thickness and angle on a wedge was usually a compromise for each specific beam and energy between thinness and ability to be precisely manufactured. The parameters of the wedges are included in the secondary beam summary (Table 2.7, in the following subsection).

The measured profiles and wedge's effect on the gas stopping measurements is outlined in the next subsection.

2.4.3 Secondary Beam Stopping Data

Our campaign of measuring secondary beams began on 03 January 2003. Whenever time allowed, both the primary beam and its secondary fragment were measured.

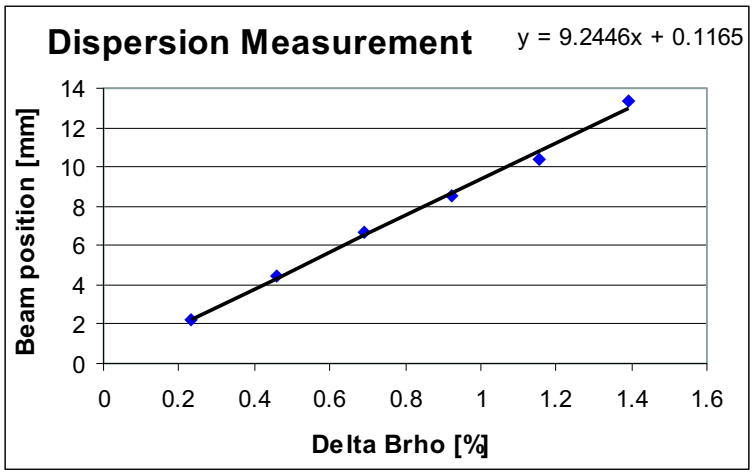

Figure 2.17: Results of dispersion measurements.

Table 2.7: Summary of secondary (radioactive) beam experiments.

Date (Year = 2003)	Primary Beam, Energy [MeV/A]	Secondary Beam, Energy [MeV/A]	Wedge Parameters: middle thickness, angle [mm], [mrad]
03, 27Jan	^{36}Ar, 150	^{32}P, 111	2.28, 10.8
10, 27Mar, 17Apr	^{86}Kr, 140	^{80}As, 93.6	0.736, 2.42
15May	^{40}Ca, 140	^{38}Ca, 91.9	0.736, 2.42
			0.975, 11.2

Before the data is presented, we remark on the units used in the presentation of the data. In the instance of secondary beams, we have an aluminum wedge degrader in addition to the glass of the variable degraders. Now, using a collection of degrader materials, using only the units of glass degrader thickness on the x-axis of the stopping profiles is inappropriate. Instead, we will need a more all-encompassing unit. If we recall the Bethe specific energy loss formula (section 2.1), a more feasible unit can be readily developed:

$$-\frac{\mathrm{dE}}{\mathrm{dx}} = \frac{4\pi \mathrm{e}^4 \mathrm{q}^2}{\mathrm{m_0 v}^2} \mathrm{NZB} \tag{2.6}$$

Focusing on the terms contributed by the absorber (degrader), the product of N [atoms/volume] and Z [electrons/atom] gives an electron density [e^-/volume]. Multiplying an electron density [e^-/cm^3] by a real thickness [cm] would give an "electron aerial density" [e^-/cm^2] much like the mass aerial density [mg/cm^2] described ear-

lier. This new quantity, electron aerial density, like mass thickness, factors out the absorber density, but goes one step further in factoring out the effective atomic number (or electron number) of the absorbing material. In our case where we have more than one degrader material (glass and an aluminum mono-energetic wedge) each being a composite of many different atoms, the electron thickness comparison becomes a single absorber parameter which can equitably treat any combination of degrader material compositions and thicknesses..

The parameters describing the measured secondary beams are summarized in Table 2.8. $B\rho_0$ is the magnetic rigidity of the primary beam from the K1200 cyclotron, $B\rho_{1,2}$ is for the section of the A1900 immediately following the production target, and $B\rho_{3,4}$ is the rigidity value of the ions after the aluminum wedge and count rate scintillator at Image 2 of the A1900. From these parameters, one can recreate our experimental conditions in programs such as LISE.

Table 2.8: Secondary beam parameters. Note: a 28 mg/cm^2 scintillator was used at the same position as the wedge (not included in the wedge thickness shown here).

Primary Beam	$B\rho_0$	Be Target thickness [mg/cm^2]	$B\rho_{1,2}$	Al Wedge thickness [mg/cm^2]	$B\rho_{3,4}$	Fragment
^{36}Ar	3.670	658	3.512	300	3.321	^{32}P
^{86}Kr	4.499	285	3.923	300	3.461	^{80}As
^{40}Ca	3.718	564	2.973	300	2.689	^{38}Ca

The secondary beam data is presented below in blocks which intend to highlight the usefulness of the methods of reducing the secondary beam momentum spread.

Use of Momentum Slits

Both Image 2 and Image 3 of the A1900 have slits which can be placed in the beam's path to physically limit the momentum spread of the beam. By varying the slits at Image 3, data was taken for 0.3, 1.0 and 2.0% momentum spreads. An example of the effect of changing the momentum slits on the gas stopping profile is shown in Figure 2.18.

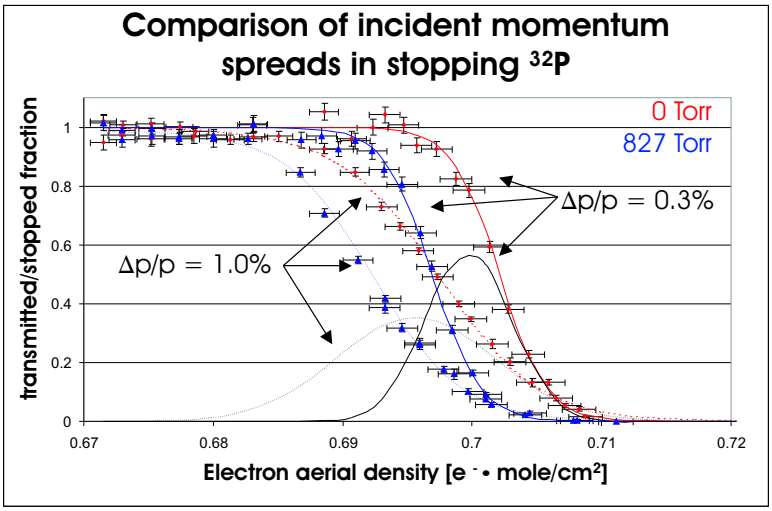

Figure 2.18: Comparison of the stopping fraction for ^{32}P for incident momentum spreads of 0.3% and 1.0%.

Evident in Figure 2.18 is the improvement in the stopping fraction (difference between gas and no gas curves). The stopping profile becomes steeper as the slits are narrowed. At an incident momentum spread of 1.0% only 35% of the beam is stopped, while at 0.3% momentum spread, 55% of the beam can be stopped.

The Mono-energetic Wedge

Next the mono-energetic wedge, or M wedge, was paired with the proper glass degrader thickness and stopping profiles were measured. An example of data taken with the M wedge, where the beam's momentum spread incident on the glass and wedge is 2.0%, is shown in Figure 2.19. Using the M wedge, again the fraction stopped in the gas increases, proving the wedge's ability to compress the ranges of the secondary beam ions.

A homogeneous wedge, or H wedge, was also inserted into the beam path. This wedge has the uniform thickness as the middle thickness of the M wedge; that is, the H wedge is, more precisely, a flat degrader. It was quickly apparent that the mono-energetic wedge had the desired energy bunching effect. This could qualitatively be seen by simply comparing the energy spectra for the M wedge and H wedge produced

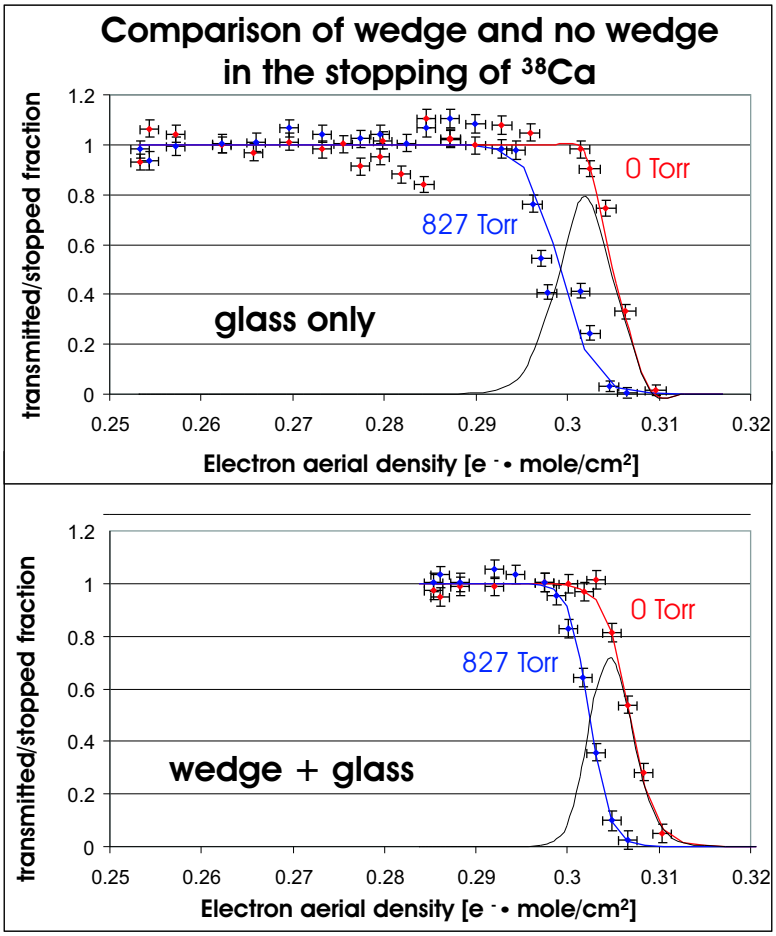

Figure 2.19: Range compression demonstrated by comparison of using a mono-energetic wedge and glass only in the stopping of ^{38}Ca. The momentum spread of the beam incident on the degrader glass is 2.0%.

under similar conditions (see Figure 2.20). Now if we examine the stopping profiles obtained with the two wedges (Figure 2.21), the M wedge clearly has more of an effect on the stopping fraction–giving additional credence to the concept of range compression using a mono-energetic wedge. The M wedge's stopped fraction is nearly twice the fraction of beam stopped using the H wedge.

2.4.4 Conclusions for Secondary Beam Measurements

The results of our experiments on secondary beams furthered our understanding of stopping fast beams. It was shown that stopping efficiencies could be improved with the use of equipment to shrink the momentum spread of the secondary beams. The

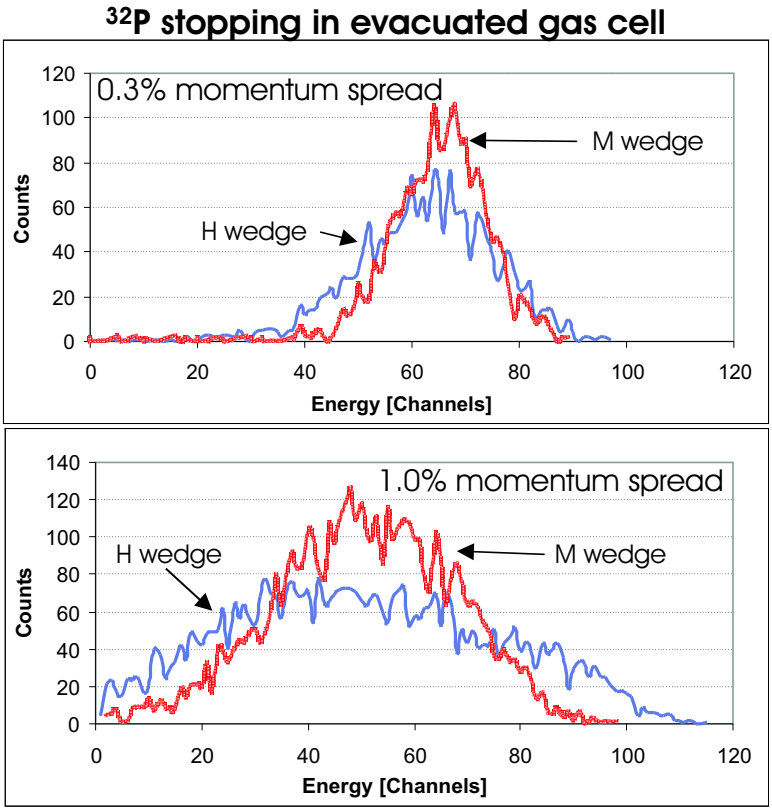

Figure 2.20: Energy spectra in the 1.5 mm Si detector for the M and H wedges with 0.3% and 1% momentum distributions. A zero degree glass angle was used for the H wedge spectra while a glass angle of ~10 degrees was used to take the M wedge spectra to account for the slightly different thicknesses of the wedges.

use of slits in the A1900 Fragment Separator to reduce to beam's incident momentum spread provides a definite improvement on the fraction of ions stopped in the gas cell (Figure 2.18). In addition, the mono-energetic wedge was shown to indeed compress the range (and stopping distribution) of the secondary ions resulting in an improved stopping fraction when compared to glass degraders alone (Figure 2.19) and compared to using an aluminum wedge of constant thickness (Figure 2.21).

Improvements to stopping secondary beams have relevance to calculations. Comparison of data to calculations is complicated by uncertainties in the beam optics. Two sources are likely contributing to shifts in the stopping profiles. One source occurs well upstream of the gas cell in the A1900–uncertainty in positioning the momentum slits in conjunction with the beam. In addition, downstream near the gas cell, positioning

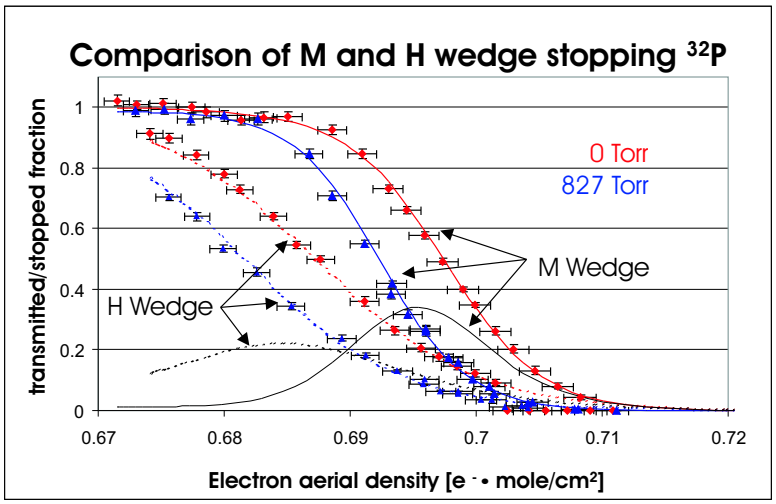

Figure 2.21: Comparison of mono-energetic and homogeneous degraders in the stopping of ^{32}P. The curves at the bottom of the graph (stopping fractions) demonstrate the mono-energetic wedge's compression of the range distribution.

of the beam in the center of the mono-energetic wedge also included uncertainty.

Impurities in the beams are manageable (Figure 2.15). We have a method in place to account for contaminants in the beam when figuring gas stopping efficiencies. The undesired contaminant ions will largely be removed by mass selection of the RFQ ion guide (Appendix A) and the remainder of the LEBIT beam transport.

A summary of the stopping efficiencies for secondary beams will be included in the next section.

2.5 Gas Stopping: Summary and Conclusions

The equipment designed and constructed for our gas stopping efforts is functional and, save for minor improvements, will be capable of performing gas stopping for the wide variety of beams produced at the Coupled Cyclotron Facility.

We have shown the ability to stop both stable and radioactive beams over a wide range of masses and beam energies (summarized in Table 2.9). These efficiencies look promising; that is, the demonstrated stopping fractions will support the overall scheme of LEBIT by stopping a high percentage of radioactive beams.

Table 2.9: Summary of gas stopping experiments.

	Primary beams	Secondary beams
Mass range [A]	36-126	32-80
Energy range [MeV/A]	100-150	92-111
Efficiency range [%]	50-90	35-80

Remembering that the gas stopping is an intermediate objective on the way to providing low-energy radioactive beams, perhaps the most significant result of the gas-stopping tests is the determination of the glass degrader angle which maximizes the stopped fraction of ions. For example, the in the stopping of ^{38}Ca (Figure 2.19), the value along the x-axis corresponding to the maximum stopping fraction can be translated to a degrader glass angle (approximately 24 degrees). This value will be important in maximizing our overall efficiency (discussed further in Chapter 4).

Chapter 3

Gas Flow

3.1 Concept

The NSCL's Gas Stopping Station will function as a high-pressure radioactive ion source in order to provide low energy beams for precision experiments. The previous chapter (Gas Stopping) described the process of bringing the fast radioactive ions to rest in the Gas Cell. These ions must then be quickly and efficiently extracted from the gas cell through an orifice and into an expansion chamber. This chapter will be devoted to discussion of the gas flow aspect of the extraction process and the components of the system involved with gas flow.

3.2 Design Considerations

Gas flow, and the orifice through which the ions would be extracted from the gas cell was actually the earliest and most central of considerations for the gas stopping system. Although the overall concept for a gas cell is somewhat new, the stopping of ions in a gas-filled chamber and the later guiding of ions through a low pressure gas are generally well understood. However, the means to perform fast and efficient extraction of ions with gas flow through an orifice is less well understood and further complicated

if the gas stopping chamber is of large dimensions and filled with (possibly) a high pressure gas.

3.2.1 Choosing a Gas

Radioactive ions stopped in a gas can be extracted and largely separated from the stopping medium. In constructing such an ion source, the first issue then becomes which gas to use. The choice of stopping gas figures greatly into the design and capabilities of a gas-stopping ion source.

The selection of helium as the stopping medium was arrived at quickly. Although low mass (A=4) helium has the disadvantage of lower stopping power due to low electron density, several other properties make it quite useful, almost essential, for the stopping of fast radioactive beams.

1. Noble gas chemistry. Helium will have few to no chemical reactions with ions under study–no compounds are formed. Argon, with its greater stopping power could also be used, but it is significantly more polarizable than helium and would lead to adduct formation [48].

2. Availability and cost. Helium is widely available in the United States. It is found with natural gas deposits. Only the noble gas argon is cheaper. Local prices for Grade-A gases (99.999% purity) are typically $60 for 336 scf argon or 291 scf helium (scf=standard cubic feet: 9514 standard liters and 8240 standard liters, respectively).

3. First ionization potential. Helium has the highest first ionization potential of any element, 24.6 eV. In light of this fact, the gas cell should retain any ions stopped in the helium at a charge state of 1^+.

4. Low mass. Helium's low mass is very different from ions that will be studied, an advantage during ion transport. After extraction from the gas cell, the radioactive ions will undergo several meters of beam transport during which the experimenter can apply mass selection. Even if helium could be ionized, its charge/mass ratio would very different from the ions under study.

Helium's high first ionization potential is the most crucial property when it comes to efficient gas stopping and extraction. The desired charge state of 1^+ for the ions under study is necessary for efficient transport. Ions at a higher charge state will rarely survive the subsequent ion-guiding process. Although helium's ionization potential is best suited for maintaining ions at a 1^+ charge state, the possibility for 2^+ charge states exists. That is, elements exist which have a second ionization potential that is lower than 24.6 eV as well:

Table 3.1: 1st and 2nd Ionization Potentials of some sample elements [49].

Element	1st IP [eV]	2nd IP [eV]
helium	24.6	54.4
carbon	11.3	24.4
silicon	8.2	16.3
germanium	7.9	15.9
tin	7.3	14.6
neodymium	5.5	10.7

Evident is the general trend of decreasing 2nd ionization potentials with increasing atomic number. In addition, there is a chance for ions to remain triply ionized, 3^+. This is generally only true of the rare earths, including neodymium, Nd, listed above (3rd ionization potential 22.1 eV).

3.2.2 Stopping Gas Purity

Again, examining the first ionization potentials, there are many compounds possibly present in the gas cell and its vacuum systems which could act as scavengers:

Table 3.2: 1st Ionization Potentials of some common compounds [49].

Compound	1st IP [eV]
water	12.6
nitrogen gas	15.6
oxygen gas	12.1
pump oils	~8-11

These undesired compounds, with relatively low first ionization potentials, could

reduce the efficiency of the gas stopping process by neutralizing radioactive ions. Therefore, it is important to limit the number of ions neutralized by the impurities in the stopping gas as we are interested in studying rare radioactive beams which are produced at low rates (as low as a few per second).

Cleanliness of components and purity of the stopping gas will contribute to a good efficiency. All components of the gas cell and its vacuum system were cleaned before installation and later handled with latex gloves. As to the purity of the gas, special effort and extreme care were given to the selection and handling of components which make up the gas handling system, detailed in the next sub-section.

3.2.3 The Gas Handling System

To deliver helium for stopping, a gas manifold was designed (Figure 3.1). Its function is to deliver the ultra-pure helium, providing a constant pressure of helium in the gas cell. The inner surface of all its 1/4 inch tubing is electropolished. In addition, the

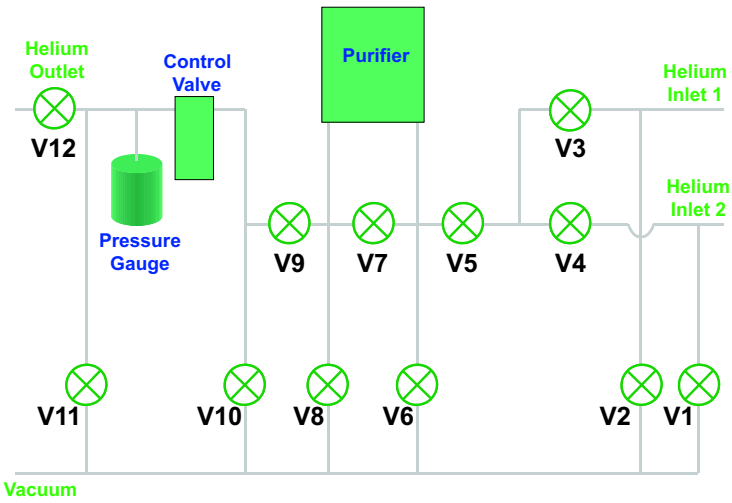

Figure 3.1: Schematic of the gas handling system that delivers ultra-pure helium to the gas cell.

valve bodies and stems are electropolished. All the valve-to-tube connections are of the VCR metal seal type. Great care was taken in its assembly in a clean hood to maintain the absolutely lowest possible level of contamination.

The gas manifold chiefly has two modes of operation: helium delivery and baking.

Helium Delivery

The helium delivery mode uses the upper set of valves shown in Figure 3.1. In this mode, the manifold delivers the ultra-pure helium required for efficient stopping of the ions. Grade-A, 99.999% purity, or better helium is introduced into the manifold (at Helium Inlet 1 or 2) where it passes through a Nanochem L-2000 purifier. This purifier uses a proprietary resin in solid black bead form, OMX, which contains lithium hydride and organolithium polymer. The purity level specified by the manufacturer for He is <1 ppb each: H_2O, O_2, CO and CO_2. The purifier can operate at a flow rate up to 50 slpm N_2. Our operating conditions require ~5 standard liters per minute (slpm) He (2 slpm N_2).

The delivery of this now ultra-pure helium to the gas stopping cell is regulated by a MKS Type 205E Pressure/Flow Controller. The controller uses feedback from a pressure gauge (MKS Baratron Type 121A Absolute Pressure Transducer) located near the outlet of the manifold in conjunction with a precision valve (MKS Type 148J Pressure and Flow Control Valve) to maintain the pressure of helium being delivered to the gas cell.

Baking

The baking mode largely uses the lower set of valves (shown in Figure 3.1) and the attached pump system. The vacuum is provided by a Varian Minuteman Turbopump system. A 70 liter per second turbopump is backed by a diaphragm pump in this dry (oil-free) system.

The manifold and delivery tubing is lined with resistive heating elements for baking. When activated, the heating elements cause contaminants to desorb from the manifold and gas delivery tubing, while the vacuum system evacuates these contaminants.

3.3 The Gas Jet

3.3.1 Introduction and Background

Although the fundamentals of stopping ions in a gas are understood, the extraction of these ions from a high pressure gas cell would require considerable attention. It was clear that the ions would be passed from the stopping region of high pressure (stagnation pressure) gas into a region of lower pressure through an orifice. The use of electric fields to maneuver the ions through the gas-stopping cell to the immediate region of the orifice will be discussed in the next chapter. The remainder of this chapter will be devoted to the characterization of the helium gas flow as it carries ions through the orifice and expands as a free jet into the region of lower pressure.

3.3.2 Gas Jet Properties

The distribution of the helium gas after the orifice must be known for modeling the capture and transport of the ions by the ion guide. Practical constraints from hardware placed an upper limit on the length of the gas cell at $\sim$100 centimeters (not so important to the jet, but more a gas cell pressure versus gas cell length consideration). In addition, the length in the first lower pressure expansion chamber was limited to approximately 50 centimeters.

As a result, an accurate description of the free jet was necessary to complete the design of the gas cell-expansion chamber combination (including a skimmer) and to optimize our ability to stop and extract short-lived radioactive ions. The gas cell pressure would ideally be high to aid stopping, but the pressure must be low enough such that (1) the expanding gas jet length is confined to the length of the expansion chamber and does not interact with the skimmer that follows and (2) the gas pressure does not prevent prompt extraction of ions from the gas cell.

The orifice should be of a shape such that transverse expansion of the jet is minimized and of a size that allows for a reasonable background pressure in the

expansion chamber (given the available pumping speed).

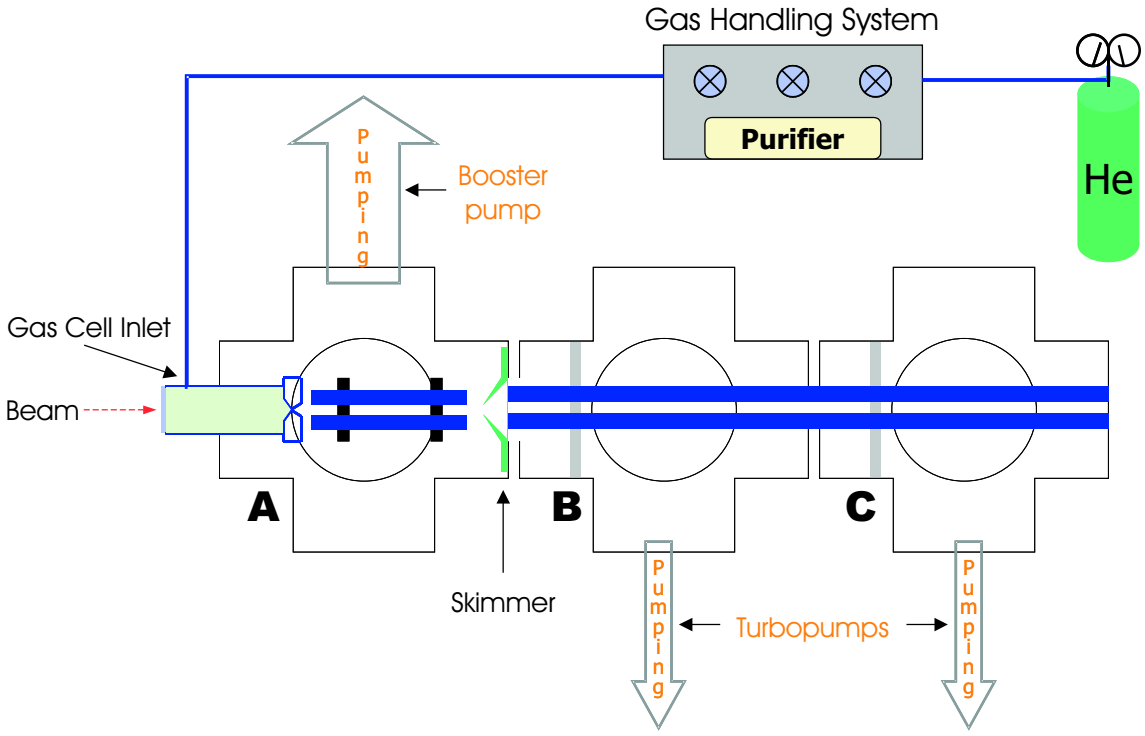

Figure 3.2: Schematic of the gas handling system, the gas cell and the differentially pumped chambers of the Gas Stopping Station.

The typical throughput for the orifice is approximately 10 Watts. [The throughput, Q, is the conductance, C (m^3/s), times the pressure difference, ΔP, (N/m^2).] The differential pumping is accomplished by Varian vacuum equipment (see Figure 3.2 and Table 3.3).

Table 3.3: Gas stopping pumps and speeds. All pumps are manufactured by Varian.

Pump	Type	Model	Pumping Speed
Booster	Roots Blower	VB-5400	2550 L/s, 5400 cfm
Backing (Booster)	Mechanical Piston	KT-1350	368 L/s, 779 cfm
Turbopumps	Turbomolecular	2000HT	2000 L/s
Backing (Turbo)	2-stage Rotary Vane	DS1602, DS1002	1380, 900 L/m

3.3.3 The Nozzle

The orifice separating the high pressure gas cell and the expansion chamber would take the form of a nozzle. The nozzle shape and size expressly determine the characteristics of the gas jet formed when the helium carrier gas expands from the high-pressure chamber through the nozzle to a region of chamber pressure. Calculations (discussed in the next section) and experimental measurements strongly suggested a horn-shape nozzle (Figure 3.3).

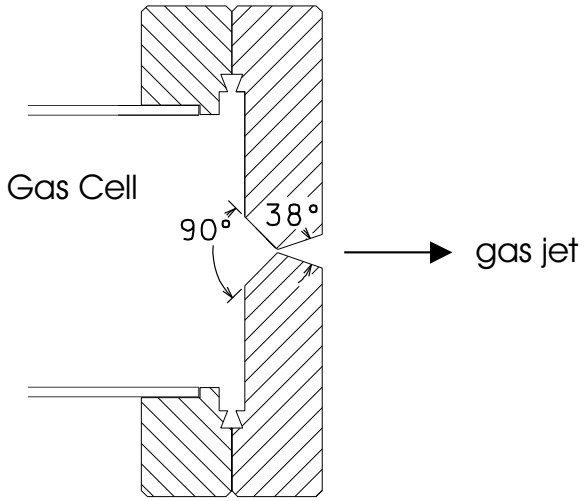

Figure 3.3: Schematic of the (calculated) optimized supersonic nozzle shape.

It was soon thereafter considered a supersonic nozzle, as the typical velocities of the gas in the expansion chamber (immediately downstream of the nozzle) would exceed the speed of sound, C, in a gas:

$$C = (gRT/MW)^{1/2} \tag{3.1}$$

where g is the adiabatic constant, R is the gas constant, T is the temperature and MW is the molecular weight of the gas.

3.4 Gas Jet Calculations

3.4.1 Background

In addition to understanding of the shape of the expanding free gas jet, a simulation, or preview, of the jet was required to complete the design of the gas cell-expansion chamber combination. In this way, certain parameters of the gas stopping station (i.e., gas cell pressure, nozzle shape and size, and geometries) could be identified to optimize our ability to stop and transport ions given the physical constraints of the chambers and pumps that already made up the Gas Stopping Station.

Our understanding of the gas jet was greatly enhanced by collaboration with Dr. Victor Varentsov from St. Petersburg, Russia. He contributed experimental knowledge and perform detailed calculations using his own computer code to provide a thorough description of several gas jets based on varying input parameters. Some of the results of these calculations are described in the sub-section which immediately follows.

3.4.2 Description of the Calculations

Complete calculations describing the viscous flow and subsequent free gas jet were undertaken using the VARJET code [50] based on a solution of full time-dependent system of Navier-Stokes equations for multi-component gas mixtures including device geometry, type of gas or mixture, and background pressure and temperature. The pressure in the gas cell is high enough that the mean free path of the atoms is small compared to the opening in the nozzle, so that the flow is viscous [51].

In short, the Navier-Stokes Equations are partial differential equations which describe the laminar flow (motion) of compressible or incompressible, non-turbulent fluids. Such equations are made from a set which expresses conservation of mass, linear momentum and energy for general motion. The conservation laws are applied to individual cells in a grid, one by one. The entire grid is iterated until a steady state is achieved. The calculations are performed in two dimensions, with cylindrical

symmetry assumed (and satisfied in the Gas Stopping Station) to complete the third dimension.

3.4.3 The VARJET Code

Before calculation could begin, Dr. Varentsov carefully divided the volume under consideration into cells (see Figure 3.4). The size of these cells was determined by the volume under consideration. As show in Figure 3.4, the cells could be coarser in the areas which were expected to see relatively small gradients in the gas flow parameters (pressure, density, velocity). The time steps between calculations were typically of the order of microseconds, but depended on the size of the cell and, again, the gas flow parameters.

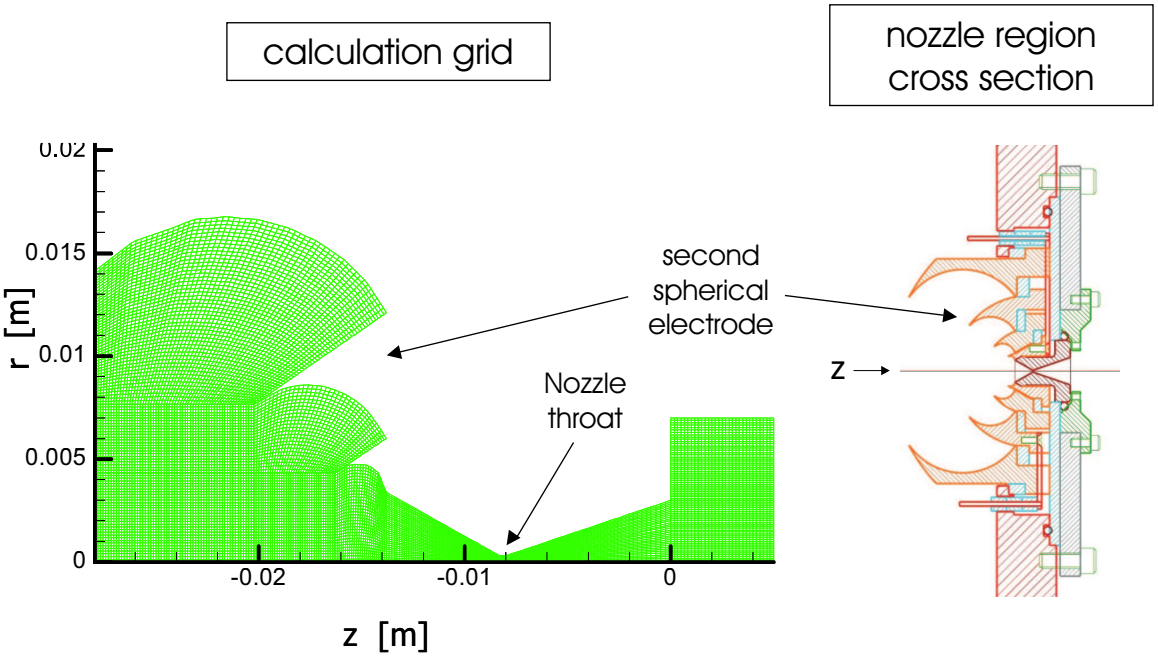

Figure 3.4: On the left, an example of a grid which represents the two-dimensional extraction geometry used for calculation under the VARJET code. The right portion shows a cross section of the nozzle region including spherical electrodes.

The last requirement before calculation was the input of the expected experimental parameters: stagnation (or static background) pressure in the gas cell, background pressure (determined by the orifice size and pumping speed), temperature and the

physical sizes of the devices under study.

The output of the calculations could be translated into jet temperatures and velocities. However, the most important result of the calculation was the pressure profile of the gas jet; i.e., the density of the carrier gas (and therefore, a density of the ions). An example pressure profile is shown in Figure 3.5.

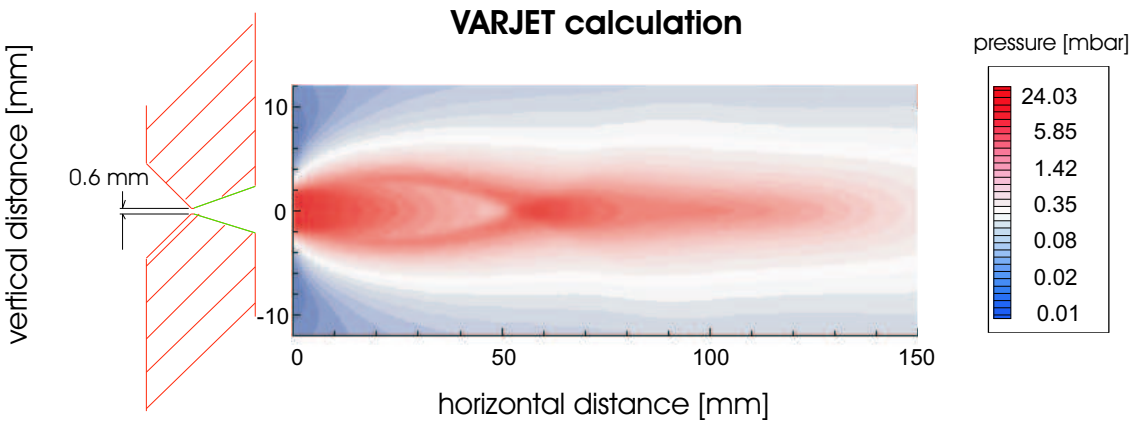

Figure 3.5: VARJET calculation showing pressure profile of free expanding jet for 1 bar helium gas pressure in the gas cell.

The location of the Mach disk (high pressure region where the jet re-converges) at approximately 32 mm nearly agrees with the prediction (39 mm) of Beylich's imperial formula [52]:

$$X = 2/3 \cdot D(P_o/P_a)^{1/2} \tag{3.2}$$

where X is the distance from the nozzle to the Mach disk, D is the nozzle throat diameter, P_o is the stagnation pressure and P_a is the ambient pressure.

From these calculations, we could focus our search for the proper parameters (stagnation pressure, nozzle shape and size) and focus our measurements on conditions displaying these optimal parameters.

3.5 Gas Jet Measurement Data

3.5.1 Introduction

A series of measurements of the pressure downstream from nozzles with two different shapes were performed as a function of helium pressure. These measurements were carried out with a Pitot tube mounted on a mechanical translator. The results are described immediately hereafter.

3.5.2 The Pitot Tube

Background

A Pitot tube can measure a fluid flow's static pressure ("overpressure") by changing the flow's kinetic energy into potential energy. The transformation takes place at the stagnation point, at the Pitot tube entrance. The kinetic to potential energy change results in a pressure greater than the free jet (dynamic pressure). A manometer can then be used to measure the static pressure. A Pitot tube typically is the device used to measure air speeds in airplanes. A simple conversion of the measured static pressure can give the relative fluid velocity.

NSCL Gas Jet Measurement Equipment

In the earliest iterations of the gas jet measurements, a simple re-entrant cylinder was crafted to function as the gas cell. On its upstream side, it had an inlet to allow introduction of helium from a gas bottle. Its downstream stainless steel flange contained the nozzle. The supersonic nozzle, shown Figure 3.6, was machined at the NSCL.

A mechanical translator was designed, built and installed into Cross A (the expansion chamber) to facilitate the gas jet measurements. This device served to firmly hold the Pitot tube and to precisely position the Pitot tube during its transverse

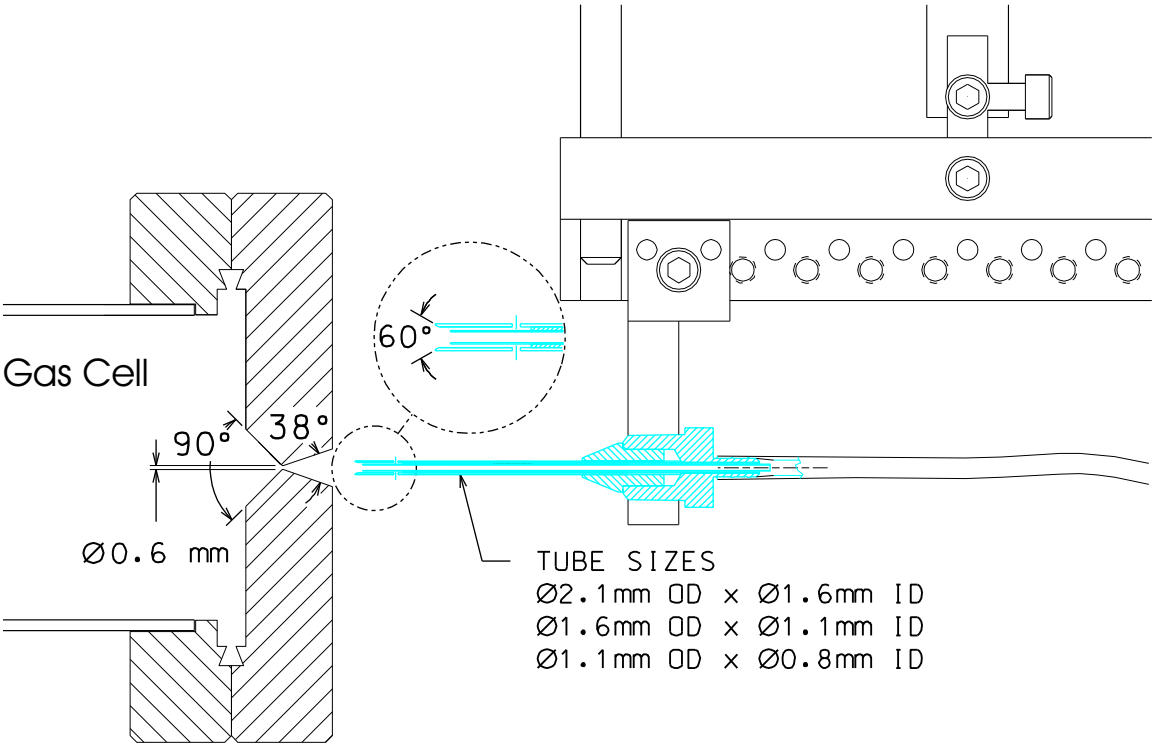

Figure 3.6: Nozzle and Pitot tube diagram with dimensions.

Figure 3.7: Pitot tube photograph.

and longitudinal movement through the gas jet. Assuming the circular nozzle cross section would produce a cylindrically symmetric gas jet, the transverse movement of the Pitot tube was limited to a vertical plane. Limiting the tube's movement to two dimensions also greatly reduced the complexity of the movement mechanism.

The vertical movement of the Pitot tube was driven by a linear motion feedthrough positioned above Cross A. This arrangement allowed extremely fine adjustment from outside the chamber and knowledge of the tubes vertical position (within 0.1 mm). The vertical range of the feedthrough was 25 mm. Therefore, the Pitot tube could

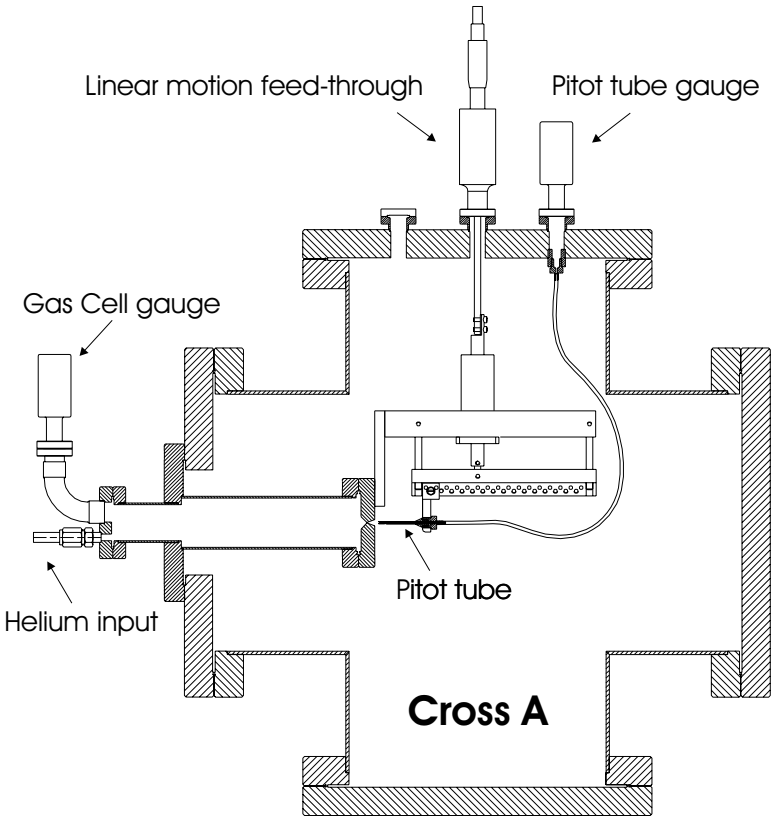

Figure 3.8: Layout for Pitot tube measurements.

travel about 12.5 mm above and below the center of the orifice. The horizontal, or longitudinal, movement of the tube was accomplished by manual movement of the Pitot tube's fixing mechanism along a perforated bar. Here the adjustment could not be made from the chambers exterior. The horizontal movement was constrained to one cm increments and had a range along the gas jet's axis of 15 cm.

Finally, plastic tubing transmitted the static pressure measured by the Pitot tube to a gauge attached to the outside of Cross A.

3.5.3 Gas Jet Measurements

An MKS Baratron (capacitance manometer) transducer (range up to 100 torr) controlled by an MKS 937A Multi-gauge controller determined the static pressure. An MKS 317 Convection Enhanced Pirani gauge determined the background pressure in the expansion chamber with the same multi-gauge controller interpreting the Pirani

transducer. The typical stagnation pressure in the gas cell was 1 bar (∼750 torr), while the background pressure in the expansion chamber was ∼0.6 mbar (∼0.5 torr).

An example of the data obtained during a Pitot tube measurement is summarized in Table 3.4.

Table 3.4: Representative data taken from Pitot tube measurements. The data is measured on the supersonic nozzle with 760 Torr (1.01 bar) helium pressure in the gas cell. The Pitot tube is in the first horizontal position, placing its tip 3 mm distant from the downstream nozzle face.

Vertical position [mm]	Pitot tube pressure [Torr]	Background pressure [Torr]
20.0	0.11	0.050
19.0	0.11	0.050
18.0	0.12	0.051
17.0	0.18	0.051
16.5	0.25	0.051
16.0	0.36	0.051
15.5	0.70	0.051
15.0	2.0	0.051
14.5	6.9	0.051
14.0	16	0.051
13.5	15	0.051
13.0	16	0.051
12.5	16	0.051
12.0	20	0.051
11.5	18	0.051
11.0	14	0.051
10.0	1.8	0.051
9.0	0.39	0.051
8.0	0.19	0.051

Approximately 20 measurements were made at each of 15 horizontal points for five different stagnation pressures with two different nozzle configurations. In all, about 3000 separate measurements were performed. The results from a complete two-dimensional measurement of the nozzle at one pressure is shown in Figure 3.9.

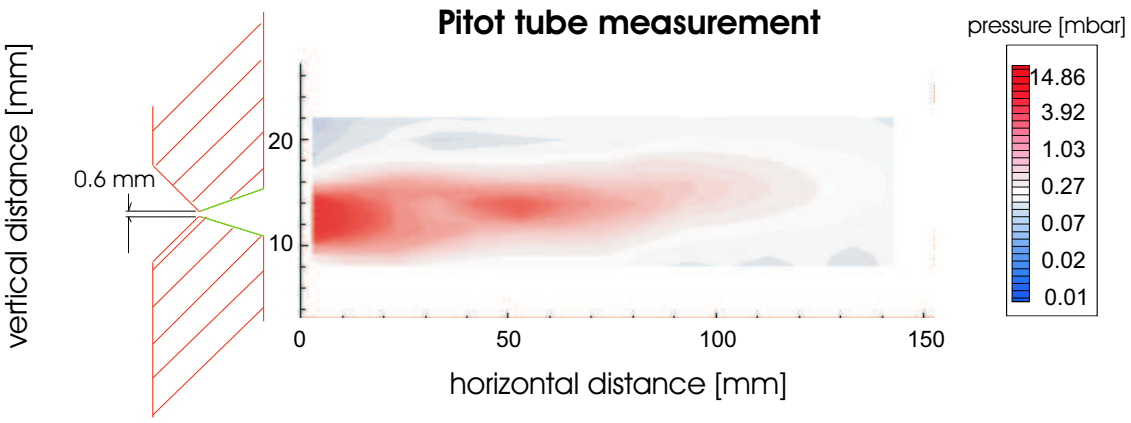

Figure 3.9: Pitot tube measurement showing pressure profile of free expanding jet for 1 bar helium pressure in the gas cell. Compare with calculation made under the same conditions (Figure 3.5).

3.6 Results and Interpretation

3.6.1 Comparison to Calculations

The measurements show good agreement with calculations (see Figure 3.10). The features of the gas jet show excellent qualitative agreement: (1) the size (length and width) agree, (2) the structure is quite similar: a convergence point followed by region of higher pressure.

One comment is offered regarding the apparent slant in the jet observed in the nozzle measurement. The results show an approximate a 3 mm vertical deviation over a run of 100 mm ($\sim$1.7 degrees). To further explore this, the nozzle was rotated by 90 degrees and again showed a slant. This is attributable to imprecise machining; that is, the throat of the nozzle was not exactly normal to the flange surface. The fixing of the nozzle flange to the gas cell was checked by micrometer to ensure that the flange was uniformly tightened to the gas cell.

3.6.2 Nozzle Gas Jet Characteristics

The general qualities of the gas jet expanding through the nozzle seem favorable. The axial size of the jet is small; that is, the ions are largely confined to the beam axis and

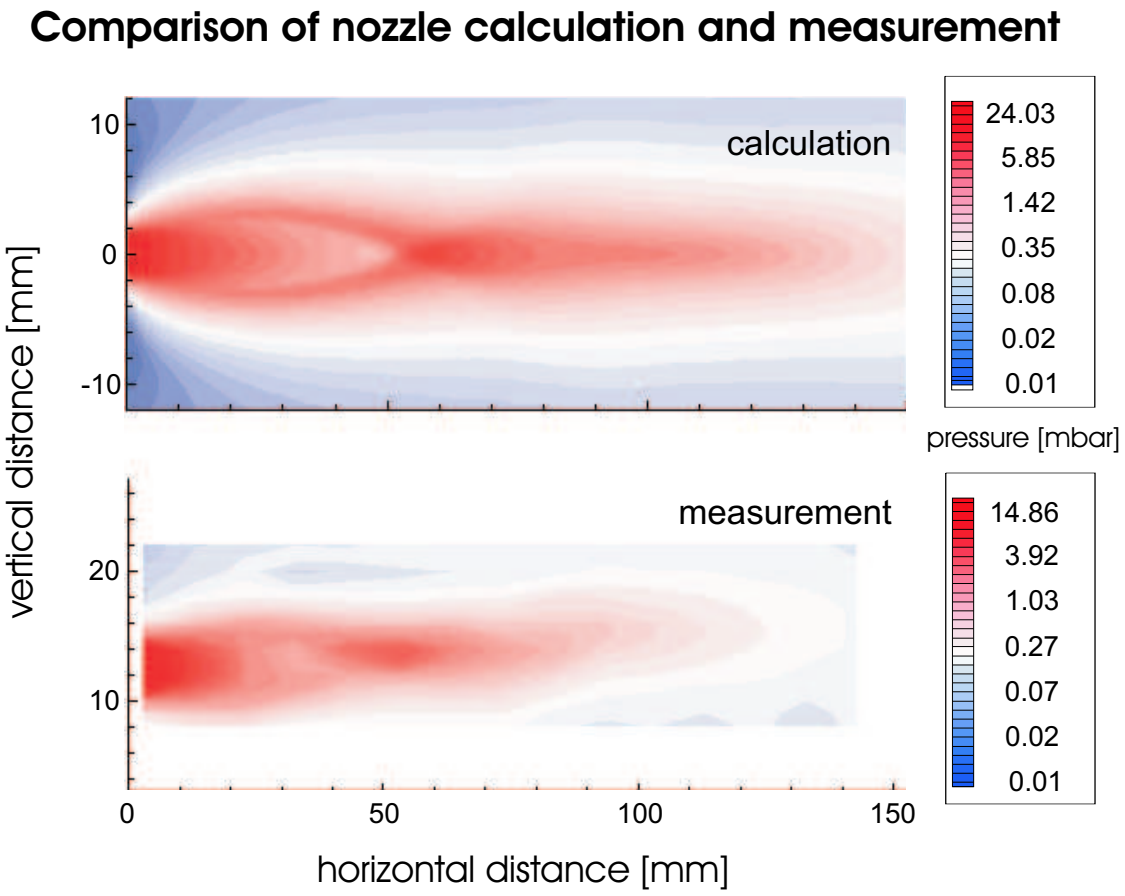

Figure 3.10: Comparison of nozzle calculation and measurement under the same conditions (1 bar helium pressure in the gas cell).

the acceptance of the ion guide. In addition, the length of the jet is useable; that is, the jets horizontal footprint will be largely confined to the expansion chamber (Cross A).

3.6.3 Simple Orifice Characterization

As a check on the measurement and the calculation, we replaced the nozzle with a simple orifice (1 mm diameter) and repeated the measurements. The results are shown in Figure 3.11. Notice that the measured pressure map is not slanted.

Again, the measurement agrees quite well with calculations. In this case the measurement was performed *before* the calculation. After the Pitot tube measurements, we transmitted only the measurement parameters (nozzle shape, stagnation and back-

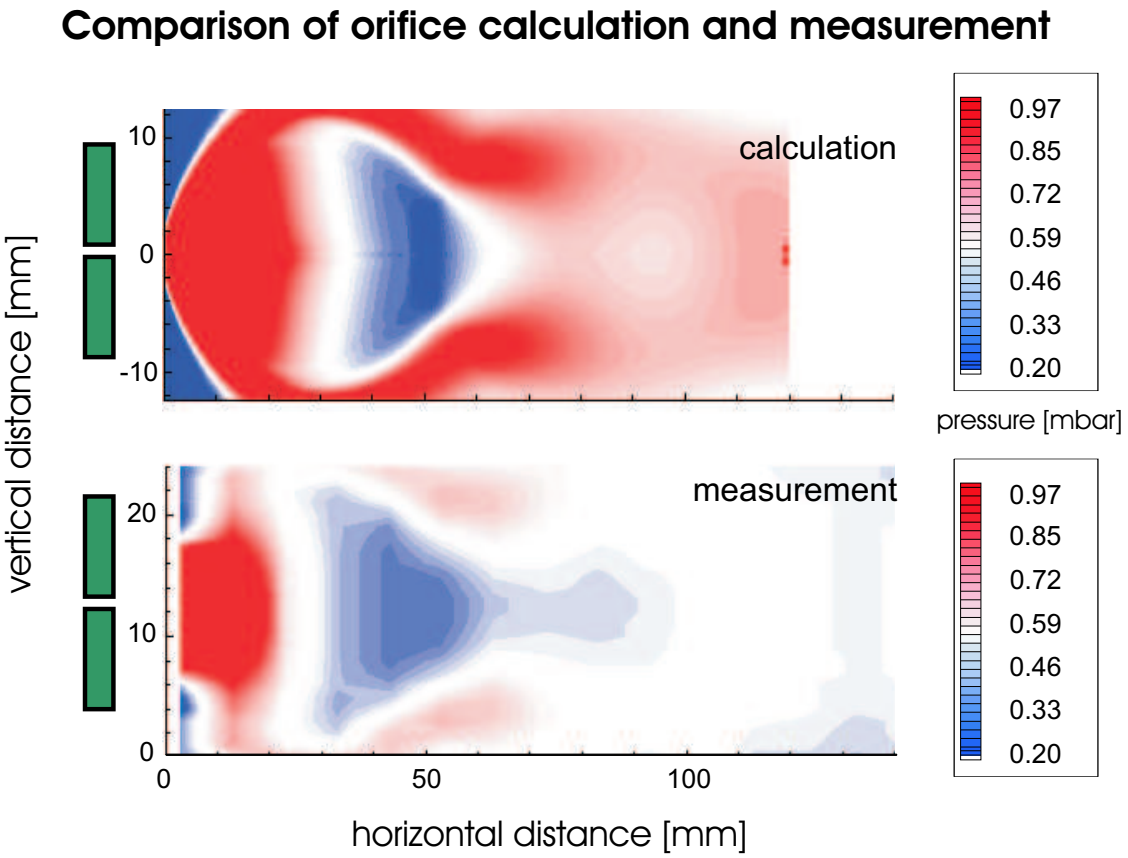

Figure 3.11: Comparison of 1 mm orifice calculation and measurement under the same conditions (1 bar helium pressure in the gas cell).

ground pressures) to Dr. Varentsov who undertook the calculations and replied with the diagram in Figure 3.11 (orifice calculation).

The orifice is clearly not suitable for our needs. To transport the ions downstream, we will use an RFQ ion guide. This RFQ will have an inner clearance diameter of 14 mm. That is, 7 mm above and 7 mm below the nozzle opening. In the previous figure (orifice), the vertical scale is in mm. Using this 'nozzle' shape, one can see that the jet 'blows up' quickly upon expanding through the orifice. That is, such a jet shape would not be compatible with our RFQ–the ions would not be efficiently captured and confined to the beam axis.

3.6.4 Gas Jet Measurement Conclusions

As a result of the calculations and experiments involving gas flow, we decided upon the optimal conditions for our gas stopping system. With some knowledge of the extraction times offered by reasonable electric fields at given pressures, a pressure of one bar (and length of 50 centimeters) was chosen for the gas stopping cell. The supersonic (horn-shaped) nozzle, with a 38 degree angle on the low pressure side was selected for the orifice.

Chapter 4

Ion Extraction

4.1 Introduction

Having studied the stopping of ions in helium and the flow of the carrier gas through the supersonic nozzle, we turned our attention to the extraction of ions from the gas cell and to the transporting of these ions to LEBIT's low energy buncher/accumulator. The fast and efficient extraction and transport of rare, short-lived ions is overall goal for the project. This work covers experiments in extracting ions from the gas cell, but contains no data on ion transport. Such tests are currently underway, so only a brief description of the ion transport system will be provided for reference in this chapter and Appendix A.

4.1.1 Extraction Requirements

The ultimate goal is to measure short-lived ions that are at the limits of nuclear stability and thus appear with short half-lives. As such, speed and efficiency in the extraction and transport process are essential to facilitate the study of the most interesting radioactive ions. Our goal is to make measurements on ions with half-lives on the order of tens of milliseconds. A quick order of magnitude calculation shows that for our gas-flow system with 10 Watts throughput and 1 bar helium gas cell

pressure, the conductance through the nozzle will be $\sim 10^{-4} m^3/s$. For our cylindrical gas cell with a length of 50 cm and a diameter of 21 cm, this would result in an evacuation time constant, τ, of approximately 170 seconds with gas flow alone. In this amount of time, all the short-lived ions would be lost to decay. It is easy to see that the extraction of ions from the gas cell is the rate-determining step in the entire process. The time between fragment production and gas stopping is on the order of 1 μs. Once ions have cleared the supersonic nozzle, the time required to transport ions to the LEBIT low-energy experimental stations is on the order of a few ms. Clearly then, the evacuation of ions from the gas cell requires additional means to hasten the travel of ions to the nozzle. A system to quickly extract the ions with the greatest efficiency would then be complete.

4.1.2 Equipment

We developed an extraction and transport scheme which would use DC potentials to extract ions from the gas cell and a combination of DC and rf potentials in the ion guide system to capture the ions on the beam axis and transport them downstream. Figure 4.1 illustrates the extraction and transport concept, highlighting the pressures and qualitative features of the electric potentials the ion will encounter along their path. After coming to rest in the 1 bar helium of the gas cell, drift (ring) electrodes will form a DC gradient to push ions toward the nozzle. Spherical electrodes (not shown) inside the gas cell will focus the ions toward the nozzle with their funnel-shaped DC field. The ions will see a potential difference between the upstream side and the downstream side of the nozzle, while being swept forward as part of gas jet. The jet will be captured in the first RFQ section (A) which is segmented to provide both an rf field to keep ions on axis and a DC gradient to push them downstream. In this region (A) most of the helium will be removed by the large pumping system. The ions then pass through a skimmer into the B and C sections of the RFQ. These RFQ sections are also segmented, but currently are placed at the same DC potential so

that the ions feel only the rf field. Finally, after leaving the Gas Stopping Station, the ions encounter accelerating electrodes which drive them through the remainder of the LEBIT beam transport system and towards the accumulator/buncher and Penning Trap.

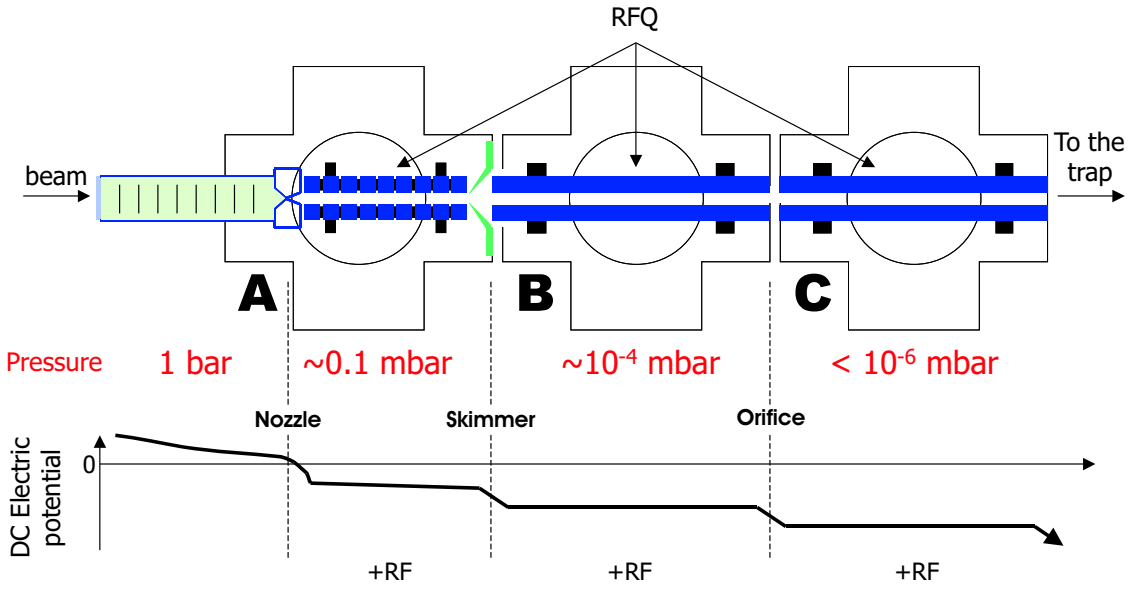

Figure 4.1: The gas cell extraction scheme with pressures in the differentially pumped system and potentials along the length of the beam axis. All three RFQ sections are segmented, but only the first section (Cross A) is shown this way. This is to allow a DC gradient to be applied across its length. Currently, RFQ sections B and C have the same DC potential down their entire lengths.

Drift Electrodes

The system of drift electrodes consists of 21 polished aluminum (type 6061) rings and a support structure fixed to the same flange which holds the beryllium window (see Figure 4.2). The rings have a 5.6 cm inner diameter, a thickness of 4 mm and a center-to-center spacing of 2.2 cm. They run the length of the gas cell, with the first ring 6 cm downstream of the beryllium window and the last ring 1.5 cm from the first (largest) spherical electrode (Figure 4.3). The rings are fixed in place by three support rods which are attached to the window flange. The entire assembly is inserted into the gas cell from the upstream side. The support rods each consist of a threaded stainless

steel rod inside a Macor tube with Macor spacers between the rings. Macor is a low outgassing, high temperature machineable glass ceramic. DC voltages are applied to the rings to form the gradient along the length of the gas cell. These are applied to the rings via five feedthroughs which are connected to the 1st, 2nd, 6th, 16th and 21st rings. The remainder of the rings have their voltages delivered from these five connections by resistive chains. These chains use 1 MΩ RX-1M resistors (inside the gas cell) from Ohmite Manufacturing Company which are hermetically glass sealed for use in ultra-high vacuum applications.

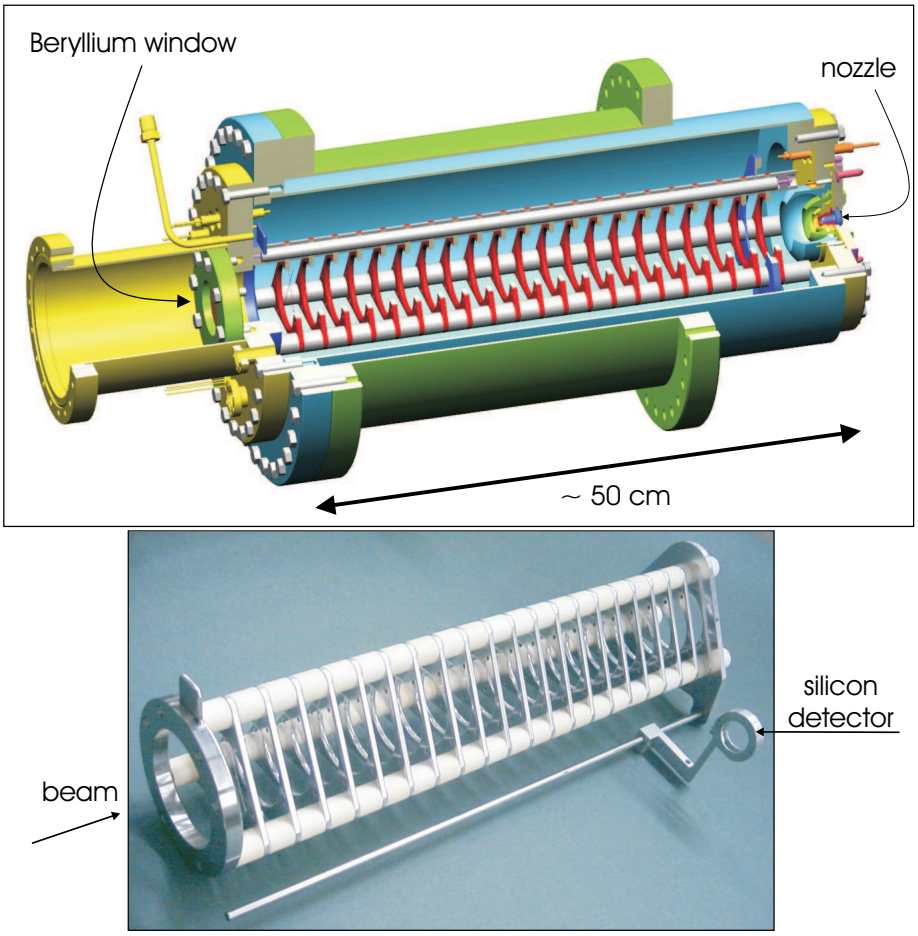

Figure 4.2: Cutaway mechanical drawing (above) and photograph (below) of the drift (or ring) electrodes. The 21 rings' inner diameters are 5.6 cm and their center-to-center spacing is 2.2 cm. Also shown in the photograph is the silicon detector mount which allows the detector to be inserted into or removed from the beam axis by means of a rotary feedthrough.

Spherical Electrodes and Nozzle

The drift electrodes form a field to push the ions toward the nozzle along trajectories parallel to the beam axis. However, in order to focus the ions toward the small throat of the nozzle, spherical electrodes were added inside the gas cell (Figure 4.3). These four electrodes form a funnel-shaped field which concentrate the ions towards the nozzle. Once the ions approach within a few millimeters of the nozzle's throat, gas flow takes over, sweeping the ions out of the gas cell. Stefan Schwarz developed a design of the spherical electrodes to form the appropriate field while maximizing the number of ions which would reach the nozzle. The electrodes are made of aluminum (type 6061) and have Macor separators acting as insulators. The diameters of the electrodes' sharp tips (furthest upstream) are 45.8, 28.2 15.2 and 9.0 mm. The entire package of electrodes, insulators and nozzle are secured, with the addition of an o-ring seal, to the flange which makes the downstream boundary of the gas cell. Biases to the spherical electrodes are provided by feedthroughs which enter at the top of Cross A, pass through the nozzle flange, and make contact with the electrodes in the 1 bar of helium. The design of the extraction electrode system was complicated by the fact that the entire system must hold a pressure of greater than 1 bar of helium (in the gas cell) with vacuum on either side. Significant effort was necessary to design the seals and the high voltage feedthroughs.

The nozzle was machined entirely from the semiconductor germanium (by Lattice Materials Corporation) with the intent of placing different potentials on its upstream and downstream side (-166 and -190 Volts, respectively). Holding a large potential difference across the germanium nozzle proved difficult, and it will soon be replaced by a silicon version.

Simulations

In order to minimize the evacuation time and maximize the extraction efficiency, the geometry and voltages of the drift and spherical electrodes required optimization.

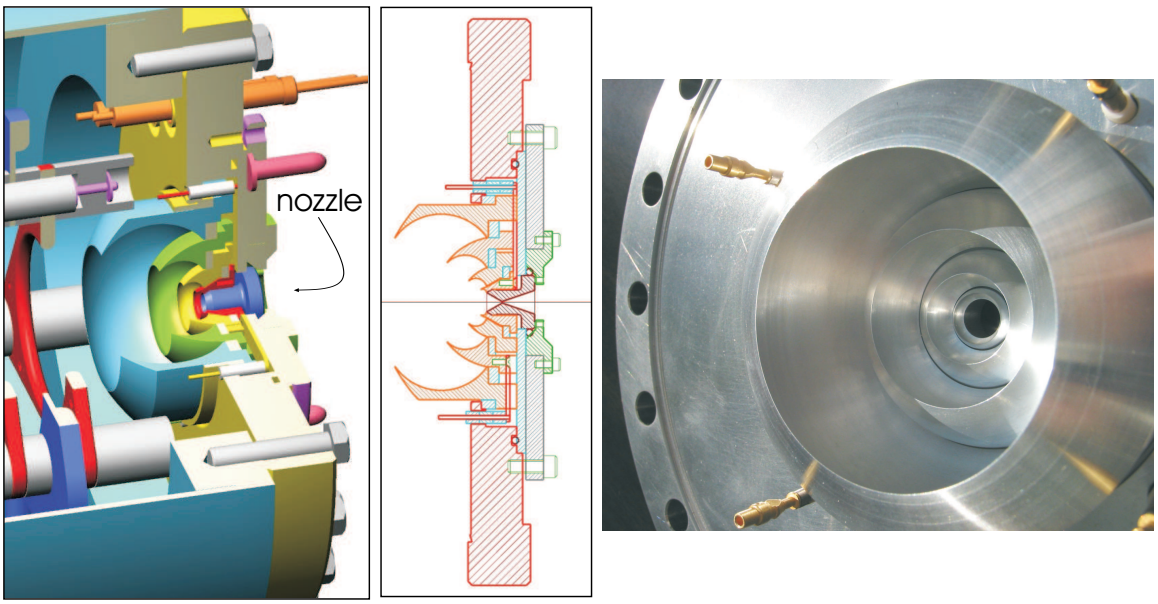

Figure 4.3: Cutaway (left) and cross section (center) mechanical drawings of the spherical electrodes and supersonic nozzle. For comparison, the (red, triangular) drift electrode's inner diameter is 5.6 cm. On the right is a photograph of the electrodes and their mounting flange.

Peter Schury of the LEBIT group performed SIMION (3D version 7.00) [53] beam transport simulations with the constraint that the highest potential in the gas cell would be approximately +2000 Volts. Spark breakdown tests showed that the high voltage feedthroughs would tolerate, at most, roughly 2 kV in helium. It is known that the breakdown voltage in helium gas is a factor of 5-6 times lower than that in air.

SIMION simulations using a viscous drag force showed that, for a stopping distribution centered along the length of the gas cell at 1 bar, more than half the ions should be extracted in less than 60 ms. The voltages applied to the electrodes for the simulation are given in Table 4.1. Shown in Figure 4.4 are the field lines created by the electrode potentials and the time required for extraction depending on the position where the ion comes to rest. It is also worth noting that the simulation includes the dependence of extraction time on gas cell pressure (given that the electric potentials remain constant). While higher gas cell pressures can stop a larger fraction of the incoming ions, more short-lived ions could be lost due to longer extraction times. Data

Table 4.1: Optimized voltages for the drift (ring) and spherical electrodes in the gas cell.

Ring	[V]	Ring	[V]	Ring	[V]	Spherical	[V]
1	1136	8	1075	15	915	1	565
2	1130	9	1055	16	885	2	420
3	1125	10	1045	17	855	3	225
4	1115	11	1015	18	815	4	-160
5	1105	12	995	19	775		
6	1095	13	975	20	670		
7	1085	14	945	21	590		

on the extraction times will be available when tests with a laser ablation system are performed in the future (see Chapter 5).

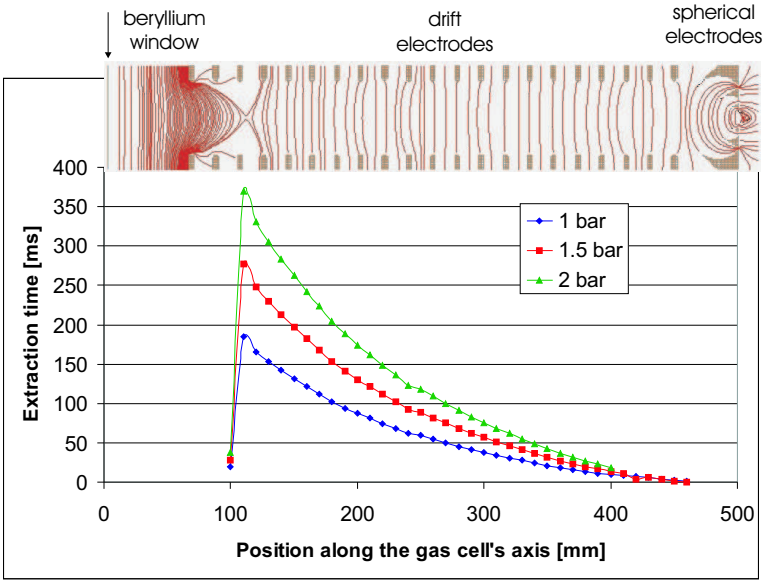

Figure 4.4: Simulation results for gas cell extraction produced by the software SIMION. The field lines created by the electric potentials are shown in the inset at the top of the figure. The extraction times for various gas cell pressures is also shown. Note that ions stopping in the first 10 cm of the gas cell will not be extracted.

4.2 Extraction Measurements

We decided to make measurements of the extraction efficiency with a collection electrode just downstream of the nozzle. The extraction efficiency is the most important unknown quantity in our system and these tests did not require the operation of the

RFQ ion guide.

4.2.1 Experimental Setup

We chose to measure the extraction efficiency by detecting the gamma rays of extracted radioactive beam. This would provide unambiguous evidence that a specific nuclide had exited the gas cell. Careful consideration determined which nuclide would be measured based on the available primary beam, secondary beam purities and nuclide half-lives and decay energies. To perform the gamma ray detection, the layout of Cross A of the Gas Stopping Station was altered (Figure 4.5) to include an ion collection electrode on a β detector and a nearby germanium detector.

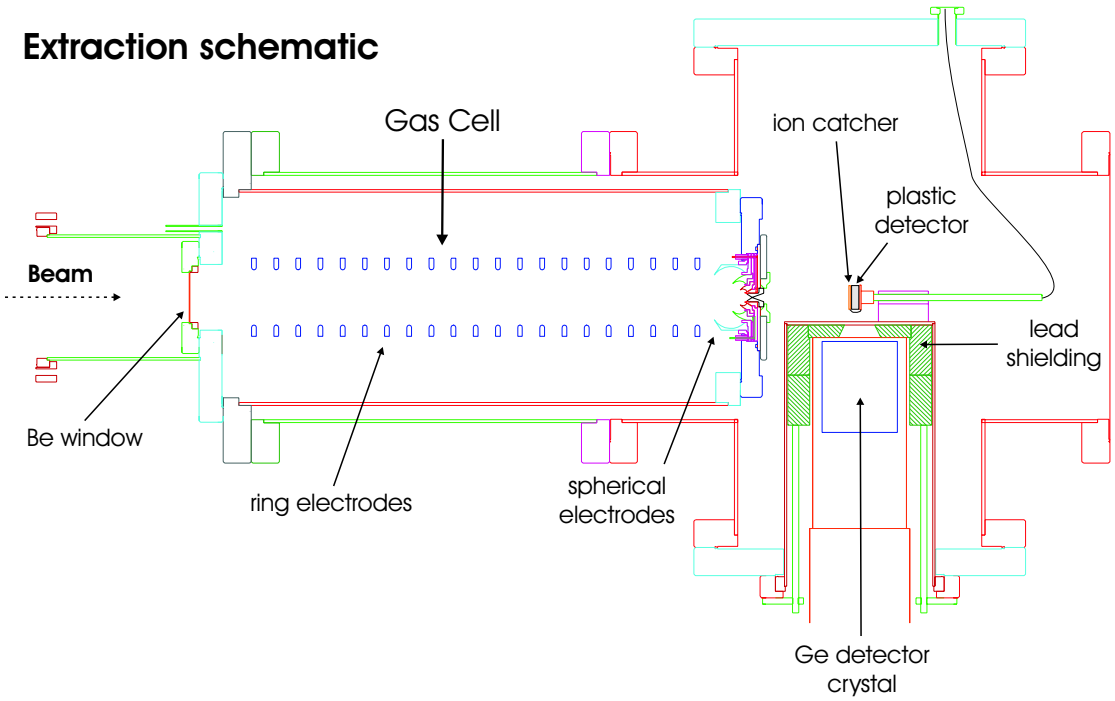

Figure 4.5: Schematic of the extraction test. Ions were captured on the catcher by applying a negative potential. Upon decay, beta particles could be registered in the plastic scintillator detector and gamma rays could be observed by the germanium detector.

A re-entrant cylinder provided close geometry for an Ortec germanium detector and lead shielding (to reduce the number of detected gamma rays originating from other than the catcher–most notably the spherical electrode region). The ion catcher

(a 2.5 cm diameter disc), with a plastic scintillator detector behind it, was mounted on a rod, moveable along the beam axis. The longitudinal placement of the ion catcher was determined by the position of a high pressure in the gas jet, at approximately 9 cm, and the center of the germanium detector. In order to hold a bias, the catcher was electrically connected to the metal mount (and rod) behind the plastic detector. Positive and negative high voltage was applied via a feedthrough in cross A connected to the metal rod. The concept was, for detecting positive ions, that ions (and their decay gamma rays) should be observed for a negative bias on the catcher while few ions should be seen for a positive bias. The plastic scintillator detector could count beta particles and allow for beta-gamma coincidences to be observed. The detectors were calibrated by gamma/beta and gamma sources placed at the catcher. The standard sources covered a range of energies from approximately 300 to 1800 keV. The plastic detector (1 cm thick and 2.5 cm in diameter) had an efficiency of 0.30. The germanium detector was an Ortec (120%), and we determined its efficiency as 0.007 for 1568 keV gamma rays in its given geometry.

A slight deviation from the optimal electrode voltages was used. Because the resistivity of the germanium nozzle could not hold the required potential difference across its two ends, the voltage scheme required adjustment. The potentials used for this extraction are given in Table 4.2.

Table 4.2: Voltages for the drift (ring) and spherical electrodes used in the gas cell extraction experiments.

Ring	[V]	Ring	[V]	Ring	[V]	Spherical	[V]
1	1135	8	1055	15	966	1	565
2	1130	9	1038	16	885	2	420
3	1125	10	1023	17	826	3	225
4	1118	11	1009	18	767	4	18
5	1110	12	997	19	708		
6	1095	13	985	20	649		
7	1074	14	975	21	590		

4.2.2 Extraction Data

As previously mentioned, in determining a candidate radioactive ion for extraction tests, many factors came to bear: available primary beam, secondary beam rate and purity, and nuclide half-life and gamma-ray energy. Table 4.3 summarizes the ions we considered for extraction studies..

Table 4.3: Summary of extracted secondary beams.

Primary Beam, Energy [MeV/A]	Secondary Beam, Energy [MeV/A]	$T_{1/2}$
^{36}Ar, 130	^{32}P, 111	14.3 d
^{86}Kr, 140	^{80}As, 93.6	15.2 s
^{40}Ca, 140	^{38}Ca, 91.9	440 ms

Among the three nuclides we studied for extraction, the most ideal candidate was ^{38}Ca, with its 440 ms half-life and strong gamma ray at 1568 keV (branching ratio of 21%). The short half-life reduced the contribution of build-up in the gamma spectra and the 440 ms was more closely matched with those we expect to measure in the future. The 1568 keV gamma ray energy was well beyond the background gamma rays and then continuum at 511 keV from positron decay. In addition, our detection technique continually improved with experience, so only the data on ^{38}Ca is presented here.

The conditions for the extraction test of ^{38}Ca follows. Table 2.8 lists the beam parameters for this secondary beam of approximately 92 MeV/A which was delivered to the Gas Stopping Station. A single 1.49 mm glass degrader plate turned to 24.1 degrees (the angle determined for greatest stopping efficiency, as discussed in Chapter 2) and the M1 mono-energetic wedge (0.736 mm middle thickness and 2.4 mrad angle) degraded most of the beam energy before the ions passed through a 1.0 mm thick beryllium window into the gas cell containing a helium pressure of 780 Torr (1.03 bar). The collector voltage was set, in alternating 10 minute runs, to either +350 or -350 Volts. The cyclotron beam was cycled on (3 seconds) and off (3 seconds) to reduce

the contribution of prompt gamma rays. The voltages for the electrodes were set as previously described (Table 4.1) with some exceptions. Due to a problem with the nozzle electrode system, the nozzle voltage was set to ground and the final (smallest) spherical electrode was set to 18 Volts. The adjusted voltages are summarized in Table 4.2. The responses of the plastic scintillator and the germanium detector were observed to compare the effect of the differences of the positive and negative catcher voltage. An extraction rate and efficiency could then be deduced from this comparison.

Shown in Figure 4.6 are the data from the response of our two detectors. The germanium detector shows $\sim$20% effect between the positive and negative catcher voltages for the 1568 keV gamma rays of ^{38}Ca. This relatively low difference can be attributed to detection of gamma rays emitted from nuclei not on the catcher. As seen in Figure 4.5, the available space and geometry which only allows for limited shielding of gamma rays coming from nuclei stopped in the region of the nozzle and spherical electrodes. The beta spectra show a larger effect between the positive and negative voltage (Figure 4.6 lower panel) due to its higher efficiency and a sensitivity to the contaminant secondary ion ^{37}K (the only other significant contaminant was the stable nuclide ^{36}Ar).

A more stringent test of ion collection is shown in Figure 4.7 where a gamma-beta coincidence is required of the same data set as presented in the gamma ray and beta singles spectra. The 1568 keV line is a factor of 16 larger for a negative voltage (albeit with low statistics).

As another test of the ion extraction, the glass degrader angle was varied about the optimal stopping angle (24.1 degrees) while the response from the beta detector was observed (gamma-beta coincidence statistics were too low). The data from the beta detector is shown in Figure 4.8. The beta detector was sensitive to both the ^{38}Ca and the ^{37}K, so the stopping curve is similar but wider than that shown in Figure 2.19 in Chapter 2. Fewer counts were observed in the plastic as the glass degrader angle was moved away from the optimal angle in either direction, showing that indeed

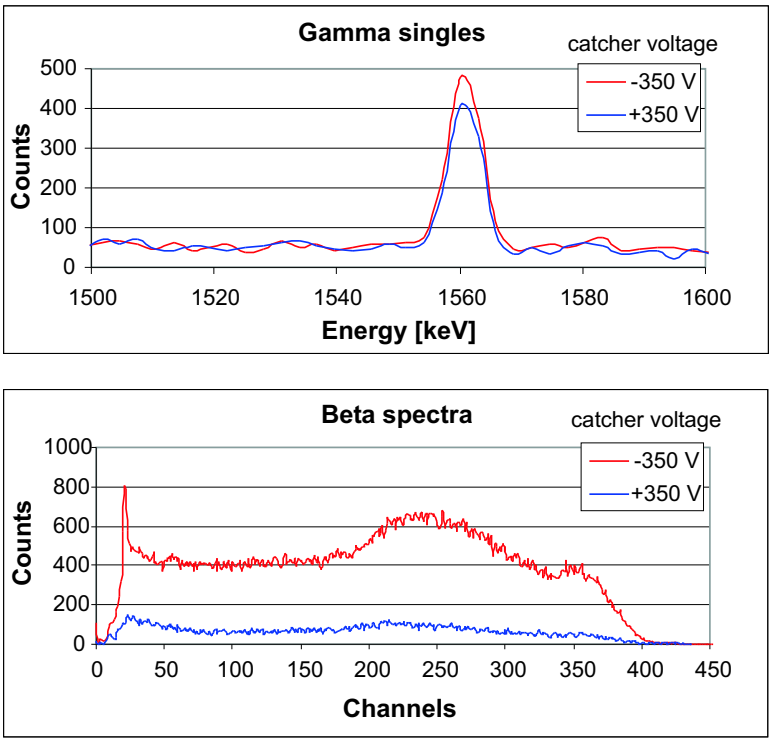

Figure 4.6: Gamma singles (upper panel) and beta spectra (lower panel) for a pair (-350 and +350 catcher voltages) of 10 minute runs at a fixed glass angle and 780 Torr (1.04 bar) helium pressure in the extraction of ^{38}Ca from the gas cell.

fewer ions were being stopped and then extracted.

4.2.3 Interpretation

The most important number derived from our extraction data is the extraction efficiency. We arrived at an efficiency by two routes: one using the beta counting data and one using the beta gated gamma data. The errors were dominated by the uncertainty in the detection efficiencies, and in the coincidence case by low statistics. In both cases the observable from the experiment is actually the combined stopping and extraction efficiency. The previously determined stopping fraction will then be factored out to arrive at the extraction efficiency.

In using the beta particle data, we make the assumption that both the ^{38}Ca and the main radioactive contaminant, ^{37}K had an equal chance of extraction given that they were both stopped in the gas cell; that is, we assume that the calcium and the

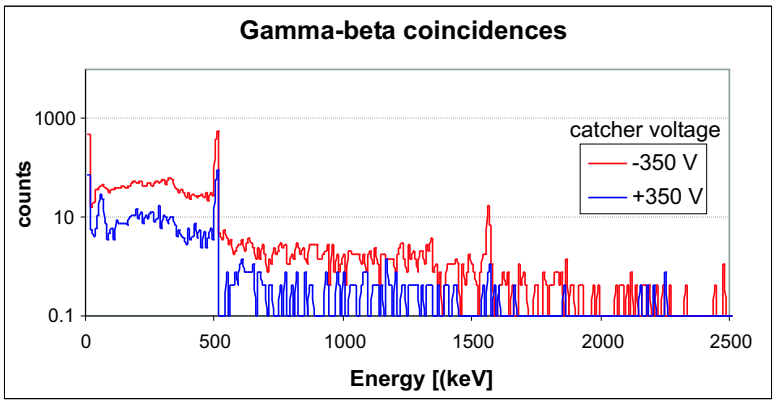

Figure 4.7: Gamma-beta coincidence spectrum using the same experimental data as seen in Figure 4.6, demonstrating the effect of switching collector voltage between -350 and +350 Volts. In this spectrum a simultaneous gamma ray in the germanium detector and beta particle in the plastic scintillator detector is required. The ^{38}Ca gamma ray is at 1568 keV.

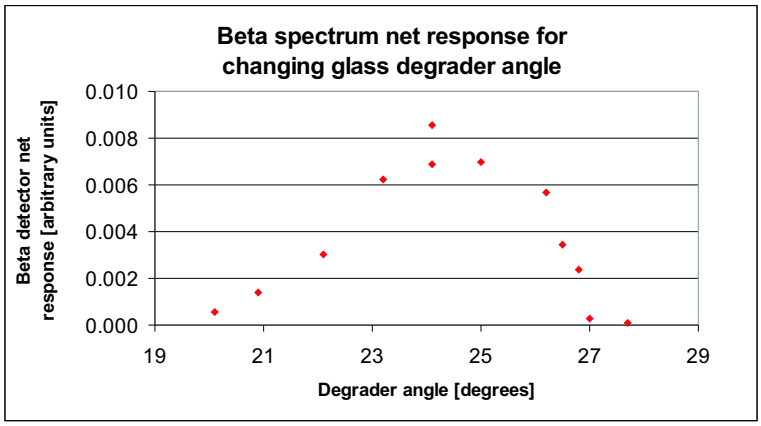

Figure 4.8: Graph of beta detector net response for a changing degrader glass angle. As the glass angle varies from the optimal angle (24.1 degrees) the beta detector response clearly is affected, showing that fewer ions are being stopped and extracted.

potassium has an equal chance to be extracted as an atomic or molecular ion (recall the particle identification presented in Figure 2.15). Now, the efficiency for extraction, ϵ_{EXTR} can be obtained from:

$$N_\beta = \epsilon_{STOP}\epsilon_{EXTR}\epsilon_\beta N_{Ca+K} \tag{4.1}$$

where N_β is the number of counts in the beta detector, N_{Ca+K} is the total number of beam particles delivered to the gas cell, and the remaining three terms de-

scribe the stopping, extraction and beta counting efficiencies. Using this method (with 25,171,296 ^{38}Ca and 14,791,380 ^{37}K ions counted and 43,524 beta events), a combined stopping and extraction efficiency of 0.36(7)% was determined, with the error dominated by the beta counting uncertainty (20%). The main error for the beta efficiency comes from uncertainty in beta counting, with the beta efficiency obtained from several sources, conservatively given as 30(5)%.

As a cross check, we also determined the extraction efficiency by using the gamma-beta coincidence data, though it had low statistics. In this case:

$$\mathrm{N}_{\beta\gamma} = \mathrm{N}_{\mathrm{Ca}}\epsilon_{\mathrm{STOP}}\epsilon_{\mathrm{EXTR}}\epsilon_{\beta}\epsilon_{\gamma,1568}\mathrm{BR}_{1568} \tag{4.2}$$

where, in considering the number of gamma-beta coincidences, $N_{\beta\gamma}$, the efficiency for 1568 keV gamma rays being detected (0.007) and the branching ration (BR) to the 1568 keV level (21%) must also be considered. Using this method, the stopping and extraction efficiency of 0.29(8)% was determined with the error dominated by contributions from the beta counting uncertainty (20%) and the low statistics of the gamma-beta data (18%).

When the previous two values for the total efficiencies, 0.36(7)% and 0.29(8)% are combined, we determine a total efficiency for our gas cell of 0.33(5)% (see also Table 4.4). This value obviously has potential for improvement, but is sufficient to allow the mass measurement of many new nuclei at the NSCL [54]. Recall that the stopping fraction (efficiency) at this degrader angle (Figure 2.19) was found to be $0.72(^{+0.13}_{-0.20})$, so that the extraction efficiency is $0.46(^{+0.11}_{-0.15})$%.

Table 4.4: The extraction efficiency for ^{38}Ca derived from the combined stopping-extraction value.

	$\epsilon_{STOP} \cdot \epsilon_{EXTR}$	ϵ_{STOP}	ϵ_{EXTR}
value	0.0033	0.72	0.0046
uncertainty	0.0005	+0.13	+0.0011
		-0.20	-0.0015

Chapter 5

Summary and Future

5.1 Data Summary and Interpretation

5.1.1 Efficiencies

A summary of the efficiencies and time required for various steps of the overall process of mass measurements are given in Table 5.1. For various secondary beams, the flight time of the ions in each section will be approximately the same on this gross scale. The pre-stopping efficiency value includes the transmission through the A1900 and to the N4 vault. The collection and transport efficiency in this pre-stopping phase is very dependent on the secondary ion. For example, the efficiency can be as high as 100% if the momentum distribution is narrower than 2%. Thus, a typical value of 1/2 is given. The stopping and extraction efficiencies were discussed in Chapters 2 and 4, respectively. Simulations of the beam optics indicate that ion losses of no more than 15% for transferring and capturing ions in the Penning Trap should be expected and typical Penning Trap detector efficiencies are known to be around 30% [54]. Thus, if we combine all of these factors, we expect an overall efficiency of $\sim 3 \cdot 10^{-4}$ from production to detection in the Penning Trap. This number is sufficiently large to allow a number of studies of exotic nuclei.

For perspective, the efficiencies of the NSCL's gas stopping system is compared

Table 5.1: Summary of data and efficiencies for the different systems of the Gas Stopping Station and LEBIT taken for a mid-mass nuclide with half-live of 100 ms. The mass measurement alone usually requires approximately $2 \cdot T_{1/2}$.

Event	Efficiency	Required time
Pre-stopping	$\sim$0.5	$\sim$0.5 μs
Stopping	0.5 - 0.7	$\sim$0.05 μs
Extraction	0.005	60 ms
Transport & cooling (predicted) [54]	0.85	10 ms
Mass measurement (predicted) [54]	0.3	200 ms
Overall	$(3.2\text{-}4.4) \cdot 10^{-4}$	$\sim$270 ms

(Table 5.2) with the most recent data from other gas stopping efforts (recall Table 1.2). The overall efficiency of the NSCL system and the RIKEN systems are similar although the geometries and the collection electrodes are rather different. The factor of two difference between these results is easily understandable. The efficiency of the ANL device is significantly higher than any other results, including all of the earlier IGISOL studies [27, 28]. The difference comes down to an extraction efficiency that is about two orders of magnitude larger than other similar efforts. The relatively small amount of information on the details of the ANL extraction studies [31] precludes a detailed discussion of the differences.

Table 5.2: Comparison of efficiencies with other gas stopping efforts (mass measurement efficiency factored out of NSCL figures from Table 5.1). The Xs mark the events which factor into the given overall efficiency.

Event	NSCL 92 MeV/A ^{38}Ca	RIKEN [29] 70 MeV/A ^{8}Li	ANL [31] $\sim$5 MeV/A ^{120}Cs
Pre-stopping	X	X	
Stopping	X	X	X
Extraction	X	X	X
Transport	X	X	X
Overall	0.001	0.002	0.43

We believe the extraction efficiency of our gas cell can immediately be boosted by an order of magnitude with improvements in the nozzle potentials. As previously mentioned (Chapter 4), our germanium nozzle could not hold the required (optimal)

voltage between its upstream and downstream face. As a result, for our extraction studies, the potential for the entire nozzle was set to zero and the voltage for the innermost spherical electrode was greatly affected. We now have acquired a silicon nozzle which has a greater resistivity and is expected to hold a much greater voltage across its length. Further SIMION [53] calculations show that while the transport of ions through a nozzle with zero Volts across its length is, at best, a few percent, a nozzle which can hold 60 Volts (achievable by our silicon version) should transport 50% of the ions that it receives.

5.1.2 Mass Measurement Prognosis

Given the efficiencies that we have attained and the performance of the NSCL's coupled cyclotrons, an estimate of the nuclides which can be measured (and the corresponding accuracies) can be determined. Shown in Figure 5.1 is the required number of detected ions as a function of half-life for a variety of nuclide masses needed to achieve a 10^{-7} statistical accuracy in the mass measurement. Therefore the required number of secondary ions *produced* by the coupled cyclotrons and A1900 can be estimated by simply dividing the y-axis in Figure 5.1 by the overall efficiency of $\sim 3 \cdot 10^{-4}$, or multiplying by 3000.

The data taken on the Gas Stopping System to date validate the assumptions of the first Penning Trap measurements proposed at the NSCL. An overall efficiency of 10^{-4} (as compared to the $\sim 3 \cdot 10^{-4}$ obtained thus far) was suggested as a target to allow measurements of several nuclides with accuracies of 10^{-7} or better. When the LEBIT system is fully functional, N$\sim$Z nuclei involved with the rp-process will be measured: $^{61-62}$Ga, ^{64}Ge, ^{65}As, $^{67-68,70}$Se, ^{70}Br, and ^{72}Kr. In addition nuclear structure beyond N=28 will be studied in: $^{40-42}$P, $^{41-44}$S, and $^{43-45}$Cl.

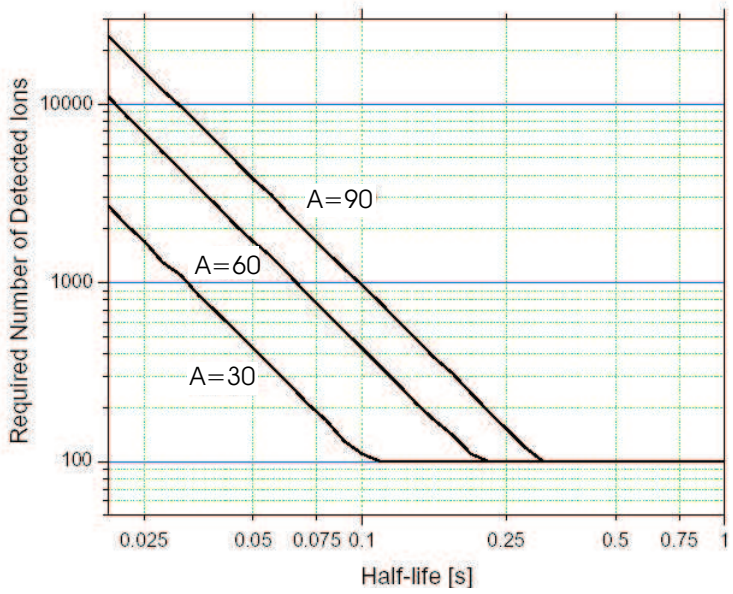

Figure 5.1: Required number of detected ions for obtaining a statistical accuracy of $\delta m/m = 10^{-7}$. Typically, a minimum of 100 ions are required to obtain a cyclotron resonance curve during mass measurements in the Penning Trap [54].

5.2 Future Work and Improvements

5.2.1 Improvements

The present studies were performed without the optimal voltages on the extraction electrodes and the nozzle. Up to the present, the nozzle was left at ground potential and the electrode potentials were scaled down to the values given in Table 4.2. We have ordered a new nozzle made from higher resistivity silicon to allow us to reach the design potentials. This change should provide a substantial increase in the extraction efficiency. All of the simulations indicate that the thermalized ions will be transported to the upstream face of the nozzle so that the electric field at the nozzle throat is critical for ion extraction.

A second improvement in the system would be to increase the volume of the gas cell. In particular, an increase in the drift electrode diameter (and a corresponding increase in the gas cell diameter) to match the 10 cm diameter of the beam line would allow for complete coverage of the degraded beam from the range-compression ion-

optical system. The drift time of the ions is only slightly dependent on their radial distribution. A larger diameter system would also allow more space for the bulky high voltage feedthroughs.

We are encouraged that we have been able to attain significant extraction efficiencies with the gas cell operating at 1 bar helium pressure. Future studies of ion collection at even higher pressures should be carried out because at higher pressures a larger fraction of the incident ions are stopped in the gas. The pumping system that we have developed should be able to run at pressures up to 5 bar, but the ion transport through the RFQ and skimmer under these conditions will require further investigation.

5.2.2 Related Other Improvements

Two projects are underway to further the work of gas stopping and beam transport. The first idea involves monitoring the beam current inside the gas cell to confirm the stopping fraction inside the gas cell. A logarithmic amplifier, able to accept a wide range of negative current will be connected to the first (furthest upstream) drift ring in the gas cell. Ions stopping in the gas will ionize the helium as they come to rest. While positive ions will be driven downstream by the electric potential, electrons will travel upstream and be collected on a sparse grid strung across the first ring. The current on this ring is directly proportional to the rate of ions stopping in the helium. Given that the energy and effective ionization potential for helium is known, the ionization rate can be monitored in a non-destructive way.

In addition, tests of ion transport through the RFQ are being undertaken. The LEBIT design included a test ion source (see Figure 5.2) which can direct a test beam steered by a four-way quadrupole deflector (located on the beamline near the ion source) either downstream or upstream. This plasma ion source is providing a beam of argon ions which are directed upstream (backwards) through the beam optics and through the RFQ towards the gas cell. Current at the gas cell nozzle is being

monitored and early results show at least 35-40% of the beam being transmitted.

5.2.3 Gamma Detection after RFQ Transport

Once the operation of the RFQ is fully tested, the original tests in which the extracted radioactive beam was collected just downstream of the nozzle by an electrode at negative voltage can be repeated near the end of the RFQ. A design for collection on a wire electrode to make such a measurement has been developed. This measurement will give us a qualitative test for ions undergoing stopping, extraction and transport through the RFQ. The design calls for a pivotable wire that will sample ions in the center of RFQ section C, remove them from the RFQ axis and position them in front of a combination of plastic and germanium detectors similar to that previously described in Chapter 4.

5.2.4 Laser Studies

A project using laser ablation to study extraction times and efficiencies is also underway. Instead of using beam from the cyclotrons, we will create ions in the gas cell by using a Nd-Yag green laser pulse to ablate a target. With knowledge of the laser pulse start time and energy, the ion start time and number can be known for a given target. By measuring the beam current and arrival time of the extracted beam at a point downstream of the nozzle, the extraction times and efficiencies can be determined.

5.2.5 LEBIT Equipment Status

After describing the future work and improvements, we would like to comment on the progress of the LEBIT project and the gas stopping initiative. The current status of LEBIT is shown via schematic in Figure 5.2. Previous chapters have detailed the progress of installation and testing of hardware in the Gas Stopping Station. The last item of equipment for collection and transport of the ions after the nozzle is the RFQ

that terminates in Cross C, which is described in Appendix A.

After the beam traverses the length of the RFQ, it will encounter accelerating and steering (correction) electrodes just beyond Cross C. Next, an einzel lens will transport the beam to the 10 degree electrostatic bender, after which the beam will be on the proper trajectory towards the Penning Trap. A second einzel lens will transport the beam through the shielding wall, past a diagnostic section, and then into the accumulator/buncher. All the aforementioned equipment (between the RFQ and the buncher) are in place and have been tested. The accumulator/buncher is under construction and nearly complete. When operational, this section of LEBIT will provide ion pulses to the experiments. A cooler section (not completed) will follow and serve to improve the emittance of the beam. Finally, after passing through a completed (but untested) beam observation and einzel lens section, the beam will be transported to the Penning Trap for mass measurement. Although the 9.4 Tesla solenoid is in place, the beamline bore tube for the magnet is being machined and the Penning Trap itself is undergoing its last iteration of design.

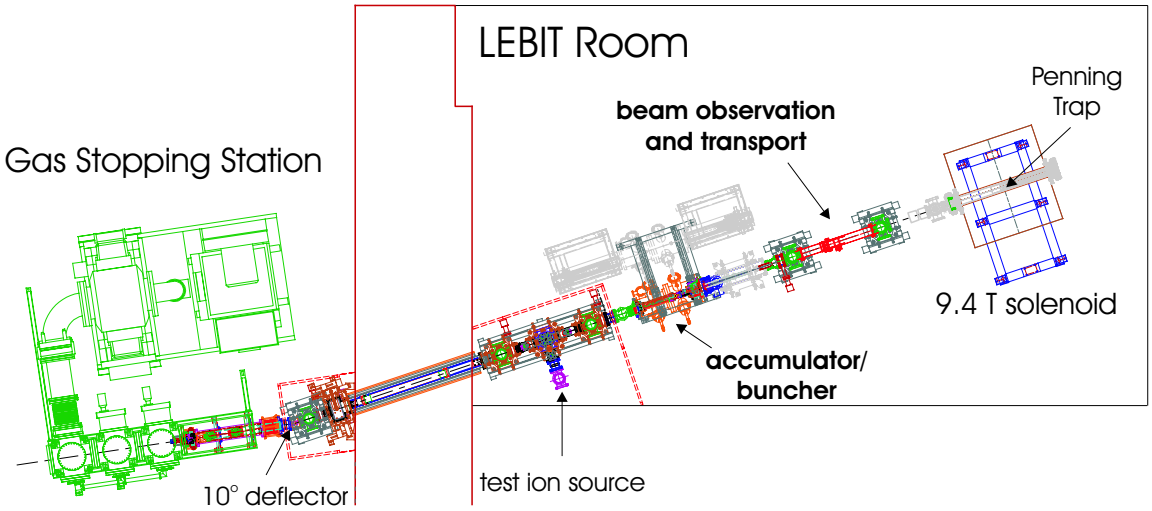

Figure 5.2: Top view of the LEBIT project layout. Various items in grey have yet to be installed. Those systems labeled in bold print are in place but have yet to be tested.

Appendix A

Beam Transport

A radiofrequency quadrupole (RFQ) ion guide will be used to transport ions from the nozzle and gas jet to the LEBIT beam transport section. Such a device will complement our differentially pumped system; that is, ions captured by the RFQ would be confined to the beam axis while the neutral helium carrier gas will be easily pumped away by the vacuum systems.

A.1 Background

A radiofrequency quadrupole (RFQ) is a device which focuses beams of charged particles onto its central axis. The RFQ consists of four rods. The rods opposite each other form a pair which are connected to be at the same electrical potential. These two pairs are then placed at equal but opposite potentials driven by a radiofrequency amplifier (Figure A.1). The electric field that an RFQ produces has the net effect of confining ions to the longitudinal axis. In this way, ions introduced to one end of the RFQ will be efficiently guided or transported along its length. RFQs have been developed for a number of applications including ion guiding, mass spectrometry and buffer gas ion cooling.

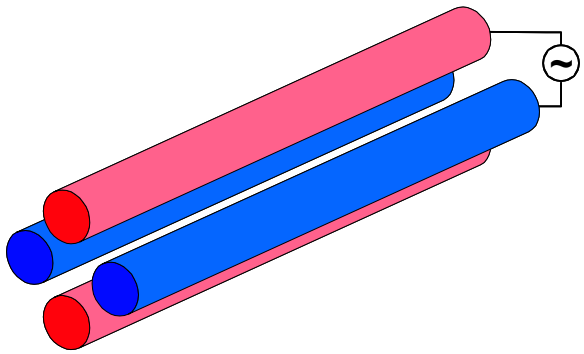

Figure A.1: Simple RFQ depiction. Alternating current is applied to the rods, with opposite rods connected so that they are at the same potential. Ions passing through the RFQ's length experience a confining field which keep them on the beam axis.

The electric potential, Φ, and the electric field, $\mathbf{E}$, of the RFQ are given by:

$$\Phi = \frac{x^2 - y^2}{r_0^2}[U - V\cos(\Omega t)] \tag{A.1}$$

$$\mathbf{E} = \begin{pmatrix} -x \\ y \end{pmatrix} \frac{2}{r_0^2}[U - V\cos(\Omega t)] \tag{A.2}$$

where the spatial coordinates x and y are perpendicular to the beam axis (z), r_0 is the characteristic nearest half-distance between opposite rods, U is the applied DC voltage, V is the zero to peak radiofrequency voltage, and $\Omega/2\pi$ is the radiofrequency [55]. If we consider the effective potential, D, for a radiofrequency voltage only (where U=0) [56]:

$$D = \frac{e}{m}\frac{1}{4\Omega^2}\mathbf{E}_0^2 = \frac{e}{m}\frac{V^2}{4\Omega^2}\frac{r^2}{r_0^4} \tag{A.3}$$

As an example for mass = 100u, V = 50 Volts, $\Omega/2\pi$ = 1 MHz and r_0= 7 mm, the potential, D, at r = r_0 would be approximately 1 eV. From Equation A.3, one can see that by choosing the appropriate rf voltage, the RFQ can also provide mass selection.

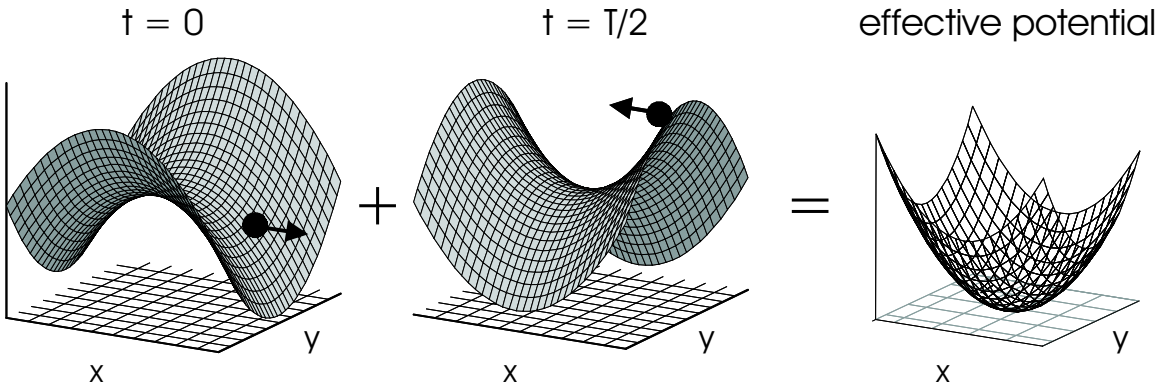

Figure A.2: Snapshots of the RFQ potential for two instances. The sum of the potentials (shown at time zero and at time equal to one half the period) gives an effective field which constrains ions on both the x and y axes.

A.2 The Gas Stopping Station RFQ

The Gas Stopping Station's RFQ was based on a similar ion guide design used at CERN for ISOLTRAP [57]. Each pole has a diameter of 18 mm and the characteristic radius, r_0, is 7 mm. The total length of each pole is approximately 145 cm, made up of short individual segments (see Figure A.3).

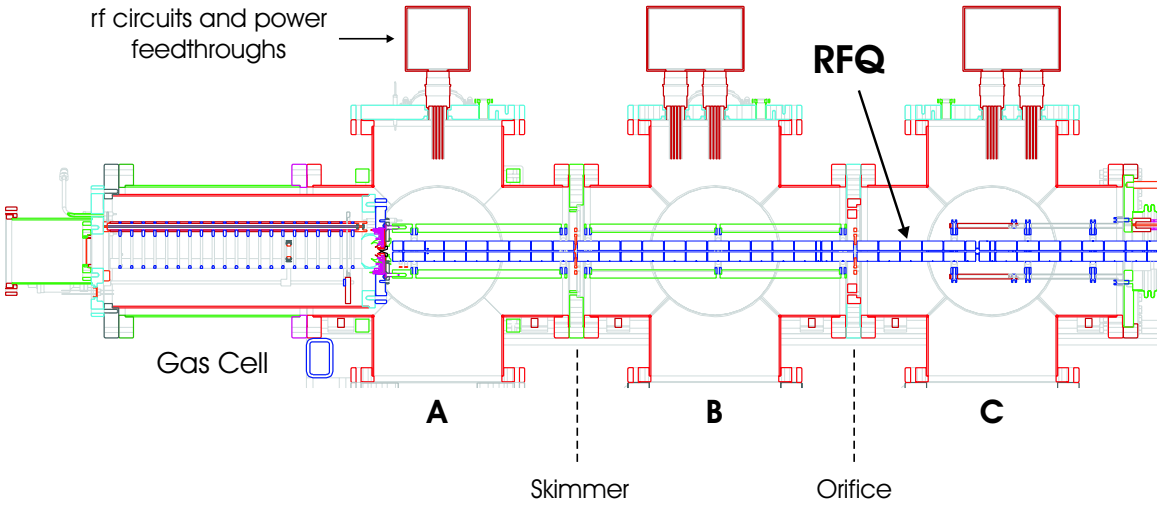

Figure A.3: Side view of the Gas Cell and the Gas Stopping Station's RFQ. The power feedthroughs and circuits sit atop the crosses for each section of the RFQ.

Each of the four poles is assembled by adding stainless steel segments separated by ceramic spacers to a central 6 mm stainless steel rod (threaded at each end). A

stainless steel nut at each of the rod compresses the segments and spacers. Segments are 10 mm, 20.5 mm and 41.5 mm in length and the ceramic spacers provide a 0.5 mm separation between segments. The number and length of the segments are chosen to fill the available spaces in Crosses A, B and C. A support system of aluminum octagons and ceramic stand-offs provides rigidity and orientation to the RFQ. Two large (~6 inch diameter) ceramic discs (Figure A.4) form the boundaries between Crosses (A/B and B/C) and are incorporated into the length of the RFQ poles. This first boundary (A/B) disc also holds the skimmer. The skimmer has an orifice of 3 mm diameter, chosen to allow maximum passage of ions while allowing the desired pressures to be achieved by the differential pumping. The second boundary (B/C) disc contains an opening (orifice) which is simply the clearance inside the RFQ poles.

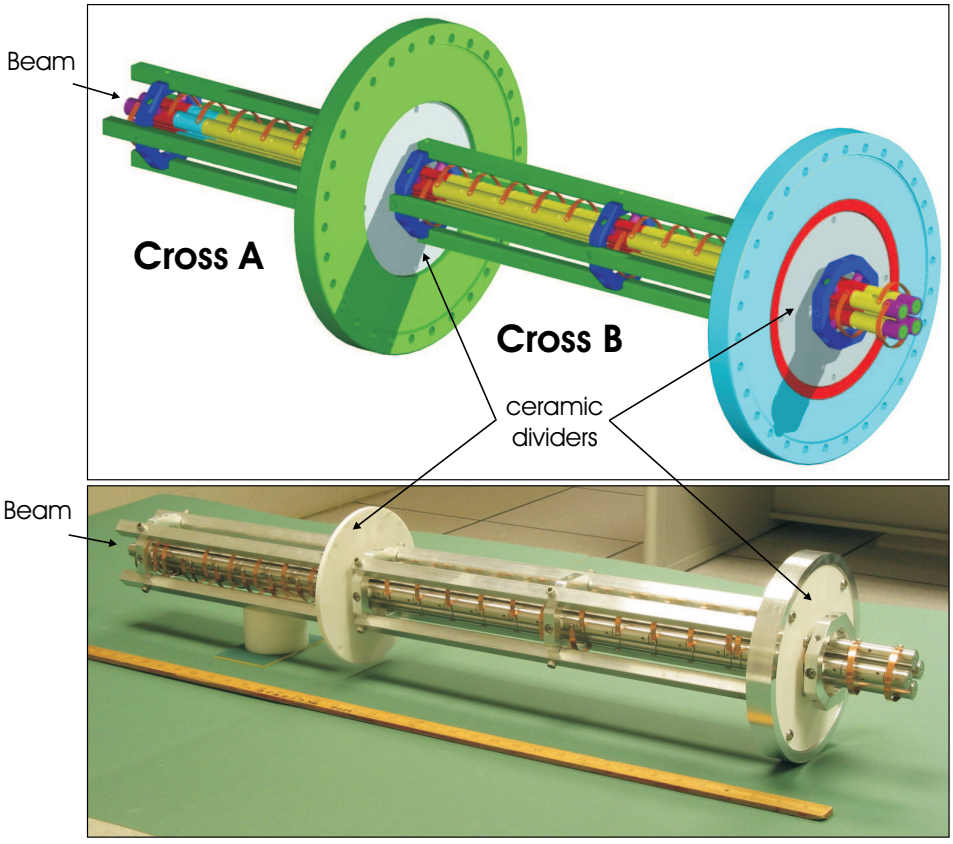

Figure A.4: Mechanical drawing (above) and photo (below) of the RFQ and its support structure, showing the different sections of the ion guide (only a portion of the RFQ in Cross C is displayed). The copper bands connect opposite rods, placing them at the same potential. The yardstick accompanying the photo shows the scale.

Direct current is provided by bipolar power supplies capable of delivering ±400 Volts and the radqiofrequency is provided by a square wave driver/amplifier built by Peter Schury. The DC and the rf potentials are fed to resonant circuits which rest outside Crosses A, B and C. Multi-pin power feedthroughs carry these voltages inside the vacuum system. Cabling from these feedthroughs to the RFQ segments uses KAP2 from Caburn MDC-Limited, a silver plated copper conductor coated by Type F Kapton. We chose to take advantage of the segmentation in Cross A so that a DC gradient could be placed on RFQ section A, helping to drive the ions downstream. Though RFQ sections B and C are also segmented, we currently have all segments at the same potential. The voltage scheme is:

Table A.1: Planned DC voltages for the RFQ segments of Cross A, based on the voltages placed across the nozzle (with the first segment placed at the same potential as the downstream face of the nozzle). The remainder of the segments in Crosses B and C will be at the same voltage as the skimmer.

Segment	1	2	3	4	5	6	7	8	skimmer
Voltage	0	-5	-15	-25	-35	-45	-55	-56	-60

Initial trials with the RFQ show that it transmits 35-40% of the beam. Because of available resources, these trials were performed by running the beam backward through the RFQ from an ion source upstream near the accumulator/buncher. When the beam travels in the expected direction (with the skimmer oriented properly), this percentage is expected to rise, conservatively, to 50%.

Bibliography

[1] E. M. Burbidge, G. R. Burbidge, W. A. Fowler, and F. Hoyle. *Rev. Mod. Phys.*, **29**:547, 1957.

[2] A. G. W. Cameron. *PASP*, **69**:201, 1957.

[3] R. K. Wallace and S. E. Woosley. *ApJS*, **45**:389, 1981.

[4] T. Glasmacher. *Annu. Rev. Nucl. Part. Sci.*, **48**:1, 1998.

[5] P. F. Mantica et al. *Phys. Rev. C*, **67**:014311, 2003.

[6] Yu. Kudryavtsev. *Nucl. Instr. and Meth. B*, **179**:412, 2001.

[7] D. Lunney and G. Bollen. *Hyperfine Int*, **129**:249, 2000.

[8] R. F. Casten and B. M. Sherrill. *Prog. Part. Nucl. Phys.*, **45**:S171, 2000.

[9] C. J. Barton et al. *Phys. Rev. C*, **67**:034310, 2003.

[10] G. F. Lima et al. *Phys. Rev. C*, **65**:044618, 2002.

[11] A. S. Lalleman. *Hyperfine Int*, **132**:315, 2001.

[12] F. Herfurth et al. *Eur. Phys. J. A*, **15**:17, 2002.

[13] J. P. Dufour et al. *Nucl. Instr. and Meth. A*, **248**:267, 1986.

[14] R. Anne et al. *Nucl. Instr. and Meth. A*, **257**:215, 1987.

[15] K. H. Schmidt et al. *Nucl. Instr. and Meth. A*, **260**:287, 1987.

[16] H. Geissel et al. *Nucl. Instr. and Meth. A*, **282**:247, 1989.

[17] D. J. Morrissey and B. M. Sherrill. *Phil. Trans. R. Soc. London*, **356**:1985, 1998.

[18] A. C. Mueller and R. Anne. *Nucl. Instr. and Meth. B*, **56/57**:559, 1991.

[19] B. M. Sherrill, D. J. Morrissey, J. A. Nolen, N. Orr, and J. A. Winger. *Nucl. Instr. and Meth. B*, **70**:298, 1992.

[20] H. Geissel et al. *Nucl. Instr. and Meth. B*, **70**:286, 1992.

[21] T. Kubo et al. Proc. First Intl. Conf. on Radioactive Nuclear Beams, Berkeley, W. D. Meyers, J.M. Nitschke, and E. Norman, eds., World Scientific, Singapore, p. 563, 1990.

[22] D. J. Morrissey, B. M. Sherrill, M. Steiner, A. Stolz, and I. Wiedenhöver. *Nucl. Instr. and Meth. B*, **204**:90, 2003.

[23] S. Schwarz, G. Bollen, D. Lawton, P. Lofy, D. J. Morrissey, J. Ottarson, R. Ringle, P. Schury, T. Sun, V. Varentsov, and L. Weissman. *Nucl. Instr. and Meth. B*, **204**:507, 2003.

[24] H. Geissel et al. *Nucl. Instr. and Meth. B*, **195**:3, 2002.

[25] J. Ärje and K. Valli. *Nucl. Instr. and Meth. A*, **179**:533, 1981.

[26] J. Ärje et al. *Nucl. Instr. and Meth. A*, **247**:431, 1986.

[27] P. Dendooven. *Nucl. Instr. and Meth. B*, **126**:182, 1997.

[28] J. Äystö. *Nucl. Phys. A*, **693**:477, 2001.

[29] M. Wada et al. *Nucl. Instr. and Meth. B*, **204**:570, 2003.

[30] G. Savard et al. *Nucl. Phys. A*, **701**:292c, 2002.

[31] G. Savard et al. *Nucl. Instr. and Meth. B*, **204**:582, 2003.

[32] J. Dilling et al. *Hyperfine Int*, **127(1/4)**:491, 2000.

[33] M. Wada et al. In *Proceedings of Non-Neutral Plasma Physics IV, vol. 606*, page 625. American Institute of Physics, 2002.

[34] G. F. Knoll. *Radiation Detection and Measurement.* John Wiley & Sons, Inc., New York, 3rd edition, 2000.

[35] F. Hubert, R. Bimbot, and H. Gauvin. *At. Data and Nucl. Data Tables*, **46**:1, 1990.

[36] J. F. Ziegler and J.B. Biersack. computer program SRIM 2000/01/03. Available from <http://www.srim.org>.

[37] J. F. Ziegler, J. P. Biersack, and U. Littmark. *The Stopping and Range of Ions in Solids*, volume 1. Pergamon, New York, 1985.

[38] C. Scheidenberger and H. Geissel. *Nucl. Instr. and Meth. B*, **135**:25, 1998.

[39] J. Lindhard and A. H. Sørensen. *Nucl. Instr. and Meth. B*, **135**:25, 1998.

[40] D. Bazin, O. Tarasov, M Lewitowicz, and O. Sorlin. *Nucl. Instr. and Meth. A*, **482**:314, 2002.

[41] O. B. Tarasov and D. Bazin. *Nucl. Instr. and Meth. B*, **204**:174, 2003.

[42] T. Baumann et al. *Nucl. Phys. A*, **701**:282c, 2002.

[43] H. Paul and A. Schinner. *Nucl. Instr. and Meth. B*, **179**:299, 2001.

[44] A. Stolz, 2003. Private communication.

[45] H. Weick et al. *Nucl. Instr. and Meth. B*, **164-165**:168, 2000.

[46] C. Scheidenberger et al. *Nucl. Instr. and Meth. B*, **204**:119, 2003.

[47] J. Stetson, 2003. Private communication.

[48] Yu. Kudryavtsev. *Rev. Sci. Instr.*, **69**:738, 1998.

[49] D. R. Lide (ed.). *Handbook of Chemistry and Physics.* CRC Press, Washington D.C., 2002.

[50] V. L. Varentsov and A. A. Ignatiev. *Nucl. Instr. and Meth. A*, **413**:447, 1998.

[51] A. Roth. *Vacuum Technology*, page 69. Elsevier, The Netherlands, 3rd edition, 1996.

[52] A.E. Beylich. Z. flugwiss. Weltraumforsch. 3, Heft 1, 1979.

[53] LLC Bechtel BWXT Idaho. SIMION (3D version 7.00) software, 1999.

[54] G. Bollen. "LEBIT–Pilot Mass Measurement Program," NSCL proposal for experiment, 2002.

[55] D. Gerlach. *Ion-Molecule Reaction Dynamics, Part 1, Advances in Chemical Physics Series*, volume 87. John Wiley & Sons, Inc., New York, 1992.

[56] S. Schwarz, 2003. Private communication.

[57] F. Herfurth et al. *Nucl. Instr. and Meth. A*, **469**:254, 2001.